



Technische Universität München  
Fakultät für Maschinenwesen  
Lehrstuhl für Turbomaschinen und Flugantriebe

## **Experimental and Numerical Study of Cryogenic Flashing Spray in Spacecraft Application**

**Meng Luo**

Vollständiger Abdruck der von der Fakultät für Maschinenwesen der Technischen Universität München zur Erlangung des akademischen Grades eines

Doktor-Ingenieurs (Dr.-Ing.)

genehmigten Dissertation.

Vorsitzender: Priv.-Doz. Dr.-Ing. habil. Xiangyu Hu

Prüfer der Dissertation: 1. Prof. Dr.-Ing. Oskar J. Haidn  
2. Prof. Dr. rer. nat. Michael Pfitzner

Die Dissertation wurde am 25.04.2018 bei der Technischen Universität München eingereicht und durch die Fakultät für Maschinenwesen am 24.08.2018 angenommen.



*To my Parents*  
*To my Wife*



# Acknowledgment

This work is performed in the Institute of Turbomachinery and Flight Propulsion of Technische Universität München (LTF-TUM). Great thanks to the China Scholarship Council and Munich Aerospace for the financial support.

I would like to express the most sincere gratitude to my supervisor Prof. Dr.-Ing. Oskar J. Haidn, for offering me the opportunity of this engaging project, and for his insightful advice and persistent encouragement during my research. Without his guidance and help, this dissertation would not have been possible.

I am grateful to Dr. Claus Wehmann, Dr.-Ing. Wolfgang Erhard, Dipl.-Ing. Gregor Schlieben and Dipl.-Ing. Christian Bauer and Dr. Yingchun Wu for their kind help with the experiments.

A full appreciation goes to Mr. Roland Grubert and Miss Zoe Gerstung in our workshop; and without your excellent work, I could not finish the test facility development.

Definitely I will never forget all other fellow colleagues in the Institute and the time we have spent together. In particular, I would like to thank Prof. Dr.-Ing. Volker Gümmer, Prof. Dr.-Ing. Andreas Hupfer, Simona Silvestri, M.Sc., Maria Palma Celano, M.Sc., Fernanda Winter, M.Sc., Dr.-Ing. Nan Chen, Zhendong Yu, M.Sc., Ye Hong, M.Sc., Chengyu Zhang, M.Sc. Dipl.-Ing. Yuriy Metsker, Dipl.-Ing. Daniel Paukner, Dipl.-Ing. Sebastian Lang, as well as the visiting scholars Prof. Xianggeng Wei, Yuan Tian, M.Sc., and other colleagues. The inspiring academic discussion and valuable feedbacks are beneficial to my research. Also many thanks to the students Manuel Kuchelmeister, M.Sc. and Usmam Rana, M.Sc. for their contribution to the research.

I also would like to thank my friends in Munich, Dr. Hanyin Sun and all others. Thanks for your accompany and the activities. I do cherish the time with all of you.

Last but not the least, I would like to express the deepest affection to my parents and my wife. Their unconditional love, support and encouragement have accompanied me all the way from China to Germany, and will be with me along my following journey.



# Abstract

In recent decades, the space industry and space agencies are confronted with the issues of increasing space debris and the highly toxic and carcinogenic propellants (e.g. MMH/NTO) that are utilized in the liquid propellant rocket engine. The European Union has put enormous efforts in more environmentally-friendly propellants. The cryogenic propellant pair of LO<sub>x</sub>/LCH<sub>4</sub> turns out to be a promising alternative. As a consequence, Munich Aerospace proposed the project “Propulsion Technologies for Green in-Orbit Spacecraft” to investigate the green propulsion technique. Under the support of this program, my research topic is focused on the green propellant behaviors under low pressure conditions, with an aim to provide a solid knowledge for the green propulsion technique development.

The test facility has been designed and built in the Institute of Turbomachinery and Flight Propulsion of Technische Universität München to perform a morphological study of the LN<sub>2</sub>, LO<sub>x</sub> and LCH<sub>4</sub> sprays with high-speed Schlieren and Shadowgraph techniques. Under low pressure conditions, the spray undergoes a violent atomization and vaporization, termed as the flashing phenomenon. The characteristics of the flashing spray and the impact of the injection boundary conditions (i.e. superheat degree, nozzle geometry) on this spray was explored in detail. Based on the nucleation theory, a non-dimensional energy parameter was proposed and it can successfully characterize the flashing spray atomization regimes. Furthermore, the Global Rainbow Refractometry technique (GRR) was for the first time applied to investigate the cryogenic propellant spray droplets. The refractive index and the probability distribution of the droplet size were retrieved from the rainbow patterns with the inverse method using the complex angular momentum scattering theory.

Meanwhile, a numerical simulation was conducted to unveil the flashing phenomenon with the coupled Euler-Lagrange approach. The continuous phase was calculated under the Euler frame by solving the 3D-URANS equations, and the dispersed phase was tracked under the Lagrangian frame. A Flashing Spray Model (FSM) was developed and implemented into the CFD solver by considering the flashing evaporation and the interphase heat, mass and momentum exchange. The simulation results show a fairly good agreement with the experimental data.

In sum, a comprehensive investigation of the cryogenic spray under low pressure conditions has been performed in this work and the further development of the green propulsion technique will benefit from the revealed knowledge.



# Kurzfassung

In den letzten Jahrzehnten wurde im Europa verstärkt an Problemlösungen gegen Weltraumschrott und Alternativen und umweltfreundlichen Treibstoffen für die Raumfahrtindustrie geforscht, die giftige und krebserregende Treibstoffe wie zum Beispiel MMH/NTO ersetzen sollen. Die Europäische Union hat große Anstrengungen hinsichtlich umweltverträglichen Treibstoffen unternommen. Als vielversprechende Alternative bietet sich die Kombination flüssiger Sauerstoff/flüssiges Methan (LOx/LCH<sub>4</sub>) an. Daher hat der Verein Munich Aerospace e.V ein Forschungsprojekt mit dem englischen Namen "Populsion Technologies for Green in-Orbit Spacecraft" eingeleitet. Das Ziel des Projekts ist die Forschung im Bereich umweltfreundlichen Treibstoffe wie zum Beispiel LOx/LCH<sub>4</sub>. Diese Forschungsarbeit fand im Rahmen dieses Projekts statt. Der Schwerpunkt dieser Arbeit lag darin, das Verhalten solcher umweltfreundlichen Treibstoffe bei niedrigen Druckbedingungen zu untersuchen, sodass auf Basis dieser Forschung weitere technologische Entwicklungen im Bereich umweltfreundlichen Treibstoffe möglich ist.

Der Versuchsstand wurde am Lehrstuhl für Turbomaschinen und Flugantriebe der Technische Universität München aufgebaut. An diesem Versuchsstand wurden die Erststudien zur Untersuchung des Verhaltens von flüssigem Stickstoff (LN<sub>2</sub>), Sauerstoff (LOx) und Methan (LCH<sub>4</sub>) bei Einspritzung in Vakuum durchgeführt. Für die Untersuchung wurden die Hochgeschwindigkeits-Schlierenfotografie und die Schattenfotografie Verfahren eingesetzt. Bei Einspritzung unter niedrigen Druckbedingungen (Vakuum) tritt eine extreme Zerstäubung und Verdampfung des Fluids auf. Dieses Verhalten der extremen Zerstäubung und Verdampfung wird in der Fachsprache "Flashing" genannt. Eine Einspritzung mit einem solchen Verhalten wird als "Flashing Spray" bezeichnet. Im Rahmen dieser Forschungsarbeit wurde der Einfluss der Einspritzungsparameter wie zum Beispiel Überhitzungsgrad des Fluids und der Einfluss der Düsengeometrie auf das Verhalten von Flashing Spray untersucht. Basierend auf der Blasenbildungstheorie können die verschiedenen Zerstäubungsgebiete des Flashing Sprays durch einen dimensionslosen Energieparameter charakterisiert werden. Des weiteren wurde zum ersten Mal das Global Rainbow Refractometry Verfahren (GRR) zur Untersuchung der Spray Tröpfchen von kryogenen Treibstoffen eingesetzt. Der Berechnungsindex sowie die wahrscheinliche Verteilung der Tröpfchen wurden anhand des Regenbogenmusters mit einer inversen Methode ermittelt. Dazu wurde die Methodik des komplexen Drehimpuls Streutheorie im Englischen "complex angular momentum" genannt, verwendet.

Das Flashing Spray wurde auch numerisch untersucht. In der CFD Simulation wurde das Euler-Lagrange Verfahren angewandt, welches sich für die Simulation von Mehrphasenströmung insbesondere für die tropfenbeladener Strömung eignet. In diesem Verfahren wird die kontinuierliche Phase mit Hilfe des Eulerschen Ansatzes betrachtet. Dazu werden 3-D URANS Gleichungen gelöst. Die Bewegung der dispersen Phase wird mit Hilfe der gewöhnlichen Differentialgleichungen mit dem Lagrangeschen Ansatz erfasst. Für die Flashing Spray Simulation wurde ein Model entwickelt, welches die Flashing-

Verdampfung und den Massen-, Impuls- und Wärmeaustausch zwischen den beiden Phasen erfasst. Dieses Model genannt Flashing Spray Model (FSM) wurde in den CFD Solver implementiert. Die Simulationsergebnisse wurden mit den experimentellen Daten validiert. Die Simulationsergebnisse zeigten eine gute Übereinstimmung mit den experimentellen Daten.

Zusammenfassend lässt sich sagen, dass in dieser Dissertation eine grundlegende Untersuchung von kryogenen Spray bei niedrigen Druckbedingungen durchgeführt wurde, welche für die weitere Forschung und technologische Entwicklung im Bereich grüne Treibstoffe genutzt werden kann.

# Contents

<b>Abstract</b>	<b>I</b>
<b>Kurzfassung</b>	<b>III</b>
<b>List of Figures</b>	<b>IX</b>
<b>List of Tables</b>	<b>XIII</b>
<b>Nomenclature</b>	<b>XV</b>
<b>Chapter 1. Introduction</b>	<b>1</b>
1.1 The Research Objective .....	1
1.2 Motivation and Background .....	1
1.3 The Methodology for the Research.....	2
1.4 Outline of the Work .....	2
<b>Chapter 2. Background Theory and Literature Review</b>	<b>5</b>
2.1 Liquid Oxygen/Liquid Methane Engine .....	5
2.2 Thermodynamics of Superheated Fluid .....	6
2.2.1 Two-phase Flow State Criteria .....	6
2.2.2 Binodal and Spinodal Curve .....	8
2.2.3 Thermal Process of Flashing Spray.....	9
2.3 Kinetics of Nucleation .....	10
2.3.1 Bubble Formation in Superheated Liquid.....	10
2.3.2 Bubble Growth in Superheated Liquid.....	12
2.4 Flashing Atomization Correlations .....	14
2.5 Flashing Spray Morphology .....	16
2.6 Literature Review of Flashing Spray .....	18
2.6.1 Experimental Study of Flashing Spray.....	18

2.6.2	Numerical Study of Flashing Spray.....	22
2.7	Summary.....	24
<b>Chapter 3.</b>	<b>Experimental Investigation of Cryogenic Flashing Spray</b>	<b>25</b>
3.1	Introduction.....	25
3.2	Experimental Facilities .....	25
3.2.1	Flashing Test Facility.....	25
3.2.2	Optical Diagnosis Methodology .....	29
3.2.3	Measurement and Uncertainty.....	30
3.2.4	Data Acquisition.....	35
3.3	Results and Analyses.....	36
3.3.1	Test Cases .....	36
3.3.2	Flashing Spray Evolution.....	36
3.3.3	Effect of Injector Geometry on Flashing Spray.....	41
3.3.4	Thermal Characteristics of Flashing Spray .....	46
3.3.5	Flashing Spray Solidification .....	50
3.3.6	Flashing Atomization Criterion .....	52
3.4	Summary.....	57
<b>Chapter 4.</b>	<b>Investigation of Cryogenic Spray with Rainbow Refractometry</b>	<b>59</b>
4.1	Introduction.....	59
4.2	Rainbow Phenomenon.....	60
4.3	Experimental Setup .....	61
4.4	Data Inversion Algorithms.....	64
4.4.1	Characteristic Points Method .....	65
4.4.2	Global Points Method .....	68
4.5	Results and Discussions.....	69
4.6	Uncertainty Analysis .....	74
4.7	Summary.....	75
<b>Chapter 5.</b>	<b>Modeling of Cryogenic Flashing Spray</b>	<b>77</b>
5.1	Introduction.....	77
5.2	Flashing Spray Model Development .....	78

5.2.1	Flashing Evaporation Model.....	78
5.2.2	Droplet Energy Balance .....	82
5.2.3	Droplet Trajectory.....	82
5.2.4	Source Terms Development.....	83
5.2.5	Temperature Dependent Properties .....	86
5.3	Simulation Procedure.....	86
5.3.1	Simulation Setup.....	86
5.3.2	Computational Mesh and Boundary Conditions .....	88
5.3.3	Spatial and Temporal Resolution Validation.....	89
5.4	Results and Discussions .....	91
5.4.1	Spray Morphological Characteristics .....	91
5.4.2	Temperature Characteristics .....	93
5.4.3	Velocity Characteristics.....	96
5.4.4	Pressure Oscillation.....	99
5.4.5	Droplet Size Probability Distribution.....	100
5.5	New Correlation of Flashing Evaporation.....	104
5.6	Summary .....	107
<b>Chapter 6. Conclusions and Outlooks</b>		<b>109</b>
6.1	Summary and Conclusions.....	109
6.1.1	Experimental Work .....	109
6.1.2	Modeling Work.....	110
6.2	Outlooks .....	111
<b>Appendix</b>		<b>125</b>
I.	Test Hard Ware.....	125
II.	Lorenz-Mie Theory.....	127



# List of Figures

1.1	Schematic of the present work .....	3
2.1	Vacuum specific impulse of propellants .....	6
2.2	Equilibrium state of two-phase flow.....	7
2.3	$p$ - $v$ - $T$ diagram based on the van der Waals equation (Adapted from Ref. [7]) .....	8
2.4	Homogeneous and heterogeneous nucleation barrier .....	11
2.5	Predicted bubble growth (adapted from Ref. [17, 18, 19]) .....	14
2.6	LN <sub>2</sub> spray under different pressure conditions. From left to right: vacuum condition (Ref. [27]), subcritical injection and supercritical condition (adapted from Ref. [28]) .....	16
2.7	Water spray under different superheat conditions with splash-plate injector (adapted from Ref. [29]).....	17
2.8	Iso-octane spray under different superheat conditions with single-hole jet injector (adapted from Ref. [30]) .....	17
2.9	Acetone spray under different superheat conditions with single-hole jet injector (adapted from Ref. [31]) .....	18
3.1	Schematic of the flashing test setup.....	26
3.2	Flashing test setup .....	27
3.3	Test chamber .....	27
3.4	Test jet injectors .....	28
3.5	Schematic of Schlieren setup .....	30
3.6	Error of the measurement.....	30
3.7	Temperature measurement calibration.....	31
3.8	Analog signal input model (for pressure sensors) .....	32
3.9	Injector discharge coefficient with pressure drop.....	34
3.10	DAQ hard ware and the graphical user interface.....	35
3.11	$p$ - $T$ diagram of nitrogen .....	37
3.12	LN <sub>2</sub> flashing spray under different superheat conditions (Injector #1).....	38
3.13	Jet breakup regimes description by Ohnesorge and Miesse [83, 84].....	38

3.14	LN <sub>2</sub> flashing spray under different superheat conditions (Injector #2) .....	39
3.15	Flashing spray transient process .....	40
3.16	Cryogenic sprays with different injector aspect ratios .....	42
3.17	Definition of the spray angle .....	43
3.18	Spray angles at various superheat degrees with different injector aspect ratios .....	44
3.19	Cryogenic sprays with different injector diameters .....	45
3.20	Spray angles at various superheat degrees with different injector diameters .....	46
3.21	Temperature evolution along LN <sub>2</sub> spray centerline ( Injector #5) .....	47
3.22	Temperature evolution along LOx spray centerline ( Injector #1).....	49
3.23	Temperature evolution along LN <sub>2</sub> spray centerline ( Injector #1) .....	50
3.24	Formation of solid nitrogen and solid methane in the flashing spray .....	52
3.25	LN <sub>2</sub> flashing evolution process at different superheat degrees ( $p_{inj} \sim 10$ bar, Injector #3).....	53
3.26	LN <sub>2</sub> flashing evolution process at different superheat degrees ( $p_{inj} \sim 8$ bar, Injector #4).....	54
3.27	LN <sub>2</sub> flashing evolution process at different superheat degrees ( $p_{inj} \sim 8$ bar, Injector #5).....	54
3.28	LN <sub>2</sub> flashing evolution process at different superheat degrees ( $p_{inj} \sim 10$ bar, Injector #1).....	55
3.29	LOx flashing evolution process at different superheat degrees ( $p_{inj} \sim 10$ bar, Injector #1).....	56
3.30	LN <sub>2</sub> flashing evolution process at different superheat degrees ( $p_{inj} \sim 15$ bar, Injector #1).....	56
3.31	LOx flashing evolution process at different superheat degrees ( $p_{inj} \sim 16$ bar, Injector #1).....	56
3.32	Parameter $\zeta$ under different superheat conditions .....	57
4.1	Single droplet scattering intensity near the rainbow angle .....	60
4.2	Schematic of Global Rainbow Refractrometry.....	62
4.3	Global Rainbow Refractrometry setup.....	62
4.4	Calibration of the scatter angle and CCD pixels.....	63
4.5	Correlation of the scatter angle with CCD pixels .....	63
4.6	Temperature-refractive index diagram of LN <sub>2</sub> .....	64
4.7	Temperature-refractive index diagram of LOx.....	64
4.8	Global rainbow signal of droplet size with Gaussian distribution ( $D=100$ , $\delta=10$ ) .....	67
4.9	Calculation flow chart of the characteristic point method.....	67
4.10	Effect of prescribed droplet distribution on the derived mean diameter .....	68
4.11	Effect of prescribed droplet distribution on derived refractive index .....	68
4.12a	LN <sub>2</sub> rainbow image .....	70
4.12b	LN <sub>2</sub> rainbow scattering intensity and recomputed intensity .....	70

4.12c	LN <sub>2</sub> droplet size probability distribution.....	70
4.12d	Derived LN <sub>2</sub> droplet mean diameter.....	70
4.13a	LOx rainbow image.....	71
4.13b	LOx rainbow scattering intensity and recomputed intensity.....	71
4.13c	LOx droplet size probability distribution.....	71
4.13d	Derived LOx droplet mean diameter.....	71
4.14a	LCH <sub>4</sub> rainbow image.....	72
4.14b	LCH <sub>4</sub> rainbow scattering intensity and recomputed intensity.....	72
4.14c	LCH <sub>4</sub> droplet size probability distribution.....	72
4.14d	Derived LCH <sub>4</sub> droplet mean diameter.....	72
4.15	Statistical results of measured temperatures.....	75
5.1	Schematic of droplet model.....	80
5.2	Schematic of the mass, heat and momentum exchange.....	83
5.3	Several properties of the simulated fluids.....	86
5.4	Flowchart of the simulation laws.....	87
5.5	Flowchart of unsteady simulation per time step.....	87
5.6	Computational domain, mesh and boundary conditions.....	88
5.7	Mesh sensitivity study.....	90
5.8	Time sensitivity study.....	90
5.9	Simulated spray shape under flashing conditions.....	91
5.10	LOx spray contour.....	92
5.11	LN <sub>2</sub> spray contour.....	92
5.12	Time evolution of LN <sub>2</sub> flashing spray.....	93
5.13	LOx temperature distribution along the spray centerline.....	94
5.14	LN <sub>2</sub> temperature distribution along the spray centerline.....	94
5.15	Temperature contour of LOx droplets.....	95
5.16	Temperature contour of oxygen gas.....	95
5.17	Temperature contour of LN <sub>2</sub> droplets.....	95
5.18	Temperature contour of nitrogen gas.....	95
5.19	Statistical results of evaporation mass flow rate of LOx spray.....	96
5.20	LOx spray velocity in the spray axial direction.....	97
5.21	LOx droplet velocity in the spray radial direction.....	97

5.22	LN <sub>2</sub> spray velocity in the spray axial direction.....	97
5.23	LN <sub>2</sub> droplet velocity in the spray radial direction .....	97
5.24	Velocity fluctuation in the spray radial direction of LOx spray .....	98
5.25	Velocity fluctuation in the spray radial direction of LN <sub>2</sub> spray .....	98
5.26	LOx pressure evolution at different locations.....	100
5.27	LN <sub>2</sub> pressure evolution at different locations .....	100
5.28	LOx droplet size distribution along the spray centerline.....	101
5.29	LOx droplet size distribution in the spray radial direction .....	101
5.30	LN <sub>2</sub> droplet size distribution along the spray centerline.....	101
5.31	LN <sub>2</sub> droplet size distribution in the spray radial direction.....	101
5.32	Statistical distribution of LOx droplet size at the outlet plane.....	102
5.33	Statistical distribution of LN <sub>2</sub> droplet size at the outlet plane .....	102
5.34	LN <sub>2</sub> spray contour (case #3) .....	103
5.35	LN <sub>2</sub> temperature distribution along the spray centerline (case #3) .....	103
5.36	LOx spray contour (case #4).....	103
5.37	LOx temperature distribution along the spray centerline (case #4) .....	103
5.38	LOx temperature distribution with new superheat evaporation correlation (Case#1).....	106
5.39	LOx temperature distribution with new superheat evaporation correlation (Case#4).....	106
5.40	LN <sub>2</sub> temperature distribution with new superheat evaporation correlation (Case#2) .....	106
5.41	LN <sub>2</sub> temperature distribution with new superheat evaporation correlation (Case#3) .....	106
I.1	Flashing test facility.....	125
I.2	DAQ system .....	125
I.3	Current board for the analog signal input (for pressure sensors).....	126
I.4	Current board for the digital signal output (for solenoid valves).....	126
I.5	Venturi flow meter.....	126
I.6	Injectors.....	126
I.7	Global Rainow Refractometry setup .....	126
II.1	Mie-scattering intensity of a single droplet.....	128

# List of Tables

2.1	Typical measurement methods used in flashing spray .....	22
3.1	Detailed information of pressure sensors.....	33
3.2	Parameters of injector geometry.....	36
3.3	General operation conditions of flashing test.....	36
3.4	Boundary conditions of Fig. 3.16.....	41
3.5	Boundary conditions in Fig. 3.18 .....	44
3.6	Properties of cryogenic fluids (@1.0 bar).....	51
4.1	General test conditions.....	61
4.2	Derived results from Fig. 4.10, Fig. 4.11 and Fig. 4.12.....	73
5.1	Mesh size and time step sensitivity study .....	90
5.2	Simulation cases .....	91
5.3	Properties of the simulated fluids and pentane (@ 1bar).....	104



# Nomenclature

## Latin Symbols

Symbol	Denotaion	Dimension
$A$	area	$[m^2]$
$Bi$	Biot number, $Bi=hd/\lambda$	$[-]$
$B_T$	Spalding heat transfer number	$[-]$
$B_M$	Spalding mass transfer number	$[-]$
$C_D$	drag coefficient	$[-]$
$c_p$	specific heat capacity	$[J/kg/K]$
$D, d$	diameter	$[m]$
$D_{10}$	arithmetic mean diameter	$[m]$
$D_{32}$	Sauter mean diameter	$[m]$
$f$	focal length	$[m]$
$\Delta G^*$	nucleation barrier	$[J]$
$h$	specific enthalpy, heat transfer coefficient	$[J/kg], [W/m^2/K]$
$I$	scattering intensity, unit tensor	$-$
$J$	nucleation rate	$[1/m^3/s]$
$Ja$	Jakob number, $Ja=c_p\Delta T/L$	$[-]$
$K$	cavitation number	$[-]$
$L$	latent heat of vaporization, length	$[J/kg], [m]$
$L_c$	characteristics length	$[m]$
$m$	mass, refractive index	$[kg], [-]$
$\dot{m}$	mass flow rate	$[kg/s]$
$Nu$	Nusselt number, $Nu=hd/\lambda$	$[-]$
$Oh$	Ohnesorge Number, $\mu/\sqrt{\rho\sigma d}$	$[-]$
$p$	pressure	$[Pa, bar]$
$Pr$	Prandtl number, $Pr=c_p\mu/\lambda$	$[-]$
$\dot{Q}$	volume flow rate	$[m^3/s]$
$r$	radius	$[m]$
$Re$	Reynolds number, $Re=\rho v d/\mu$	$[-]$
$R_p$	pressure ratio, $R_p=p_{sat}(T_{inj})/p_c$	$[-]$
$s$	specific entropy	$[J/kg]$
$T$	temperature	$[K]$
$t$	time	$[s]$
$\Delta T$	degree of superheat	$[K]$
$U$	internal energy, velocity	$[J], [m/s]$
$u'$	velocity fluctuation	$[m/s]$

$v$	velocity	[m/s]
$V$	volume	[m <sup>3</sup> ]
$We$	Weber number, $We=\rho v^2 d/\sigma$	[-]
$x, y$	coordinates	[m]
$z$	coordinates, spray axis	[m]

## Greek Symbols

Symbol	Denotaion	Dimension
$\alpha$	convection coefficient, angle	[W/m <sup>2</sup> /K], [°]
$\alpha_f$	effective internal heat transfer coefficient	[kW/m <sup>2</sup> /K]
$\alpha'_f$	corrected effective internal heat transfer coefficient	[W/m <sup>2</sup> /K]
$\beta$	thermal expansion coefficient, angle	[1/K], [°]
$\delta$	standard deviation	[-]
$\varepsilon$	emissivity, angle difference	[-], [rad]
$\theta$	angle	[rad]
$\lambda$	thermal conductivity, light wavelength	[W/m/K], [m]
$\mu$	dynamic viscosity	[Pa.s]
$\Delta\mu$	chemical potential difference	[J/molecule]
$v$	specific volume	[m <sup>3</sup> ]
$\rho$	density	[kg/m <sup>3</sup> ]
$\sigma$	surface tension, standard deviation	[N/m], [-]
$\Phi$	rate of heat flow, source term	[w], -
$\varphi$	angle, volumetric source term	[rad]
$\tau$	angle, time, viscous stress	[rad], [s], [Pa]
$\zeta, \xi$	dimensionless nucleation barrier	[-]
$\chi$	size parameter, dimensionless nucleation barrier	[-]

## Abbreviations

Symbol	Denotaion
BFSL	Best Fit Straight Line
CAM	Complex Angular Momentum
CFD	Computational Fluid Dynamics
CFL	Courant–Friedrichs–Lewy condition
CMOS	Complementary Metal-Oxide-Semiconductor
CNT	Classical Nucleation Theory
CPM	Characteristic Points Method
CW	Continuous Wave
DAQ	Data Acquisition
DIT	Dual Infrared Thermography
DLR	Germany Aerospace Center
DPM	Discrete Particle Model
EOS	Equations of State

<b>Symbol</b>	<b>Denotaion</b>
FFT	Fast Fourier Transform
FPGA	Field-programmable Gate Array
FPS	Frames per Second
FSM	Flashing Spray Model
GDI	Gasoline Direct Injection
GN <sub>2</sub>	Nitrogen Gas
GO <sub>x</sub>	Oxygen Gas
GPM	Global Points Method
GRR	Global Rainbow Refractometry
GRT	Global Rainbow Thermometer
HEM	Homogeneous Equilibrium Model
HRM	Homogeneous Relaxation Model
IRES	Infrared Extinction/Scattering
LCH <sub>4</sub>	Liquid Methane
LDA	Laser Doppler Velocimetry
LES	Large Eddy Simulation
LH <sub>2</sub>	Liquid Hydrogen
LO <sub>x</sub>	Liquid Oxygen
LRE	Liquid Rocket Engine
LTf	Institute of Turbomachinery and Flight Propulsion
MMH	Monomethylhydrazine
MPA	Malvern Particle Analyzer
NASA	National Aeronautics and Space Administration
NIST	National Institute of Standards and Technology
NTO	Dinitrogen Tetroxide
OME	Orbital Maneuvering Engines
PDA	Phase Doppler Anemometry
PISO	Pressure-Implicit with Splitting of Operators
PIV	Particle Image Velocimetry
PLIF	Planar Laser Induced Fluorescence
PTV	Particle Tracking Velocimetry
R134a	1,1,1,2-Tetrafluoroethane
RANS	Reynolds-averaged Navier–Stokes
RCE	Reaction Control Engines
RMS	Root Mean Square
RP1	Refined Petroleum-1
SRR	Standard Rainbow Refractometry
TC	Thermocouple
TUM	Technische Universität München
UDF	User Defined Function
UDMH	Unsymmetrical Monomethylhydrazine
VOF	Volume of Fluid method

## Superscripts and Subscripts

Symbol	Denotaion
0	initial condition
<i>amb, ∞</i>	ambient condition
<i>b, sat</i>	saturation condition
<i>c</i>	chamber
<i>cell</i>	computational cell
<i>cor</i>	corrected value
<i>cri</i>	critical condition
<i>d, l, p</i>	liquid phase, droplet
<i>e</i>	energy source
<i>eq</i>	equilibrium state
<i>flash</i>	flashing condition
<i>g, v</i>	gas phase
<i>het</i>	heterogeneous
<i>in</i>	entrance of the cell
<i>inf</i>	inflection point
<i>inj</i>	injection condition
<i>m</i>	mass
<i>max</i>	maximum value
<i>mean</i>	average value
<i>min</i>	minimum value
<i>mom</i>	momentum
<i>nucl</i>	nucleation
<i>out</i>	exit of the cell
<i>radi</i>	radiation
<i>ref</i>	reference condition
<i>rg</i>	rainbow
<i>spe</i>	specific condition
<i>t</i>	thermocouple
<i>tri</i>	triple point condition

## Constant

Symbol	Denotaion	Value
<i>g</i>	standard gravity	9.807 [m/s <sup>2</sup> ]
<i>k<sub>B</sub></i>	Boltzmann constant	1.38065×10 <sup>-23</sup> [J/K]
<i>R</i>	idea gas constant	8.3145 [J/mol/K]
<i>σ</i>	Stefan–Boltzmann constant	5.67037×10 <sup>-8</sup> [W/m <sup>2</sup> /K <sup>4</sup> ]

# Chapter 1. Introduction

## 1.1 The Research Objective

The present work focuses mainly on a non-equilibrium thermodynamic phenomenon named flashing atomization and vaporization, which may happen in the upper stage liquid propellant rocket engines (LRE) or in in-orbit thrusters. The aim is to investigate the thermal- and fluid dynamic behavior of the cryogenic fluids under vacuum conditions with both experimental and numerical methods. The revealed knowledge will contribute to the green propulsion technique development for the orbital debris removal purpose in the project “Propulsion Technologies for Green in-orbit Spacecraft” of Munich Aerospace.

## 1.2 Motivation and Background

In recent years, the space industry and space agencies are confronted with two major issues: the increasing space debris which pose a potential threat to the orbit safety, and the toxic propellants which is a serious cost problem. The European Community Regulation on Chemicals and their safe use has put hydrazine, a classical propellant for the satellite propulsion, on the list of substances of highly concern due to their hyper toxicity [1]. Therefore, to find alternative propellants and to develop the corresponding propulsion technique is needed. As the green propellant pair,  $LCH_4/LOx$ , becomes one of the best choices because of the lower thermal management requirement than that of  $LH_2/LOx$ . It is well known that the transient start-up is one of the most challenging operation processes of the rocket engine. Unlike the hypergolic propellant, an additional ignition system is required when the new propulsion systems utilize  $LCH_4/LOx$ . In order to predict this transient start-up process and to develop the corresponding ignition systems, a solid knowledge of the propellant behavior during this transient process (i.e. flashing phenomenon) should be acquired. In addition, as the performance of a rocket thruster heavily rely on the propellant injection processes (e. g. atomization, evaporation and mixture formation preceding combustion), it is also necessary to understand the involved injection thermodynamic process.

As to the flashing phenomenon, it occurs when a liquid deviates from the thermodynamic equilibrium and becomes superheated; that is to say, the liquid temperature is above the saturation temperature at the surrounding pressure. The flashing can be triggered by a fast isothermal depressurization. Due to the sudden depressurization, the fluid finds itself superheated in the new environment, which leads to fluid

metastable state (corresponding to the local minimum free energy of the system). With some perturbation, the fluid will return to an equilibrium state (i.e. global minimum free energy of the system) through bubble nucleation, growth, and jet atomization and vaporization. At the transient start-up in the upper stage rocket engine, due to a sudden depressurization, flashing may happen, which consequently affects the liquid propellants' disintegration, atomization, vaporization, and mixing process. This process causes many potential issues, such as ignition delay, ignition failure, combustion pressure peak or even chamber structure damage. However, knowledge in this aspect in order to address such issues is still limited. Therefore, a detailed investigation of the cryogenic fluids flashing phenomena has practical values.

### **1.3 The Methodology for the Research**

Considering the complexity of the flashing phenomenon, both experimental and numerical research has been performed in this project. The cryogenic propellant flashing test facility has been built in LTF-TUM. The high-speed Schlieren and Shadowgraph techniques were employed for the morphological study and the thermal behavior was obtained by thermocouples. The Global Rainbow Refractometry (GRR) for the first time was employed to study the cryogenic sprays, and both temperature and spray droplet size were measured. A Flashing Spray Model was developed and successfully implemented into the ANSYS solver under the Euler-Lagrange frame to simulate the flashing spray.

### **1.4 Outline of the Work**

The present work is outlined as follows:

Chapter 1 gives the general information of the present work, including the study objective, a brief background of the research program and the involved methodology.

Chapter 2 presents a comprehensive state of the art related to the flashing spray, including knowledge about the flashing spray and a literature review.

Chapter 3 illustrates in detail the flashing test bench, which includes the measurement techniques and experimental campaign. The test results are analyzed and discussed at length.

Chapter 4 describes the employment of the global rainbow technique in the cryogenic spray droplet study, and the spray droplet size and temperature are successfully measured.

Chapter 5 demonstrates a CFD simulation of the flashing spray and the developed and validated Flashing Simulation Model. The simulation results are in good agreement with the experimental data.

Chapter 6 summarizes the present work and provides a brief outlook for the future work.

Finally, the appendix is attached as the supplementary documents.

The schematic of the dissertation is shown as below:

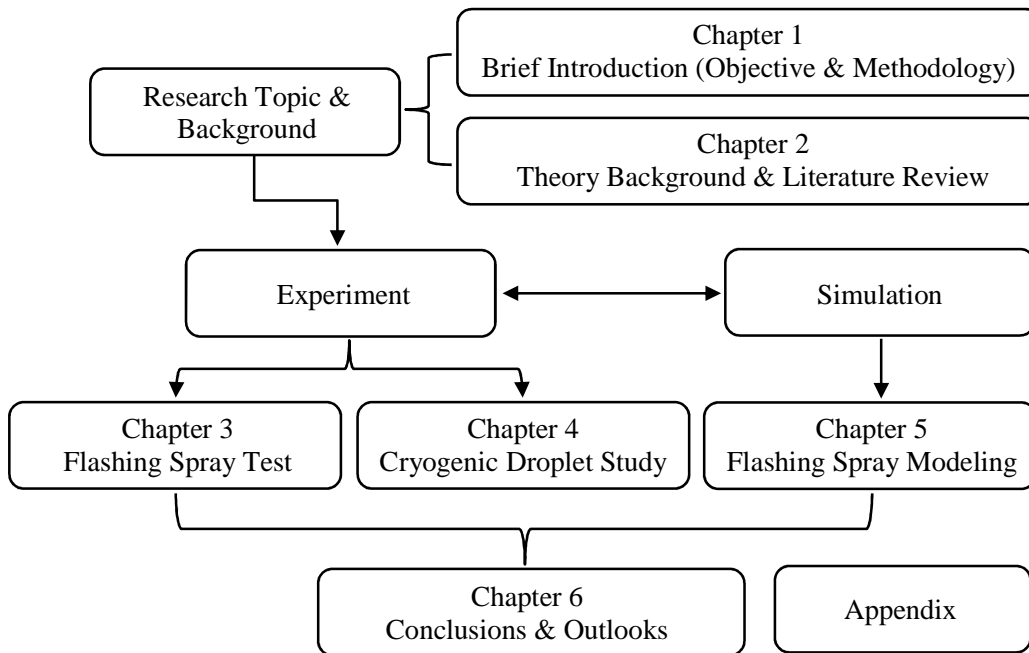


Fig. 1.1 Schematic of the present work



## Chapter 2. Background Theory and Literature Review

The objective of this study is to investigate the behavior of cryogenic fluids under low pressure conditions, which is heavily related to the degree of superheat of the fluids. This chapter is hence focused on the background theories of the superheated two-phase flow, including the thermodynamic process of the flashing spray and the kinetics of nucleation. Following the preparation of the basic knowledge, a comprehensive literature review on the flashing phenomena is also presented.

### 2.1 Liquid Oxygen/Liquid Methane Engine

Liquid rocket bipropellants can be classified by many ways: i.e. the hypergolic combinations such as MMH (UDMH)/NTO, and non-hypergolic combinations, like LO<sub>x</sub>/H<sub>2</sub>, LO<sub>x</sub>/RP1, LO<sub>x</sub>/ethanol and LO<sub>x</sub>/LCH<sub>4</sub>. The new millennium shows a renewed interest in methane as a liquid rocket propellant. It can be used in a wide range of liquid rocket engine (LRE) applications [2], with examples including the large booster engines, in-space Reaction Control Engines (RCE), Orbital Maneuvering Engines (OME), descent and ascent engines for planetary landers, and in-situ resource utilization compatibility on Mars. The early sporadic work on the methane engine can be traced back to the 1960s in the United States. Yet such propellants found little practical application except some research activities conducted by Aerojet. In the new decades, many institutes and space agencies shift their research emphasis on the new generation engines of methane/oxygen, such as the 870lbf thrust LCH<sub>4</sub>/LO<sub>x</sub> engine by Aerojet [2], the RS-18 engine with LO<sub>x</sub>/LCH<sub>4</sub> by NASA and Pratt & Whitney Rocketdyne [3], the OURAL program in French space agency and Russian space agency [4], the HYPROB program in Italian Aerospace Research Centre [5], the TEHORA program in Germany Aerospace Center (DLR) in cooperation with Astrium-ST and Russia [6], the Blue Engine (BE-4) development activities in the Blue Origin, the development of “Raptor” engine in the SpaceX, and also some activities in China Institute of Space Propulsion.

In sum, the potential in new rocket developments that support space exploration and the commercial market has revived an interest in methane/oxygen propulsion systems. This propellant combination offer multiple advantages, as listed below:

- 1). High specific impulse about 3600Ns/kg (~360s), as shown in Fig. 2.1
- 2). Non-toxicity

## 2. Background Theory and Literature Review

- 3) Low production cost
- 4). Capability of the fuel and oxidizer being stored at similar temperatures and relative ease of handling during launch vehicle
- 5). Less prone to develop combustion stability than LOx/RP1
- 6). Capability of offering potentially significant life cycle mission advantages compared to traditional rocket propellants

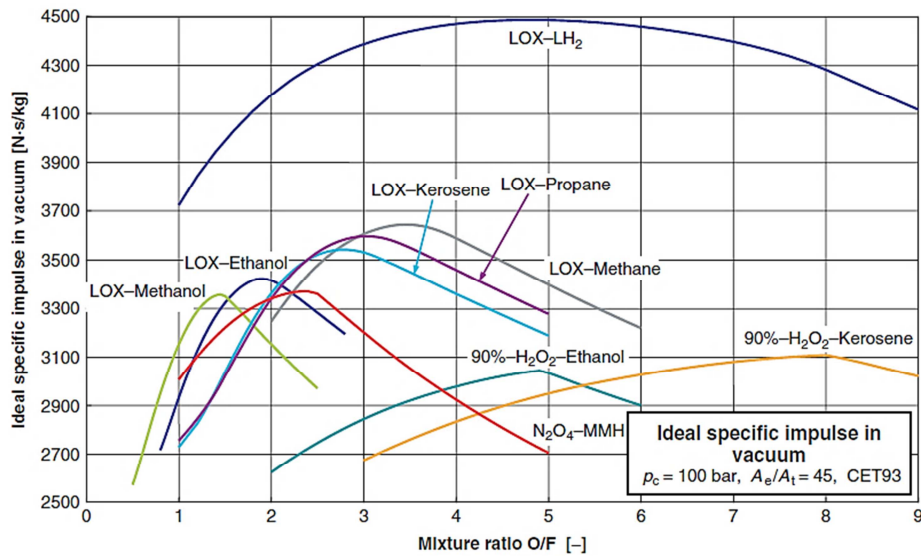


Fig. 2.1 Vacuum specific impulse of propellants

## 2.2 Thermodynamics of Superheated Fluid

### 2.2.1 Two-phase Flow State Criteria

According to the Entropy Maximum Principle or the Energy Minimum Principle, the equilibrium value of any unconstrained internal parameter is such as to maximize the entropy for the given total internal energy or to minimize the energy for the given total entropy. Inferentially, the two phases can coexist if they are in thermal, mechanical and chemical potential equilibrium, which requires the temperature, pressure and the chemical potentials of the coexisting phases are equal, respectively. It is shown as below:

$$T_1 = T_2, \quad p_1 = p_2, \quad \mu_1(p, T) = \mu_2(p, T) \quad (2.1)$$

The equilibrium states can be categorized into stable equilibrium, metastable equilibrium, and unstable equilibrium (see Fig. 2.2, as a schematic illustration). Physically, the stable equilibrium is achieved

when the free energy of a system at constant volume goes to the global minimum values. In such a state, any arbitrary perturbation will lead to the system restoring its initial state, termed as the absolute stable state. The metastable equilibrium state, however, can provide a higher internal energy, and it corresponds to a local minimum free energy. Such state is stable with respect to infinitesimal perturbations not changing qualitatively the initial state of the system. But with a larger perturbation, the system will evolve to the stable equilibrium state by overcoming the energy barrier (a local maximum free energy) after a certain time. This local maximum free energy is associated with an unstable equilibrium state, under which, any infinitesimal perturbations of the thermodynamic variables will lead to the system relaxing into a stable state.

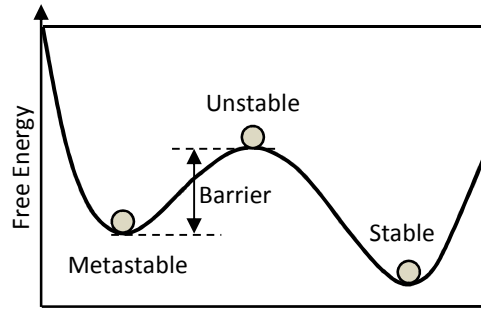


Fig. 2.2 Equilibrium state of two-phase flow

For a system at constant entropy and constant volume, the equilibrium state can be described as

$$(dU)_{eq} = 0 \tag{2.2}$$

where  $dU$  denotes infinitesimal small changes of the internal energy.

As for the stable equilibrium state, the condition of equilibrium (2.2) has to be supplemented by the requirement of stability with respect to finite perturbations,

$$(\Delta U)_{eq} > 0 \tag{2.3}$$

The symbol  $\Delta U$  refers to a finite change of the internal energy. Inequality (2.3) implies that the considered state corresponds to a minimum internal energy. When this condition is fulfilled for any arbitrary perturbations, the equilibrium state becomes absolutely stable. For infinitesimal perturbations, inequality (2.3) takes the form

$$(d^2U)_{eq} > 0 \tag{2.4}$$

In contrast, if inequality (2.4) is not fulfilled, the system will be in an unstable equilibrium state. Equation (2.2) and inequality (2.4) represent the necessary and sufficient conditions for a stable



As aforementioned, the metastable system restores its state with respect to infinitesimal perturbations. A value of the determinant equal to zero corresponds to the boundary of metastability and the transition of the system to states of essential instability of the phase under consideration. This boundary is the spinodal line (see ‘KCD’ curve in the figure). The spinodal is determined by the condition

$$-\left(\frac{\partial p}{\partial v}\right)_T = 0 \text{ and } \left(\frac{\partial T}{\partial s}\right)_p = 0 \quad (2.7)$$

The spinodal curve separates the metastable region from the unstable region.

### 2.2.3 Thermal Process of Flashing Spray

The flashing phenomenon involves a series of complex thermodynamic process, which occurs when a liquid deviates from the thermodynamic equilibrium and becomes superheated (metastable); namely, the liquid temperature is above the saturation temperature for the pressure surrounding it. It can be obtained either by sudden isothermal depressurization or by a careful isobaric heating. The thermodynamic process is illustrated in Fig. 2.3. In the present work, the flashing phenomenon is triggered mainly by the sudden depressurization. Initially, the liquid stays in subcooled or near saturated liquid region (see point “0” in  $p$ - $v$  figure). Under a sudden isothermal depressurization, the liquid will cross the saturation curve (point “1”) and shift to the metastable region at point “2”. As aforementioned, this state can not maintain a long time and with some disturbance, part of the fluid then reaches a new stable equilibrium state at point 2’ by nucleation or/and flash boiling, as shown in  $p$ - $v$  diagram in Fig. 2.3. If the liquid enters deeper into the metastable region, e.g. at point 3, where the spinodal line is, the massive homogeneous nucleation starts and an “explosive flashing” phenomenon will happen. The fluid undergoes to either the vapor stable state sides or to the liquid stable sides. In Fig. 2.3, the region inside the spinodal line (dash line in  $p$ - $v$  figure) is unphysical since the positive value of  $\partial p/\partial v$  is against the practical situation.

In the flashing study, the metastable liquid can be characterized either by its superheat with temperature difference  $\Delta T$  or with the pressure ratio  $R_p$ .  $\Delta T$  is defined as the temperature difference between the injection liquid temperature and the saturation temperature at the surrounding ambient pressure, as shown:

$$\Delta T = T_{inj} - T_{sat}(p) \quad (2.8)$$

The pressure ratio describes the ratio of injection saturation pressure at injection temperature to the ambient pressure, as shown:

$$R_p = p_{sat}(T_{inj}) / p_{amb} \quad (2.9)$$

Another parameter can also be used for the metastable state description, which is the Jakob number. Defined as the ratio of the available superheat energy to the required evaporation energy (latent heat of

vaporization), this parameter gives the possible vapor mass fraction after an isenthalpic phase change of a metastable liquid, as shown:

$$Ja = \frac{h_{l1} - h_{l2}}{h_{g2} - h_{l2}} = \frac{c_{pl}\Delta T_{l2}}{L_2} \quad (2.10)$$

Normally, the Jakob number is reduced by the liquid and vapor density ratio, as shown:

$$Ja^* = \frac{c_{pl}\Delta T_{l2}}{L_2} \frac{\rho_{l2}}{\rho_{g2}} \quad (2.11)$$

The Jakob number  $Ja$  of a metastable liquid is usually with a value in range of 0 to 1, which means that an adiabatic flashing is insufficient for the complete liquid vaporization. However, for the retrograde liquid, which possesses a large heat capacity, a complete evaporation upon adiabatic expansion is possible. At present work, the non-retrograde fluids (e.g. LN<sub>2</sub>, LOx and LCH<sub>4</sub>) are studied.

## 2.3 Kinetics of Nucleation

### 2.3.1 Bubble Formation in Superheated Liquid

Nucleation is the situation when a system (parent phase) is put into a non-equilibrium metastable state. For a metastable liquid study, the Classical Nucleation Theory (CNT) originally proposed in the early 1930s by Becker and Döring [8], works as a useful tool. The theory is based on the assumption of capillary approximation, according to which, the cluster is viewed as a large homogenous spherical droplet and the surface energy of the cluster is presented as the product of the planar interfacial tension. In the classical approach, Eq. (2.12) illustrates the formation energy of a nucleus with a radius  $r$ . The first term represents the interfacial energy between the phases, which is always positive since the formation of nucleus surface is energetically unfavorable. The second term is the difference in volume free energy between the phases. The energy for a nucleus formation is schematically shown in Fig. 2.4. It shows that with a small bubble radius, the surface energy dominates the nucleus formation. Conversely, the negative bulk contribution prevails when the nucleus is large. Thus, the formation energy has a maximum point ( $\Delta G^*$ ) corresponding to a critical cluster size. Mathematically,  $\Delta G^*$  and  $r^*$  can be estimated by  $d(\Delta G)/dr=0$ . The results are reported by Eq. (2.13) and Eq. (2.14) [9].  $\Delta G^*$  represents the energy barrier that a system has to overcome in order to establish a renewed stable phase. The nuclei with larger size than the critical nucleation cluster will on average grow up, while those smaller will on average collapse.

$$\Delta G = 4\pi r^2 \sigma - \frac{4\pi}{3} r^3 \Delta\mu \quad (2.12)$$

$$\Delta G^* = \frac{16\pi (v^l)^2 \sigma^3}{3 |\Delta\mu|^2} \quad (2.13)$$

$$r^* = -\frac{2\sigma}{\Delta\mu} \quad (2.14)$$

Considering the flashing conditions, in the metastable state (e.g. superheated liquid), the chemical potential in the bulk liquid is higher than that in the vapor, which makes it thermodynamically favorable to transform from the parent phase (superheated liquid) to the daughter phase (vapor). The driving force of this transformation is the chemical potential difference between the liquid and vapor phases, as illustrated:

$$\Delta\mu = k_B T_{inj} \ln(R_p) \quad (2.15)$$

The steady state nucleation rate is an exponential function of the energy barrier, as shown:

$$J = J_0 \exp\left(-\frac{\Delta G^*}{k_B T}\right) \quad (2.16)$$

$$J_0 \cong \frac{\rho_v^2}{\rho_l} \sqrt{\frac{2\sigma}{\pi m_l}} \quad (2.17)$$

where  $J_0$  is the pre-exponential factor. The nucleation rate is far less sensitive to  $J_0$  than to the value of the energy barrier [10]. Lubetkin [11] pointed out that only 4% decrease of  $\Delta G^*$  will lead to an increase by an order of magnitude in the nucleation rate  $J$ .

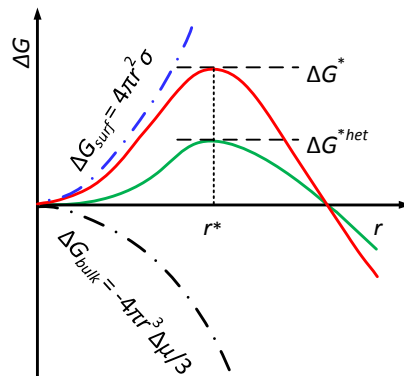


Fig. 2.4 Homogeneous and heterogeneous nucleation barrier

## 2. Background Theory and Literature Review

---

The aforementioned nucleation refers to the homogeneous nucleation, under which the liquid will reach the superheat limit and present explosive atomization sprays. However, in most of the cases, the heterogeneous rather than homogeneous nucleation happens. In the heterogeneous nucleation process, to form a nucleation cluster less energy is needed, since the required energy to form a new surface can be compensated by the existing surface in the system. The heterogeneous nucleation barrier is estimated by multiplying a factor  $f(\varphi)$  to the homogeneous energy barrier, as shown:

$$\Delta G^{*het} = f(\varphi)\Delta G^* < \Delta G^*, f(\varphi) < 1 \quad (2.18)$$

where  $\varphi$  is the contact angle between the nucleus and the extrinsic object.

### 2.3.2 Bubble Growth in Superheated Liquid

From the previous study, we know that the nucleate boiling plays an important role in the flashing spray. The massive bubble growth is energetically favorable when the nucleus size exceeds the critical nucleus size. Considering that a critical bubble stays inside of a superheated liquid bulk in the thermal dynamic equilibrium, its critical size can be estimated by the Gibbs-Duhem equation and Laplace equation, as shown in Eq. (2.19) and Eq. (2.20) [12].

$$r^* \cong \frac{2\sigma v_l}{RT \ln(p_{sat}/p_v)} \quad (2.19)$$

$$p_v = p_{sat} \exp\left(\frac{v_l}{RT}(p_\infty - p_{sat})\right) \quad (2.20)$$

In equilibrium, the pressure inside the bubble is higher than that of the fluid outside due to the surface tension compensation. However, the temperature of the bubble remains saturated and is lower than that of the bulk superheated liquid. The amount of superheat required to keep a bubble with the size  $r$  at equilibrium is shown as below:

$$\Delta T = \frac{2RT_{sat}^2 \sigma}{h_v p_l r} \quad (2.21)$$

The bubble growth is dependent on both of the mechanical equilibrium and thermal equilibrium. Shortly after the bubble formation, the growth is caused by the differential pressure force, the bubble expands and the gas pushes the surrounding liquid away. This stage is so-called the inertia-controlled growth stage. The growth rate is limited by the restraining effect of the surface tension and this effect will become less important with the bubble growing. If the initial superheat is sufficient, the limiting factor in the following state will be the liquid inertia, and the growth can be described by the Rayleigh equation, as shown:

$$\left. \frac{dr}{dt} \right|_{inertial} = \sqrt{\frac{2 p_v(T_\infty) - p_\infty}{3 \rho_l}} \quad (2.22)$$

Along with the growth of the bubble, the superheated liquid vaporizes and refills the bubble. The heat flux to meet the latent heat requirement is proportional to  $r^2 dr/dt$ . Therefore, the initial growth stage is followed by an intermediate stage, in which both inertial and thermal effect will control the bubble growth [13]. Finally, as the bubble grows, the inflow of thermal energy will dominate the process, namely heat transfer-controlled growth stage. Considering the balance between the heat flux from the liquid to the bubble surface and the latent heat required to supply the vapor in the bubble, Plesset et al. [14, 15] proposed a correlation for the thermal growth velocity, as shown:

$$\left. \frac{dr}{dt} \right|_{thermal} = \sqrt{\frac{3}{\pi \alpha}} \frac{\lambda}{L \rho_v(T_b)} \frac{T_\infty - T_b}{t^{1/2}} \quad (2.23)$$

where  $L$  is the latent heat and  $\alpha$  is the thermal diffusivity of the liquid.

Assuming a spherical bubble and an incompressible, constant-property inviscid flow, by integrating Eq. (2.22) and Eq. (2.23), we can see that the inertial-controlled bubble growth is linear with time ( $r \propto t$ ) and that the bubble size is in proportion to  $t^{1/2}$  in the thermal-controlled stage ( $r \propto t^{1/2}$ ).

In order to describe the bubble growth over the whole range, Mikic et al. [16] combined the inertia-controlled growth and heat transfer-controlled growth by employing the linearized Clausius–Clapeyron equation to estimate the vapor pressure, i.e. Eq. (2.24), and gave the expression for the bubble size evolution, shown as Eq. (2.25).

$$p_v - p_\infty = \rho_v L \frac{T_v - T_b}{T_b} \quad (2.24)$$

$$r^+ = \frac{2}{3} \left[ (t^+ + 1)^{3/2} - (t^+)^{3/2} - 1 \right] \quad (2.25)$$

$$r^+ = \frac{r}{B^2/A}, \quad t^+ = \frac{t}{B^2/A^2} \quad (2.26)$$

$$A = \left[ \frac{2 (T_\infty - T_b) L \rho_v(T_b)}{3 T_b \rho_l} \right]^{1/2}, \quad B = \left[ \frac{12}{\pi} Ja^2 \alpha \right]^{1/2} \quad (2.27)$$

It can be seen that, for  $t^+ \ll 1$ , Eq. (2.25) gives the results of Rayleigh solution (i.e. Eq. (2.22)), whereas for  $t^+ \gg 1$ , the asymptotic solution of Plesset model (i.e. Eq. (2.23)) is obtained. Some other similar models are also proposed to predict the bubble growth, e.g. the model proposed by Theofanous and Patel

[17], and the model given by Miyatake and Tanaka [18]. Fig. 2.5 illustrates the prediction results by these models for water bubble growth.

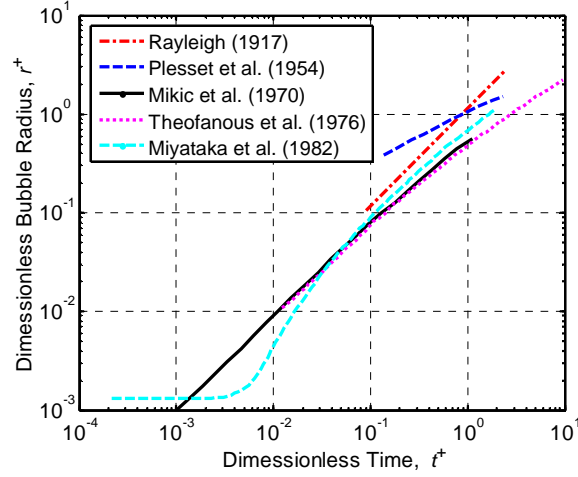


Fig. 2.5 Predicted bubble growth (adapted from Ref. [17, 18, 19])

## 2.4 Flashing Atomization Correlations

The early research exploring the flashing spray atomization models (correlations) is limited to the spray under low superheat conditions, where the mechanical jet break-up is thought to predominate and the nucleate boiling effect is almost negligible. Brown and York [20] and Kitamura et al. [21] have reported that there is little or no discernible difference in the jet atomization between under low superheat conditions and under mechanical break-up conditions. In this section, the atomization models under moderate or high superheat conditions will be discussed. Actually, the atomization models of the flashing spray under these conditions are still limited and some semi-empirical correlations have been developed. Brown and York [20] investigated in detail the flashing phenomena and proposed a correlation to predict the droplet size based on the Freon-11 and water tests, as shown:

$$\bar{D}_{30} (\mu m) = \frac{1840 - 5.18T(^{\circ}F)}{We} \quad (2.28)$$

where  $T$  is the spray injection temperature and  $We$  is the Weber number.

Nagai et al. [22] proposed a promising atomization correlation by taking into account the injector geometric parameters and a dimensionless superheat.

$$D_{32}(\mu m) = \begin{cases} 36.8(\Delta T^*)^{-2.58}, & (L/D < 7 \& 0.55 < \Delta T^* < 1.0) \\ 70.4[-1 + 0.14(L/d_0)]^{-0.22} d_0^{0.72} (\Delta T^*)^{-0.38}, & (L/D > 7.8 \& 0 < \Delta T^* < 0.55) \\ 39.1[-1 + 0.14(L/d_0)]^{-0.22} d_0^{0.72} (\Delta T^*)^{-1.33}, & (L/D > 7.8 \& 0.55 < \Delta T^* < 1.0) \end{cases} \quad (2.29)$$

$$\Delta T^* = \frac{T_{inj} - T_{sat}(P_\infty)}{T_{sat}(P_{inj}) - T_{sat}(P_\infty)} \quad (2.30)$$

Cleary et al. [23] came up with a transition model for the flashing atomization, which gives general information about the droplet size in the fully flashing spray, as estimated below  $30\mu m$ . The authors also proposed a correlation of the droplet size based on the dynamic parameters. Johnson and Woodward [24] gave a spray atomization model which assumes the droplet size to be the minimum of mechanical breakup and flashing breakup, as shown:

$$D_d = \min\{D_m, D_f\} \quad (2.31)$$

$$\begin{cases} D_m = We_{crit} \sigma_l / (u^2 \rho_\infty) \\ D_f = 0.883 \times 10^{-3} - 0.0734 \times 10^{-3} \ln(E_p) \end{cases} \quad (2.32)$$

where  $E_p$  is the partial expansion energy. It is a complex function of enthalpy and pressure, which can be found in Ref. [24].

van den Bosch and Duijm [25] proposed another correlation based on the spray jet velocity, viscosity and surface tension, as shown:

$$D_d = \begin{cases} 1.89 D_f \sqrt{1 + 3We_f^{0.5} / Re_f}, & (if \ We_f < 10^6 \ Re_f^{-0.45} \& T_0 < 1.11 T_{sat}(P_\infty)) \\ \frac{C_{ds} \sigma_l}{u_f^2 \rho_\infty} \end{cases} \quad (2.33)$$

where  $D_f$  is the jet diameter,  $u_f$  is the jet velocity after flashing,  $We_f$  and  $Re_f$  refer to the jet Weber number and Reynolds number, respectively,  $T_0$  is the spray temperature at the injector exit,  $\sigma_l$  is the liquid surface tension,  $\rho_\infty$  is the ambient gas (air) density and  $C_{ds}$  is a constant with a recommended value of between 10 and 20.

Gemci et al. [26] investigated flashing atomization with hydrocarbon solutions of n-hexadecane and n-butane, with nitrogen as the propellant gas. The authors proposed a correlation to predict the droplet size, as shown:

$$D_{32}(\mu m) = 118.4 - 28.3(\Delta T^* - K) \quad (2.34)$$

$$K = \frac{2(p_\infty - p_v)}{\rho u^2} \quad (2.35)$$

where  $\Delta T^*$  is the dimensionless degree of superheat, defined in Eq. (2.30),  $K$  is the cavitation number, which illustrates the resistance of the flow to cavitation,  $p_\infty$  and  $p_v$  are the ambient pressure and the vapor pressure at the injector orifice, respectively, and  $\rho$  and  $u$  respectively are density and velocity of the liquid–gas mixture.

## 2.5 Flashing Spray Morphology

Flashing spray is typically different from the classical atomization. The previous studies show that the superheat nucleate boiling plays a major role in the spray break-up when flashing occurs. Fig. 2.6 gives the LN<sub>2</sub> flow patterns under different pressure conditions, where three different atomization regimes are presented. The image in the middle features the LN<sub>2</sub> spray injected into a subcritical pressure environment, showing plenty of clear droplets disintegrated at the spray jet surface. This jet breakup is ascribed to the interaction between the dynamic shear force and surface tension. As the ambient pressure approaches and exceeds the critical pressure ( $p_{cri}=3.4\text{Mpa}$ ), the lack of the surface tension and of distinct interfacial structure promotes diffusion-dominated mixing before atomization, as shown in the right image. Under low-pressure conditions (see the left image), the spray shows a totally different scenario, as the spray presents a large open angle and the atomization occurs even inside the spray jets, termed as the flashing atomization.

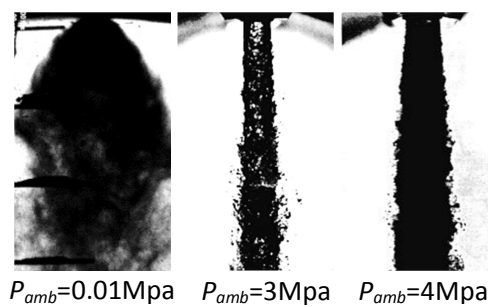


Fig. 2.6 LN<sub>2</sub> spray under different pressure conditions. From left to right: vacuum condition (Ref. [27]), subcritical injection and supercritical condition (adapted from Ref. [28])

Fig. 2.7 shows water spray atomization process at different temperatures with a splash-plate injector. The spreading liquid sheet is formed by the impingement effect of the liquid on the injector solid plate. It can be seen that, at the low temperature the spray merely forms an intact liquid sheet without disintegration due to the absence of flashing at this temperature. With the temperature increasing, so does the liquid

superheat, the liquid sheet starts to break up and larger liquid ligaments also appear. Accompanying with the continuous increase in the temperature, e.g.  $T=119^{\circ}\text{C}$ , the flashing dominates the jet break-up and almost no liquid sheet exists at this moment, and the jet disintegrates into small droplets.

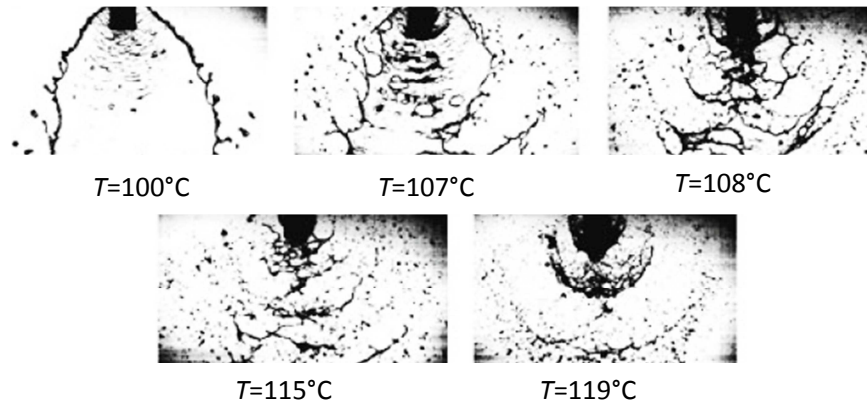


Fig. 2.7 Water spray under different superheat conditions with splash-plate injector (adapted from Ref. [29])

The former spray morphology mainly appears under moderate superheat conditions. When the superheat is extremely high, e.g. close to the spinodal line, the homogeneous nucleation will occur and trigger the explosive atomization and vaporization. In addition, the evaporation wave may be observed under the high superheat conditions. Viera and Moreira [30] conducted an experiment on iso-octane spray jet under different superheat conditions (characterized by pressure ratio  $R_p$ ) with single-hole jet injector. Fig. 2.8 shows the Schlieren images of the test data. The liquid jet undergoes a process of fierce atomization with the superheat degree increasing. Under very high superheat conditions, e. g.  $R_p=330$ , on account of the violent vaporization, the shock wave structures were observed surrounding the jet core. In the experiment, the authors argued that the flashing occurred on the surface of the liquid jet via an evaporation wave process. The two-phase iso-octane flow accelerated to acquire a local sonic speed downstream the injector, and then expanded to supersonic velocity and finally terminated this expansion process with the shock wave structures.

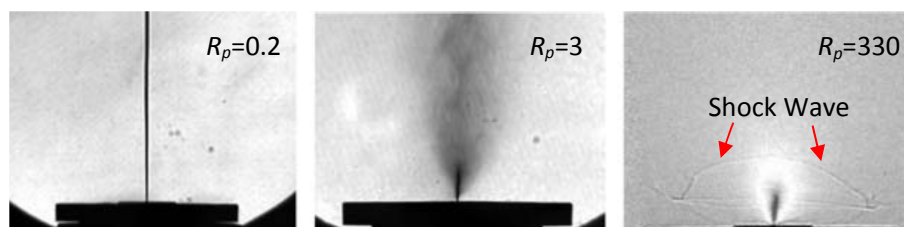


Fig. 2.8 Iso-octane spray under different superheat conditions with single-hole jet injector (adapted from Ref. [30])

## 2. Background Theory and Literature Review

---

These high superheat evaporation-induced shock waves are also observed by Lamanna et al. [31] in the study of acetone flashing sprays. Fig. 2.9 illustrates the clear structures of the shock waves, which is a result of the explosive expanding during the flashing phenomenon under extremely large superheat conditions ( $R_p=1124$ ).

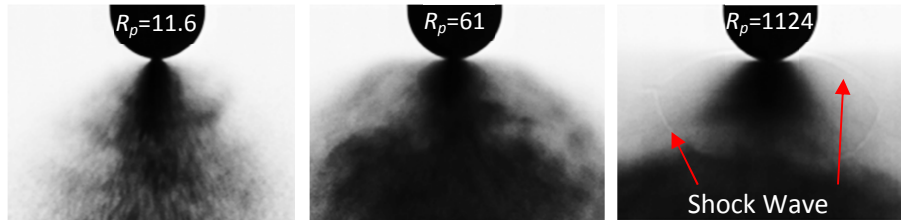


Fig. 2.9 Acetone spray under different superheat conditions with single-hole jet injector (adapted from Ref. [31])

## 2.6 Literature Review of Flashing Spray

The former sections summarize the knowledge related to the flashing spray, including the thermal dynamics and nucleation theory. This section, as a supplement, reviews the notable research works (both of experimental and numerical investigation) contributing to the understanding of a flashing spray.

### 2.6.1 Experimental Study of Flashing Spray

The research work on flashing can be traced back to the 1960s, when Brown and York [20] explored the flashing spray with water and Freon-11. The authors found that a critical superheat exists, and over this threshold, bubble growth inside the liquid jet will occur. Since then many valuable studies have been carried out to further expand the knowledge of flashing. A brief summary of the previous works from the experimental perspective is listed as below.

#### 2.6.1.1 Investigation in Flashing Spray Mechanism

Reid [32] did an early work in the 1970s to explore the potential mechanism of the vapor explosion that is induced by the sudden depressurization of a pressurized liquid tank. The author hypothesized that the vapor explosion occurs until the liquid superheat reaches its limit, and that before this point, only rapid boiling process happens. And the explosion intensity is related to the pressure difference between the vapor saturation line and the superheat limit curve.

In the early 1980s, Shepherd and Sturtevant [33] investigated the bubble evaporation process inside a single butane droplet under superheat limit conditions with a short explosion photography technique. The bubble interfacial instability driven by the rapid evaporation was observed, which is similar to the Landau mechanism of laminar flame instability. The authors found that the evaporation mass flow rate was much higher (about two orders of magnitude) than the one predicted by normal evaporation law. Additionally, a series of toroidal waves on the bubble-liquid interface were also found, and the induced surface oscillations yield a disintegration of the droplets by Rayleigh-Taylor instability.

The different flashing spray regimes were studied by Kitamura et al. [21] with water and ethanol. The authors observed two different spray patterns: a complete flashing and a normal two-phase spray. The former one happens at much higher temperature than the saturation temperature, and the latter one occurs closer to the saturation temperature. The authors proposed an empirical correlation of critical superheat for the flashing spray on the basis of the bubble growth theory. Cleary et al. [23] and Witlox et al. [34] proposed and validated an empirical correlation using the Weber number and Jacob number to predict the onset of water flashing atomization. To further describe the flashing spray pattern, Reitz [35] conducted experiments by injecting water into a heated air environment. The tests show that the flashing pattern rather than directly disintegrates at the injector orifice as the previous study concluded, but comprises an intact liquid core surrounded by a diverging fine spray. Furthermore, Peter et al. [36] characterized the flashing liquid jet by four physical features, namely, non-shattering liquid jet, partially shattering jet, completely shattering jet but in statewide sequence, and flare flashing jet. The authors pointed out that the spray temperature along the jet axial direction showed an exponential decrease. By consideration of the flow both inside and outside the injector, Park and Lee [37] identified two flashing modes (internal flashing mode and external flashing mode) through an experiment with water. The authors found that a long injector and a high superheat help to produce fine and uniform spray droplets.

By measuring the vapor concentration of n-pentane flashing spray with an infrared extinction/scattering (IRES) technique, Adachi et al. [38] proposed an empirical correlation of the flashing evaporation mass flow rate and developed and validated a flash boiling spray model.

Simoes-Moreira et al. [39] studied the flashing liquid jet released from a short injector into a low pressure environment with the Schlieren technique. The authors observed the phase transition appearing on a liquid core surface outside the injector and no internal nucleation was observed. The phase change forms an interfacial region, where the expansion waves may be generated depending on the superheat degree. By a theoretical analysis, the authors suspected that as the metastable liquid experiences a sudden evaporation on the interface, a two-phase flow emerges. This two-phase flow will freely accelerate to a supersonic velocity. Due to the ambient pressure balance, the spray acceleration process will terminate with shock waves.

Employing Laser-Induced-Exciplex-Fluorescence (LIEF) and Mie-scattering techniques, Zeng et al. [40] investigated the flashing spray released from a multi-hole injector. The spray penetration length, plume width, and normalized plume distance were analyzed to characterize the macroscopic spray structure. The authors gave two critical superheat values (represented by a ratio of ambient pressure to saturation pressure) to respectively characterize the flash-boiling regime and the spray collapsing transition regime.

Lamanna et al. [31] conducted a series of experiments to investigate the flashing spray under low pressure conditions with ethanol, acetone and iso-octane. Dependent on the superheat degree, the authors defined three atomization regimes, namely, the mechanical atomization regime, the nucleation onset regime and the fully flashing regime. Based on the nucleation theory, the authors also proposed a non-dimensional parameter (Gibbs number) for these regimes indication.

### 2.6.1.2 Investigation in Flashing Spray Velocity and Droplet Size

Brown and York [20] studied the spray droplet sizes, velocities and spray shape with different injectors, and hence proposed a correlation of the droplet size distribution. Park and Lee [37] measured the droplets of a flashing spray with Malvern Particle Analyzer (MPA). The distribution of the droplet size near the injector presents a decreasing trend in the spray radial direction, but becomes more uniform downstream the spray. Hervieu and Veneau [41] measured the droplet size and velocity of the propane flashing jets by employing a Phase Doppler Particle Analyzer (PDPA). The results show that higher injection pressures facilitate flashing spray, leading to strong fragmentation and small droplets. The Arithmetic Mean Diameter ( $D_{10}$ ) of the typical droplets falls in the range from  $10\mu\text{m}$  to about  $50\mu\text{m}$  under the fully flashing conditions.

Allen [42, 43] investigated the spray velocity and droplet size distribution of propane flashing jet with non-intrusive optical measurement techniques. The author characterized the flashing spray velocity profile with the Laser Doppler Velocimetry (LDA) technique. Though it is rather difficult to get the valid data on account of the harsh spray conditions, with some carefully post-processing, the author obtained the velocity profiles along the axial centerline as well as the lateral profiles at various axial locations. The profiles show the feature of a self-similarity along the spray axial centerline and with Gaussian velocity in the spray radial direction. As to the droplet size measurement, the author utilized an improved Malvern Particle Analyzer (MPA) system, and the droplet Sauter Mean Diameter ( $D_{32}$ ) is smaller than about  $65\mu\text{m}$  under flashing conditions.

Yildiz [44] carried out a comprehensive study to characterize R-134A flashing atomization with Particle Image Velocimetry (PIV) and Phase Doppler Anemometry (PDA) techniques. The author analyzed the influence of injector geometry and injection boundary conditions on the droplet size and the velocity distributions. The test also gives a self-similarity of the velocity distribution as Allen [42] did. This velocity self-similarity was also confirmed by Vu et al. [45] and Zhou et al. [46] in the R134a flashing study, and by Kamoun et al. [47] in the ethanol and acetone flashing study. Weber and Leick [48] studied the near-injector flashing spray structures respectively with a single-hole and two-hole GDI-injectors. The droplet velocities were obtained by applying a shadow particle image velocimetry (PIV) technique, and the droplet sizes were qualitatively estimated by the image analysis. With an intensive study, Lamanna et al. [49] pointed out that in fully flashing sprays, the enhanced evaporation induces a narrowing Rosin-Rammler distribution with the statistically  $D_{32}$  less than about  $25\mu\text{m}$ .

### 2.6.1.3 Investigation in Flashing Spray Temperature

Peter et al. [36] investigated the temperature distribution along the flashing spray centerline by thermocouples. The test showed an exponential decrease in the spray mean temperature along the jet axial direction. A similar temperature distribution was obtained by Vetrano et al. [50, 51], who used Planar Laser Induced Fluorescence technique (PLIF) to investigate the thermal characteristics of flashing jets of ethanol and acetone. The test shows that as the Jakob number increases (superheat increases), the temperature curve presents a steeper decline. The superheated liquid jets travel a rather short distance (i.e.  $z/D < \sim 20$ ) and then almost relax to an equilibrium stable state.

By employing both intrusive and non-intrusive techniques, Yildiz [44] investigated the temperature evolution of the R134a flashing sprays. As to the non-intrusive methods, the infrared thermography and global rainbow thermometer (GRT) were used. The lacking of information of the local distribution of the spray emissivity makes it challenging to recompute the accurate spray temperature based on the infrared radiation. In this case only qualitative results were provided by the infrared thermography. The thermocouple, however, disturbs the spray jets and affects the flashing onset and consequently, may lead to temperature misinterpretation downstream. With these measurements, the author gave an exponential decay relationship of the spray temperature along the spray centerline. By employing a laser diffraction technique, i.e. global rainbow thermometer, the author also conducted a feasible study on the flashing spray [52]. The experiment recorded a weak signal of the global rainbow interference patterns, from which the temperature and spray droplet size are retrieved. The results, however, deviate from the value measured by thermocouples. Considering the disadvantage of the infrared thermography, the Dual Infrared Thermography (DIT) technique was employed for the spray thermal study by Kamoun et al. [53] and Lamanna et al. [54]. This technique can be seen as an improved Infrared Thermography since the ambient radiation can be eliminated. By analyzing two distinct images of the spray at two different temperature-controlled backgrounds with a high emissivity, the local emissivity of the fluid and then the spray temperature can be estimated. One disadvantage of this technique is the sensitivity to the repeatability of spray atomization process, and to the ambient radiation. The tests also show an exponential decay of temperature along the spray centerline, and a self-similarity of the velocity profiles in radial direction for the flashing spray.

The above discussed studies are concentrated on storable fluids. However, little research on the cryogenic fluid spray under a low pressure environment (far away from the critical condition) has been undertaken so far. Gautam et al. [55, 56] investigated the behavior of transient and steady LN<sub>2</sub>/He coaxial injection spray under atmospheric and sub-atmospheric pressure conditions, using the high-speed Mie-scattering and Schlieren techniques. The authors demonstrated that the behavior of LN<sub>2</sub> is significantly affected by the low-pressure conditions. The spray presents an extremely wide expansion in such environment. Manfletti [57] employed the Schlieren visualization method to study the impact of pre-ignition conditions (such as pressure, cryogenic injection, and the local chamber flow field) on the altitude ignition process. The LOx flashing phenomena in a low chamber pressure environment (25 mbar) were observed and further analysis of the phenomenon was conducted. Lamanna, et al. [58] explored the flashing behavior of LOx and liquid ethanol, and found similar spray characteristics despite the difference in fluid properties, and also pointed out that the kinetic phase transition dominates the flash atomization under the boundary condition of high superheat level. Recently, Luo et al. [27, 59, 60,

## 2. Background Theory and Literature Review

61] conducted a series of experiments of the LN<sub>2</sub>, LOx and LCH<sub>4</sub> flashing spray and the characteristics of such spray were analyzed.

The flashing spray characteristics, such as the spray atomization mechanism, the spray temperature, the spray velocity, and the droplet size distribution are reviewed in the above sections. The adopted measurement techniques are summarized and listed in Tab. 2.1.

Tab. 2.1 Typical measurement methods used in flashing spray

Characteristics	Spray pattern	Temperature	Droplet size	Velocity
Methodology	Photography (Brown and York [20], Reitz [35], Shepherd and Sturtevant [33], Kitamura et al. [21], Yildiz [44], karami et al. [29]) Shadowgraph/Schlieren (Vieira and Simoes-Moreira [30], Simoes-Moreira et al. [39], Lamanna et al. [31], Weber and Leick [48], Luo and Haidn [27, 59])	PLIF (Vetrano et al. [50] [51]) DIT (Kamoun et al. [53] Lamanna et al. [54]) GRT (Yildiz et al. [52])	MPA (Park and Lee [37], Allen [43]) PDA (Yildiz [44]) GRT (Yildiz et al. [52])	PDA/PDPA (Allen [42], Hervieu and Veneau [41], Yildiz [44]) PIV (Yildiz [44], Weber and Leick [48])

### 2.6.2 Numerical Study of Flashing Spray

As aforementioned, the flashing phenomenon is a complex non-equilibrium phase change process; hence, modeling of such two-phase flow remains a great challenge. Nevertheless, plenty of simulation works has been performed to study such sprays.

Among the efforts, a number of numerical works is focused on the geometrically confined flashing flows (e.g. flows inside injectors). Two methods, i.e. the thermal equilibrium method and the thermal non-equilibrium method were developed in accordance. The thermal equilibrium method such as Homogeneous Equilibrium Model (HEM), takes the two-phase mixture as a pseudo-fluid of single-component flow with the same properties, velocity, pressure and temperature. Goldstein [62] did an early work to simulate the flashing flow through a capillary tube by assuming an adiabatic and homogeneous flow condition. Inada and Ohkawa [63] included flashing effects in the HEM model for two-phase flow by assuming that the liquid saturation enthalpy is linearly dependent on the local pressure, and that all other fluid properties are assumed to be independent of the pressure.

Leung [64] was the first to propose a generalized correlation for one-component equilibrium flashing choked flow. By introducing a  $\omega$ -parameter based on the assumption of isothermal state change of the two-phase flow, the deviations of the critical mass flow rate predicted by  $\omega$ -method and the HEM method are up to 20%. Later, Leung [65] improved this  $\omega$ -parameter formulation by considering the compressible nature of a two-phase flow, and Lenzing et al. [66] performed a detailed study by comparison of these two  $\omega$ -parameter methods with the HEM method.

The HEM model can predict rather accurate critical mass flow rate of the flashing flow in long injectors since the two-phase fluid has sufficient time to reach an equilibrium state. This model, however, underpredicts the critical mass flow rate in short injectors, where the flow is mainly characterized by thermal and mechanical non-equilibrium. Consequently, the thermal non-equilibrium models have been developed, such as Homogeneous Relaxation Model (HRM). In essence, this model presumes that the vapor temperature equals to the saturation temperature but is different from the surrounding liquid phase temperature. This model also represents the phase transition with one equation by estimating the time-scale of the phase change. The HRM model was first applied for adiabatic, one-dimensional flashing spray by Bilckli and Kestin [67] and later is widely used. Schmidt et al. [68] employed the HRM model in a two-dimensional flashing flow, and the simulation shows a good agreement with the experiments. Later, Gopalakrishnan and Schmid [69] successfully performed both a two- and three-dimensional flashing simulation with this model. The authors incorporated the HRM into the pressure equation to satisfy the compressibility and density change because of the phase transition. The simulation results show a geometrically-induced phase change near the injector entrance and at the injector orifice plane, and this phase transition is quite sensitive to the spray temperature. By extending Gopalakrishnan and Schmidt's work, Neroorkar et al. [70] performed a three-dimensional flashing simulation of a pressure swirl injector with consideration of temperature-dependent fluid properties. The simulation was qualitatively validated by the experimental data by Schmitz et al [71]. Saha et al. [72] studied the internal and near-injector two-phase flow with a GDI injector by coupling the HRM model with the VOF method. The simulation predicts cavitation inside the injector and flash boiling in the near-injector region, when the liquid jet is subjected to the superheated ambience.

Regarding the external flashing spray, however, few modeling work has been carried out so far. Simoes-Moreira and Bullard [73] conducted a one-dimensional simulation of a flashing jet with short injectors. Due to the rapid depressurization, the liquid jet undergoes a sudden phase change via an evaporation wave process, producing complex flow structures downstream a liquid core near the injector orifice. The author pointed out that the radial evaporation wave shows the Chapman–Jouguet (C-J) solution and the choked flow downstream of the wave is also well predicted. Later, Angelo et al [74] improved Simoes-Moreira and Bullard's work, and performed a two-dimensional simulation of a flashing jet. The simulation can well predict the main shape and dimensions of the complicated shock wave structures, and the results are comparable with the experimental data.

Based on Adachi-correlation [38], Zuo et al. [75] developed a flashing atomization and evaporation model to perform a 3D simulation of the flashing spray released from a pressure-swirl injector. The model gives consideration to the mass evaporation both due to flash boiling and heat transfer (conduction and convection) between the superheated liquid and its surrounding ambience. Specifically, the spray sheet flash boiling is molded by a transient heat conduction process with an effective thermal conductivity. The jet atomization is modeled by the hydrodynamic instability, cavitation and bubble growth inside the spray sheet. The droplet evaporation is modeled with consideration of the heat transfer under flash boiling and normal boiling conditions. The simulation results match well with the Mie scattering images. This model has later been adopted and/or improved by Raju [76], Schmehl and Steelant [77], Ramcke and Pfitzner [78, 79], and Luo et al. [80] for the flashing spray CFD study and the model shows good computational results in comparison with the experimental data.

### 2.7 Summary

Since  $\text{LCH}_4/\text{LOx}$  has more advantages than its counterparts, the green Methane-Oxygen engine attracts more attention in the new generation engines. A deep understanding of the flashing phenomenon involved in the green propulsion development is therefore required. This chapter comprehensively reviews the previous research related to the flashing spray. The thermodynamic process, the kinetics of nucleation, the atomization models and the macroscopical characteristics of the flashing spray are discussed, which is then followed by a comprehensive review. The literature studies show that the quantitative characterization of the two-phase flow under flashing conditions is rather complex, and still remains a great challenge even for the most applied laser-based measurement techniques (e.g. PDA, LDA, LIF, GRT, and DIT). The related research on the cryogenic flashing spray is hence quantitatively limited. As to the modeling of the two-phase superheat spray, a majority of work is focused on the internal flashing phenomena inside a confined injector or pipe. The study on detailed characteristics such as the morphology, thermal behavior, droplet size distribution of the external cryogenic flashing spray is still lacking.

# Chapter 3. Experimental Investigation of Cryogenic Flashing Spray

## 3.1 Introduction

This chapter presents an experimental investigation of flashing sprays of cryogenic fluids, e.g. LN<sub>2</sub>, LO<sub>x</sub> and LCH<sub>4</sub>. The flashing test bench will be described, followed by a detailed discussion of the test results. With the help of a high-speed shadowgraph and Schlieren techniques, as well as the temperature measurement, the characteristics of the flashing spray are investigated, including the spray evolution process, the spray angle, the spray thermal behaviors along the injection centerline, and, in some cases, the formation of solid particles.

## 3.2 Experimental Facilities

### 3.2.1 Flashing Test Facility

#### 3.2.1.1 Test Facility Overview

The flashing test facility has been built in LTF-TUM. The setup is designed to perform the studies of flash atomization and vaporization of cryogenic fluids in a low pressure environment (down to about 30mbar). Fig.3.1 shows the detailed schematic of the flashing test facility, which corresponds to the test setup in Fig. 3.2. The setup mainly consists of 5 parts: the main test cell, the fluid liquefaction system, the gas pressurization and cryogenic feeding system, the DAQ system and the optical diagnosis system.

In general, at the beginning the nitrogen gas (stored in cylinder bundles with a high pressure of up to 30Mpa) is depressurized by the spring-loaded pressure regulator (P\_Reg1) in order to purge the chamber and the corresponding delivery lines. After that the vacuum pump starts to evacuate the whole system. This purge and evacuation process will be repeated several times to prevent water moisture inside the delivery line from freezing at the extremely low temperature during the test (e.g. ~78K). The oxygen gas (stored with a high pressure of up to 30Mpa) and the methane gas (stored with a pressure up to 20Mpa)

### 3. Experimental Investigation of Cryogenic Flashing Spray

are depressurized by the pressure regulators P\_Reg2 and P\_Reg4, respectively, thus providing the liquefaction gas sources. The gases are liquified in the liquefaction system, which will be described later in detail. The liquefied fluids are then delivered and filled into the vacuum insulated tanks, namely the LOx and LCH<sub>4</sub> tank. Their tank pressures are closed-loop controlled by the solenoid valves and relief valves, i.e. MV-LO2, MV-LM2, P\_RV2 and P\_RV1. The solenoid valves are controlled with a prescribed pressure threshold and a marginal value as the test requirement. When the pressure inside the LOx or LCH<sub>4</sub> tanks is larger than the test requirement, the solenoid valves will open and release pressure until it returns back to the set pressure. As the flashing phenomenon is highly dependent on the injection boundary conditions, especially on the fluid superheat degree, a LN<sub>2</sub> bath is built on top of the chamber as a heat exchanger. The injector and the solenoid shut-off valve are immersed inside the LN<sub>2</sub> bath thus to almost maintain a constant injection temperature during the test. The LN<sub>2</sub> bath pressure is also closed-loop controlled (MV-LM4, P\_RV3), and is automatically filled by a large LN<sub>2</sub> tank (using the methane liquefaction tank). With a preset control sequence, the cryogenic fluid is injected into a vacuum chamber (the low pressure conditions are generated by a vacuum system), and the temperature and pressure measurement probes (e.g. T0~T7 and P0~P2) and the optical instruments are then triggered to start recording the test data.

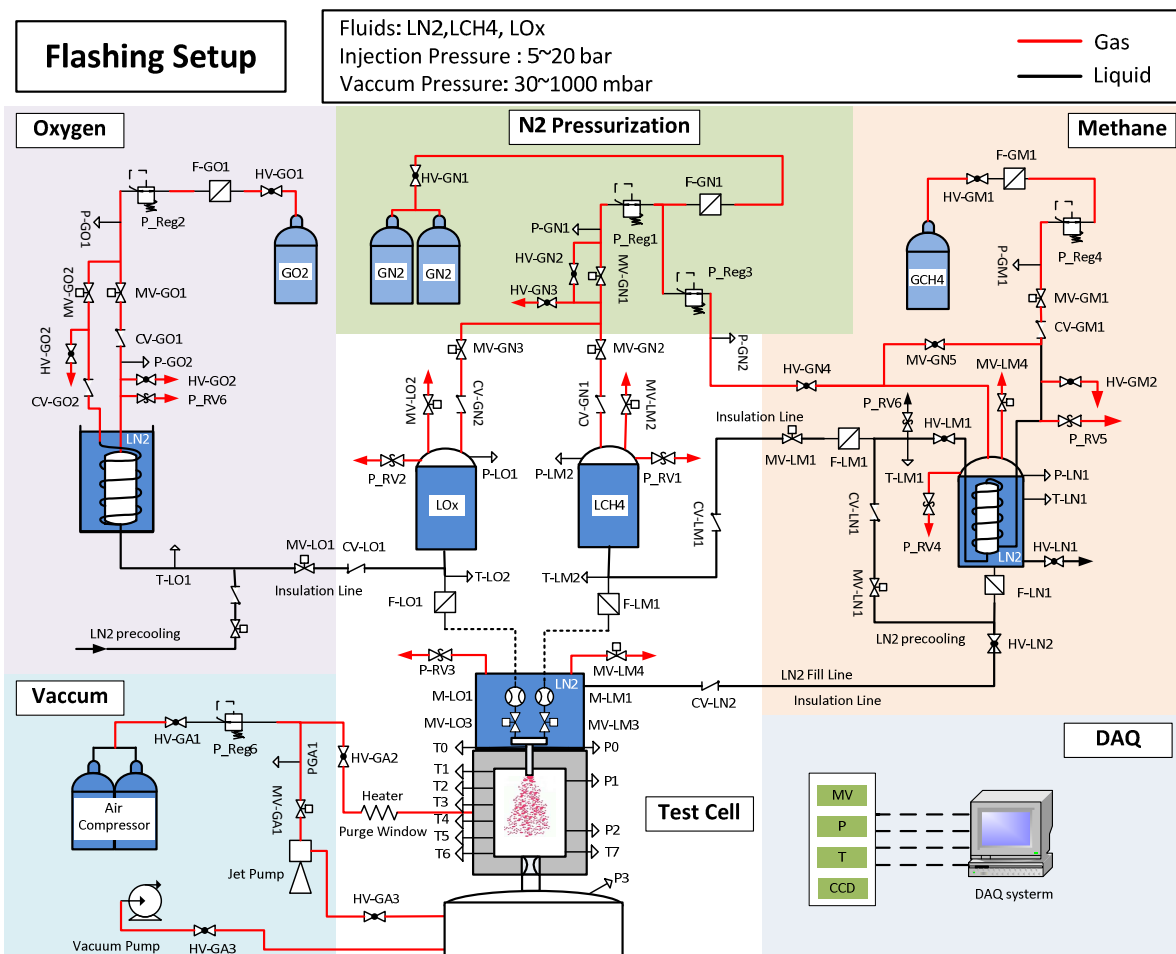


Fig. 3.1 Schematic of the flashing test setup

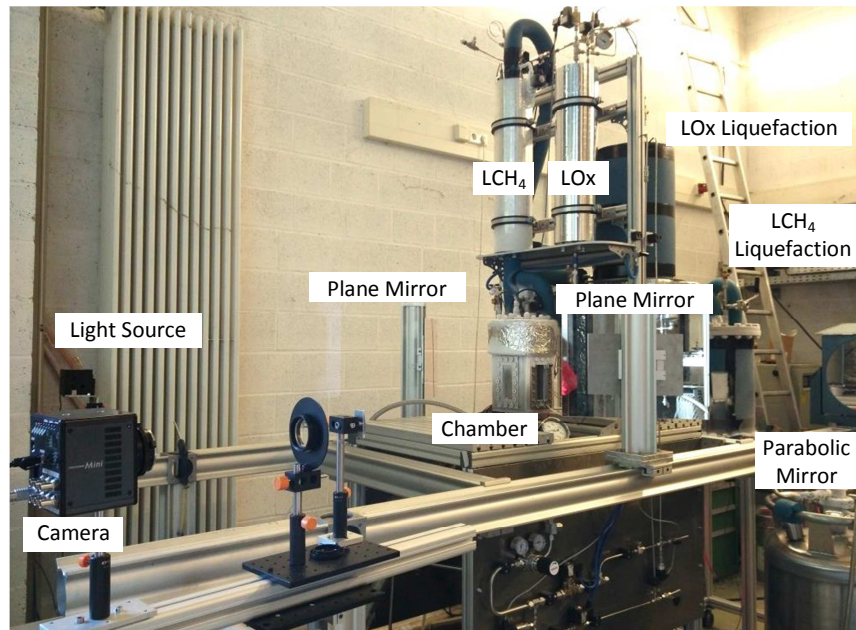


Fig. 3.2 Flashing test setup

### 3.2.1.2 Chamber with Optical Access

The rectangular test chamber is designed with 4 windows to allow visualization and optical analysis (one side is covered to set the thermal and pressure probes instruments), as shown in Fig. 3.3. The chamber size is 160 mm×144 mm×110 mm and the window is 152 mm×75 mm×15.5 mm.

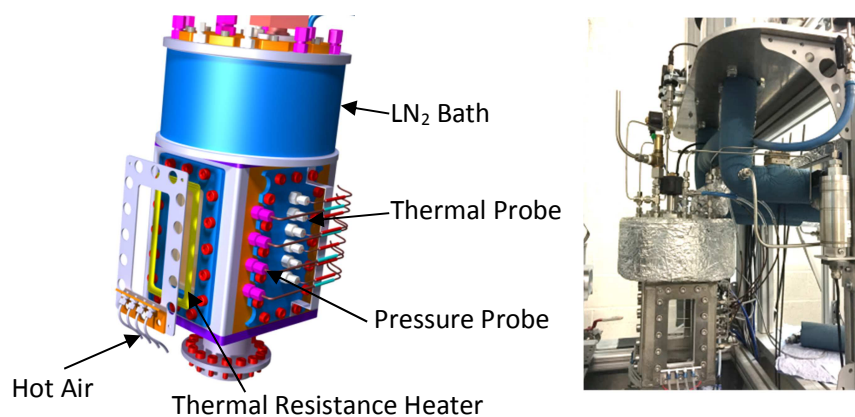


Fig. 3.3 Test chamber

A single element jet injector is used for the present study. The injector head is changeable to accommodate various diameters and lengths, as shown in Fig. 3.4. The temperature and pressure sensors

### 3. Experimental Investigation of Cryogenic Flashing Spray

are located close to the injection head to enable the measurement data to approximate the “injection temperature” and “injection pressure”.

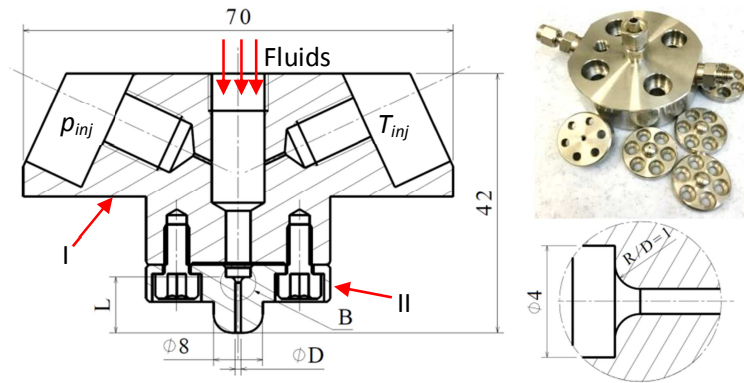


Fig. 3.4 Test jet injectors

Due to the low-temperature spray inside the chamber, the moisture molecules around the chamber are prone to condensate on the windows during the test, which will cause the challenges to the optical visualization. Flexible resistance heaters (polyimide film insulated) are, therefore, set between the chamber wall and the window covers to warm the chamber wall, and at the same time, the heated air (or heated nitrogen gas) is continuously purging the window, to prevent the moisture condensation on the chamber window.

#### 3.2.1.3 Liquefaction System

The investigated liquid propellants, i.e. LOx and LCH<sub>4</sub>, are produced by the simplified liquefaction systems with LN<sub>2</sub> as the coolant, schematically shown in Fig. 3.1. To liquify oxygen, the high pressurized oxygen gas (~30Mpa) is filtered and reduced to about 2Mpa. The depressurized oxygen gas is then separated by two feeding lines, one of which is a supplement to the liquefaction gas source and the other is to pressurize the liquefied oxygen. Since the triple point temperature of oxygen (56.4K @ 1.0atm) is lower than the saturation temperature of LN<sub>2</sub> (77.24K @ 1.0atm), the oxygen gas directly goes through an enclosed LN<sub>2</sub> tank with the pipe coils, which works as a heat exchanger. The safety valves, check valves and solenoid valves at this stage are used for pressure control and overpressure safety purpose. All the oxygen feeding lines are special cleaned (degreased) since oxygen is combustion-assisted.

The methane liquefaction is a bit more complex than oxygen. Safety is concerned since its flammability. Besides, the saturation temperature of LN<sub>2</sub> closely approximates to the triple point temperature of methane (90.68K @ 1.0atm). It indicates that a direct liquefaction of methane with saturated LN<sub>2</sub> at ambient pressure is impossible. Therefore, LN<sub>2</sub> is pressurized to increase its saturation temperature above the triple point temperature of methane, before it is used as a coolant. During the test, LN<sub>2</sub> is pressurized by nitrogen gas to about 6bar with a temperature of about 95K, thus the subcooled LCH<sub>4</sub> can be produced.

#### 3.2.1.4 Gas Pressurization and Cryogenic Feeding System

In the test, the high pressure nitrogen gas is used to pressurize the LCH<sub>4</sub> storage tank, the LOx storage tank and also to purge the system. For the cryogenic feeding system, the storage tanks of the liquid fluids are vacuum insulated, whereas the liquid feeding lines are insulated by Armaflex-LTD due to their flexibility. The detailed schematic is illustrated in Fig. 3.1.

#### 3.2.1.5 Vacuum System

The vacuum tank and chamber in the test are evacuated by a jet pump and a vacuum pump, with the layout shown in Fig. 3.1. The jet pump is designed with a vacuum capacity of about 100mbar, which is driven by compressive air of 10bar. The vacuum pump (vacuum capacity of 5mbar) is used for system drying to reduce the moisture both inside the liquid tank and inside the feeding line, which may freeze during the test, resulting in blockage of the solenoid valve or other potential damages. The vacuum pump also provides the low pressure for some tests with an extremely high superheat level.

### 3.2.2 Optical Diagnosis Methodology

#### 3.2.2.1 High-speed Schlieren Setup

For an non-intrusive study of cryogenic sprays, the optical diagnostic techniques are employed in the test, like the high-speed Schlieren technique and Shadowgraph technique, and Rainbow Refractometry technique. The Schlieren technique is a powerful tool for spray visualization, and the detailed principle of this technique can be found in Ref. [81]. As an example, Fig. 3.5 shows the schematic layout of the “C” type Schlieren setup that was built for the flashing spray transition study in our test.

This system is mainly composed of 6 components: a light source with slit device, a parabolic mirror, a plane mirror, a knife edge, an optical lens, and a high-speed camera. The light source that works for the back illumination is a Light-Emitting Diode with a slit device in front. The slit device, as an important part for creating a homogeneously collimated beam of light [81], is positioned at the focus point of the first parabolic mirror ( $f_1=3\text{m}$ ). The first parabolic mirror collects the slit light illumination and collimates it to produce parallel rays in the test region. The convex lens ( $f_2=1.0\text{m}$ ) focuses the collimated light (from the second parabolic mirror) towards the camera objective lens (Tokina100mm f/2.8) before the light is finally focused on the high-speed camera (Photron FASTCAM Mini UX100). The camera can provide 1280×1024 pixels resolution to 4000FPS and reduced resolution operation to 800000FPS with 640×8 pixels resolution. A global shutter provides blur free imagery with a minimum shutter exposure time of 1 $\mu\text{s}$  with the CMOS of 10 $\mu\text{m}$  per pixel.

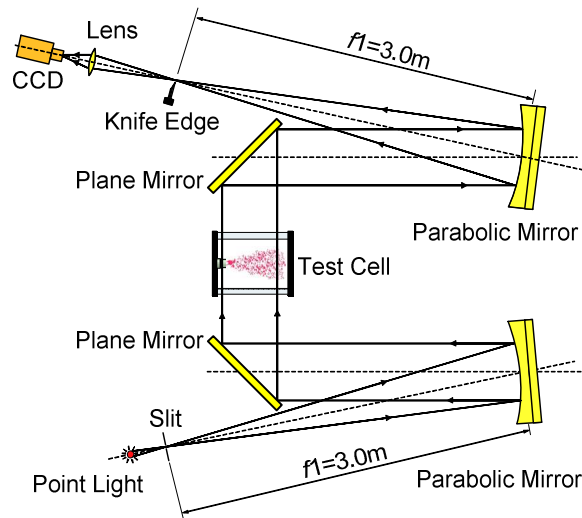


Fig. 3.5 Schematic of Schlieren setup

### 3.2.2.2 Global Rainbow Setup

The literature surveys show that a quantitative measurement of the cryogenic spray is rare, even for the widely developed laser-based techniques, such as PDPA and LIF. In order to perform quantitative study of the cryogenic spray droplets, a global rainbow refractometry setup was built and the corresponding tests were conducted. The detailed information of the test setup will be described in Chapter 4.

### 3.2.3 Measurement and Uncertainty

All that any experimental procedure can do is to give a value of the result that may be near the true value. We can never say that we know the true result, only that we have a result that may lie within a range of uncertainty. This section talks about the measurements and the corresponding uncertainty. Fig. 3.6 illustrates the potential sources of the measurement error.

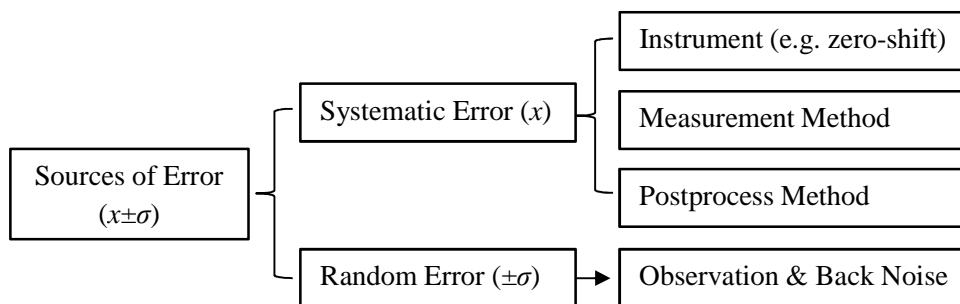


Fig. 3.6 Error of the measurement

### 3.2.3.1 Temperature Measurement and Uncertainty

As mentioned before, the quantitative investigation of thermal characteristics of the cryogenic flashing sprays with non-intrusive techniques is challenging. At present, therefore, the intrusive method is employed in the flashing study, thus to obtain precise results. Plenty of methods are available for the cryogenic temperature measurement, such as the widely used thermocouples (type T, E and K), the resistance thermometers (platinum resistance, carbon resistance, germanium resistance), capacitance thermometers (glass-ceramic), resonance thermometers and also vapor pressure method, which is based on the correlations between the saturation temperature and pressure of fluids. Due to the economy and small dimensions, the common thermocouple is used in the present study. It is known that thermocouple types T, E and K are applicable to LOx. Among them, type T thermocouple (copper-constantan) is the only one of the standardized types, for which limits of error below 273.15K have been established [82]. It is well recommended by the ASTM for use in the cryogenic temperature in vacuum or in oxidizing, reducing, or inert atmospheres [82].

In this study, therefore, type T thermocouples with the surface grounded junction and diameters of 0.5mm and 1.0mm are utilized. The uncertainty of the standard Type T thermocouple (ICE 584-3) is reported as  $\pm 1.0\text{K}$  or  $\pm 1.5\%$  of the measurement range. Before the test, the thermocouples are calibrated with LOx and LN<sub>2</sub> at the ambient pressure. Fig. 3.7 gives the average temperature measured by the thermocouples which are located in the spray. The measured data of each thermocouple is statistically averaged for several times measurement (the uncertainty for every thermocouple is estimated by Eq. (3.1), and it lies within a error margin of about  $\pm 1.0\text{K}$ ). This figure also indicates a small temperature fluctuation between the used thermocouples. With a statistical analysis with Eq. (3.1), the standard deviation is only of about  $\pm 0.25\text{K}$ . This confirms a good consistency of these thermocouples. The accuracy of the temperature measurement can be obtained by comparing the difference between the measured averaged temperature value and the reference temperature (from NIST data), shown as Eq. (3.2). The results show that this value is about  $3.0\text{K}$ . Therefore, in the present study, the temperature measurement error is estimated at a value of  $3.0 \pm 1.0\text{K}$ .

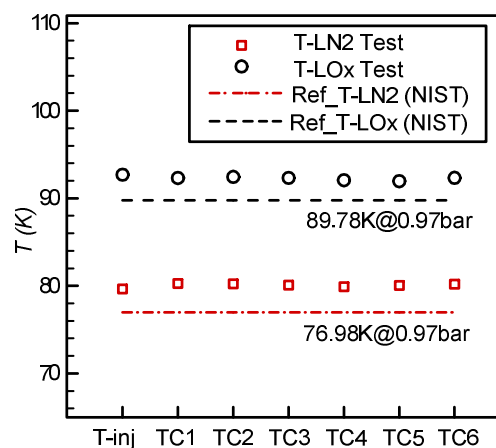


Fig. 3.7 Temperature measurement calibration

$$\sigma = \sqrt{\frac{1}{N-1} \sum_{i=1}^N (x_i - \bar{x})^2} \quad (3.1)$$

$$x = \bar{x} - x_{ref} = \frac{1}{N} \sum_{i=1}^N x_i - x_{ref} \quad (3.2)$$

#### 3.2.3.2 Pressure Measurement and Uncertainty

In this study, some pressure sensors with a current loop output (4~20mA) are utilized. This application benefits from the current loop's inherent immunity to the electrical noise and its independent to voltage drops in the system wiring, which leads to a higher accuracy of this specialization. Some pressure sensors with the voltage output (0~5V and 0~10V) are also instrumented. Since the voltage devices are sensitive to noise, the differential measurement model of the data acquisition device NI9205 (see Sec. 3.2.4) is configured to reject the commonmode noise. In addition, the pressure signals are transmitted by shielded wires, thus to minimize the noise pickup.

The pressure measurement systems are calibrated before the test. This calibration is done not only because of the sensor signal drifting itself but also due to the signal transport losses (voltage losses) in a long length cables for the voltage output sensors. Even for the current output sensors, the current input signals are transferred to the voltage signals by shunt resistors (precision metal film resistors, 500Ω) before being finally processed, which will also introduce measurement errors. Fig. 3.8 gives the designed analog signal input model.

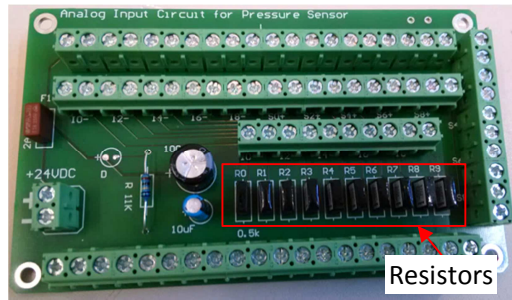


Fig. 3.8 Analog signal input model (for pressure sensors)

A comparison of the calibrated signals with the sensors' data shows a rather small deviation. Therefore, the pressure uncertainty here is estimated the same as the data provided by the sensor supplier for test data analysis, which is listed in Tab.3.1.

Tab.3.1 Detailed information of pressure sensors

NO.	Name	Type	Output	Accuracy (BFSL)	Comments
1	P_LM0	PMT-DS19	0~16bar, 0~5V	±0.5%	LCH <sub>4</sub> injection pressure (with pulse tube for low temperature protection)
	P_LN0				LN <sub>2</sub> injection pressure (with pulse tube for low temperature protection)
2	P_LO0	PMT-DS19	0~16bar, 0~5V	±0.5%	LOx injection pressure (with pulse tube for low temperature protection)
3	P_C1	WIKA-A10	0~1.0bar, 0~10V	±0.5%	chamber pressure
4	P_C2	WIKA S20	0~1.0bar 4~20mA	±0.25%	chamber pressure
5	P_LN1	WIKA S20	0~10bar, 0~10V	±0.25%	LN <sub>2</sub> pressure for methane liquefaction
6	P_LN2	WIKA S20	0~10bar, 0~10V	±0.25%	pressure in liquid nitrogen bath
7	P_GN1	WIKA-A10	0~50 bar, 0~10V	±0.5%	pressure in nitrogen gas delivery line
8	P_LO1	WIKA-S20	0~40bar, 4~20mA	±0.5%	pressure in oxygen liquefaction tank
9	P_LO2	WIKA S20	0~25bar, 4~20mA	±0.5%	pressure in LOx pressurized tank
10	P_GO1	WIKA-S20	0~40bar, 4~20mA	±0.5%	pressure in oxygen gas delivery line
11	P_GM1	WIKA-A10	0~50 bar, 0~10V	±0.5%	pressure in methane gas delivery line
12	P_LM1	WIKA A10	0~50bar, 0~10V	±0.5%	pressure in methane liquefaction tank
13	P_LM2	WIKA A10	0~25bar, 4~20mA	±0.5%	pressure in LCH <sub>4</sub> pressurized tank

### 3.2.3.3 Mass Flow Measurement and Uncertainty

In the early test, the mass flow rate was measured by the cryogenic turbine flow meter NT/FT4-8 with a capacity of 0.38~11L/min and repeatability of ±0.05%. Due to the disturbance to the flow, the flow meter was dismantled and the flow rate was measured by the calibrated injectors. It is well-known that the injector discharge coefficient is not only dependent on the injector geometry but also on the flow condition (e.g. turbulent or laminar flow). The latter is affected by the fluid property, such as the fluid viscosity, density, etc. It is possible to make an approximate conversion with different fluids to estimate the discharge coefficient, but a large error might be introduced. In this test, the discharge coefficient is obtained with LN<sub>2</sub> as the working fluid. In order to have a precise estimation of the mass flow rate, the uncertainty of the discharge coefficient is calculated with the Taylor series method of the uncertainty propagation, as shown in Eq. (3.3). The uncertainty of the volume flow can be obtained by the flow

### 3. Experimental Investigation of Cryogenic Flashing Spray

meter, which is  $\pm 0.05\%$ . The uncertainty of the pressure measurement is estimated at  $\pm 0.5\%$ . The injector is designed with the roughness of Ra3.2 for the injector inner hole surface. Therefore, the uncertainty of the injector area here is approximate  $\pm 1.3\%$ . The uncertainty of the fluid density can be approximately estimated with the temperature, which is about  $\pm 0.25\%$  (obtained by the density-temperature correlation of the NIST data). In sum, according to the above values, the uncertainty of discharge coefficient estimated by Eq. (3.5) is about  $\pm 1.4\%$ . The measured discharge coefficients corresponding to different injectors are shown in Fig. 3.9.

$$\Delta Y(X_1, X_2, \dots, X_N) = \sqrt{\sum_{i=1}^N \left( \frac{\partial Y}{\partial X_i} \Delta X_i \right)^2} \quad (3.3)$$

$$C_D = \frac{\dot{Q}}{A \sqrt{2 p_{diff} / \rho(T)}} \quad (3.4)$$

$$\frac{\Delta C_D}{C_D} = \sqrt{\left( \frac{\delta \dot{Q}}{\dot{Q}} \right)^2 + \left( \frac{1}{2} \frac{\Delta p_{diff}}{p_{diff}} \right)^2 + \left( \frac{1}{2} \frac{\Delta \rho}{\rho} \right)^2 + \left( \frac{\Delta A}{A} \right)^2} \quad (3.5)$$

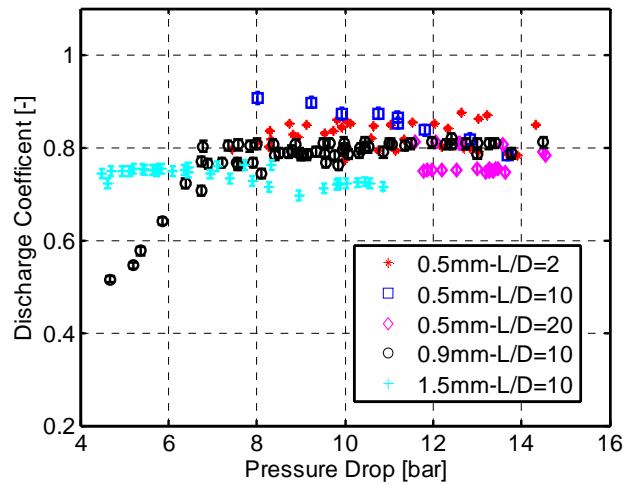


Fig. 3.9 Injector discharge coefficient with pressure drop

Based on the value of injector discharge coefficient, the mass flow rate is calculated, and the uncertainty can be estimated with the same process as the determination of uncertainty of discharge coefficient. The value is estimated at about 1.5%.

### 3.2.4 Data Acquisition

The data acquisition system, developed on a CompactRIO, mainly consists of three components: a real-time operating system (cRIO-9024), a reconfigurable FPGA (cRIO-9114) and some interchangeable I/O models. In the present study, three I/O models are used for data acquisition, i.e. NI-9214, NI-9205 and NI-9478 model.

The NI-9214 is used to acquire temperature signal with the sample rate greater than 68S/s. It offers 16 signal channels and is supported by several cold-junction compensations and an isothermal terminal block, which allows the measurement accuracy up to about 0.45K. The pressure signal is sampled by the NI-9205 model with a sample rate capacity of 250kS/s in total. This model can offer 32 single-end channels or 16 differential channels dependent on the connection method. As mentioned before, the differential channels connection is chosen in this study since it rejects the commonmode noise. The third model, NI-9478, which produces an output signal of 5V to 48V, is used to control the solenoid valves. It provides 16 channels with an update rate of 7 $\mu$ s. In the test, the pressure data-recording model is configured to achieve a high sample rate, which can reach up to 2000Hz. The temperature measurement model has a capacity of signal sample rate about 70Hz, which is set much lower than that of the pressure model due to the larger response time of thermocouples.

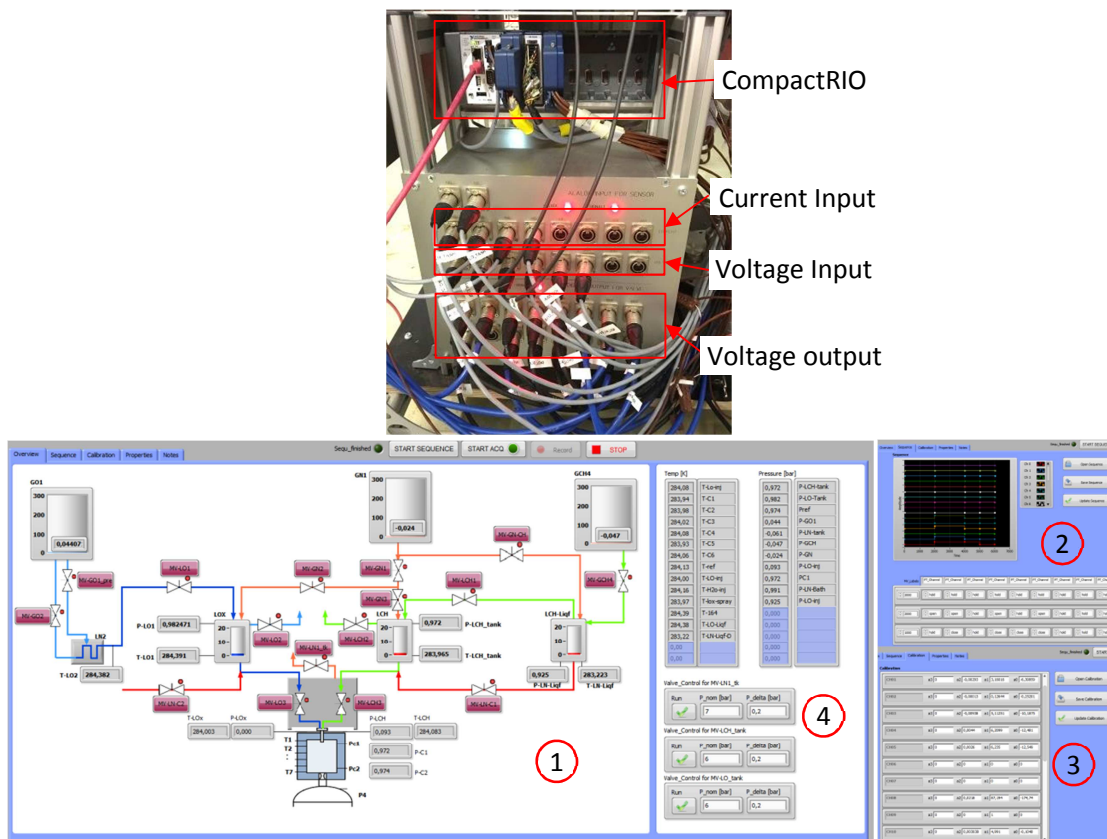


Fig. 3.10 DAQ hard ware and the graphical user interface

The DAQ hard ware and the corresponding user control panel (Graphical User Interface) is illustrated in Fig. 3.10. The user control panel mainly includes four parts: (1) the overview display module, (2) the sequence control module, (3) the data calibration module and (4) the input/output module.

## 3.3 Results and Analyses

In this section, we analyze the morphology of the flashing spray under various superheat conditions. The flashing transition criterion is explored based on the nucleation theory. The thermal characteristics of the sprays along the jet centerline as well as the spray lateral propagation will also be discussed in detail. Moreover, the solidification phase transition is also observed and will be analyzed.

### 3.3.1 Test Cases

Tab. 3.2 gives the geometric parameters of tested injectors. The single jet injectors with different orifice diameters ( $D$ ) and different length to diameter ratios ( $L/D$ ) are used. Tab. 3.3 lists general operation conditions of the test. During the test, due to the continuous injection and the spray evaporation, the chamber pressure increases slightly though the jet pump and/or vacuum pump is continuously working. The injection pressure  $p_{inj}$  and chamber pressure  $p_c$  are averaged during the test period.

Tab. 3.2 Parameters of injector geometry

Injector	#1	#2	#3	#4	#5
$D(\text{mm})$	0.5	0.5	0.5	0.9	1.5
$L/D$	2	10	20	10	10

Tab. 3.3 General operation conditions of flashing test

Parameter	Range	Uncertainty
$p_{inj}$	5bar~20bar	$\pm 0.5\%$
$T_{inj}$	80K~120K	$\pm 1.0\text{K}$
$p_c$	0.03bar~1.0bar	$\pm 0.25\%$

### 3.3.2 Flashing Spray Evolution

The flashing phenomenon is accompanied by superheat that makes the fluid metastable. Here, the  $\text{LN}_2$  flashing spray is taken as an example. During the test,  $\text{LN}_2$  experiences a transition from a subcooled state or near saturation state to a strong superheated state due to a rapid depressurization, before it finally returns to the equilibrium stable state by means of violent atomization and vaporization. Fig. 3.11 presents the nitrogen  $p$ - $T$  diagram. Initially, the subcooled  $\text{LN}_2$  stays at point A at high pressure;

suddenly it is released into a low pressure environment. During this process, the liquid in the stable equilibrium state is greatly superheated and becomes metastable (point B), which corresponds to a local minimum free energy. In this state, the system can be temporarily stable with small fluctuations of the thermodynamic variables. However, this state will not be long-time maintained due to pressure disturbance. It will overcome the energy barrier, and release the latent heat through violent atomization and vaporization (flashing), and finally return to the global minimum free energy, reaching a new equilibrium stable state (point C). If the backpressure is sufficiently low (i.e. below the triple point pressure), then when the subcooled LN<sub>2</sub> is injected into this environment (point B'), the liquid will be highly superheated. The dramatic pressure drop will therefore trigger much stronger flashing phenomena, and the release of huge latent heat might lead the metastable liquid solidification (point C').

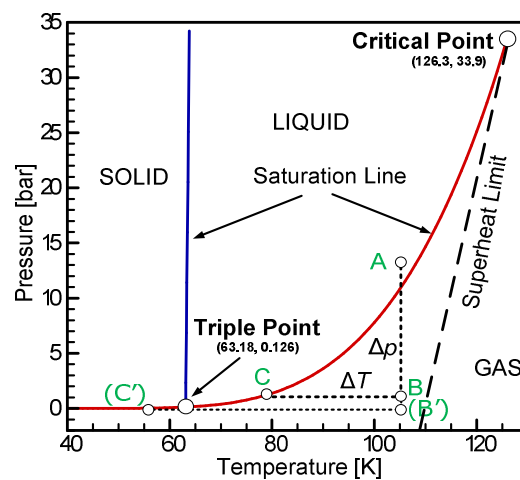


Fig. 3.11  $p$ - $T$  diagram of nitrogen

As aforementioned in Chapter 2, the superheat as a critical parameter for flashing can be described either by a temperature difference or pressure ratio. In this paper, the latter is adopted. Two reasons are presented for this choice: 1) the liquid's superheat in our work is obtained by depressurization rather than by injection temperature increase; 2) the phase transition of flashing phenomenon is driven by the chemical potential difference, and the pressure ratio is directly linked to the chemical potential difference  $\Delta\mu$ , as shown in Eq. (2.15).

Fig. 3.12 shows the spray evolution with increasing degrees of the superheat ( $R_p$ ) of injector #1. The thermocouples are marked as TC1 to TC6 (TC5 and TC6 could not be seen here) from the injector orifice to the downstream. In Fig. 3.12a and Fig. 3.12b, which occur under considerably low superheat conditions, the sprays display a similar characteristic. It presents as cylindrical jet, disintegrates into liquid ligaments and further shatters into smaller droplets downstream of the injector. These phenomena indicate that the sprays are strongly dominated by the mechanical atomization under these conditions. It can be explained as follows. During the test, the various superheat levels are mainly obtained by controlling the vacuum chamber pressure. Therefore, the low superheat conditions (small  $R_p$ ) indicates a high chamber pressure, which means there are more gases inside the chamber. Under this condition, the liquid jet is not only affected by the thermal effect (superheat), but also strongly affected by the initial turbulence of the fluid and its interaction with the surrounding gas (entrainment). Therefore, the cohesive and disruptive force

### 3. Experimental Investigation of Cryogenic Flashing Spray

acting on the jets surface, combined with the entrainment effect of the surrounding gas, causes the liquid jet to shatter into small liquid ligaments or to disintegrate further into smaller droplets.

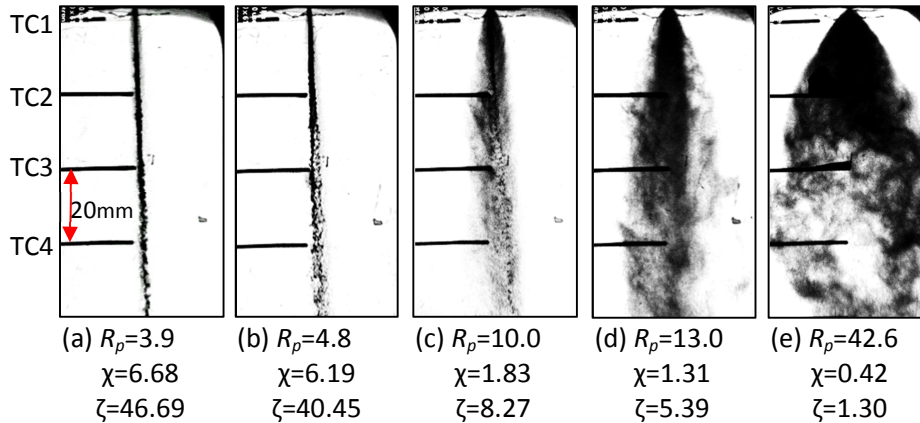


Fig. 3.12 LN<sub>2</sub> flashing spray under different superheat conditions (Injector #1)

The mechanisms of mechanical atomization have been intensively studied [83, 84, 85, 86]. Fig. 3.13 gives the jet breakup regimes' boundaries described by Ohnesorge [83] and Miesse [84]. The criterion of Messie's regime is based on the test of LN<sub>2</sub> and water discharged into the ambient air. In this figure, region (a) represents the Rayleigh Breakup Regime, where the drop diameter is larger than the jet diameter, and the jet disintegrates downstream of the injector. Region (b) is the First Wind-Induced Regime, where the drop size is about the order of the jet diameter. Region (c) shows the Second Wind-Induced Regime, in which the drops are smaller than the jet diameter and breakup occurs some distance downstream of the injector. Region (d) illustrates the Atomization Regime, where the drop size is much smaller than the jet diameter.

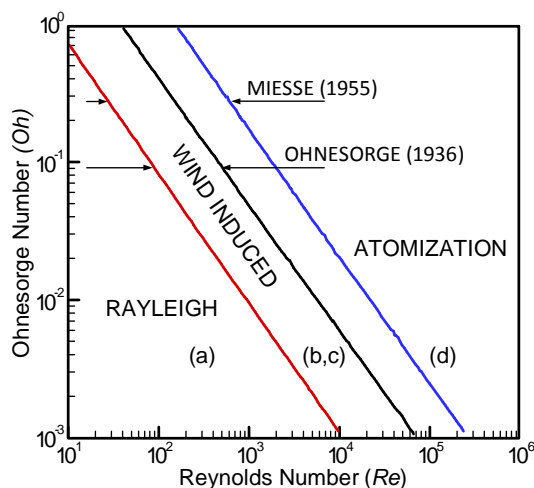


Fig. 3.13 Jet breakup regimes description by Ohnesorge and Miesse [83, 84]

In the cases presented in Fig. 3.12a and Fig. 3.12b, the Reynolds number based on the injector diameter is estimated at about  $1.22 \times 10^5$  and  $1.26 \times 10^5$ , and the respective Ohnesorge number approximates  $2.30 \times 10^{-3}$  and  $2.26 \times 10^{-3}$ . These values are located within the “Atomization Regime” region, which indicates that the spray is primarily dominated by the mechanical atomization.

With the superheat level increasing, the spray jet disintegrates into finer droplets with a fiercer lateral propagation and shorter intact liquid core, as shown in Fig. 3.12c and Fig. 3.12d. In these cases, from the view of the nucleation theory, the internal energy of the liquid cluster is comparable to the nucleation barrier and the jet spray is greatly unstable. With pressure disturbances, parts of the liquid clusters are likely to overcome the nucleation barrier, enhancing the massive bubble nuclei to grow up and the liquid jets break up to and disintegrate into small droplets until the jet reaches a new stable equilibrium state, giving the spray a strong lateral propagation.

By further increasing the superheat level (still below the superheat limit,  $T_{lim} \sim 0.9T_{cri}$  [87, 88, 89]), most of the nucleation clusters can overcome the nucleation barrier, under which the probability of bubble nuclei formation increases exponentially, triggering a large scale violent atomization and vaporization, as seen in Fig. 3.12e. This happens almost right at the injector orifice, showing a large bell-shaped spray angle and finer droplets downstream of the injector, all of which characterizes a fully flashing spray.

Polanco et al. [90] pointed out that the lower limit superheat for the heterogeneous nucleation occurrence is about  $T_{inj}/T_{cri} < 0.63$ , while the homogeneous nucleation takes place at about  $T_{inj}/T_{cri} > 0.9$  (exceeds the superheat limit). In the present work, the test conditions fall in the scope of  $0.63 < T_{inj}/T_{cri} < 0.9$ . Therefore, the flashing sprays in these tests are mainly caused by the heterogeneous nucleation rather than the homogeneous nucleation.

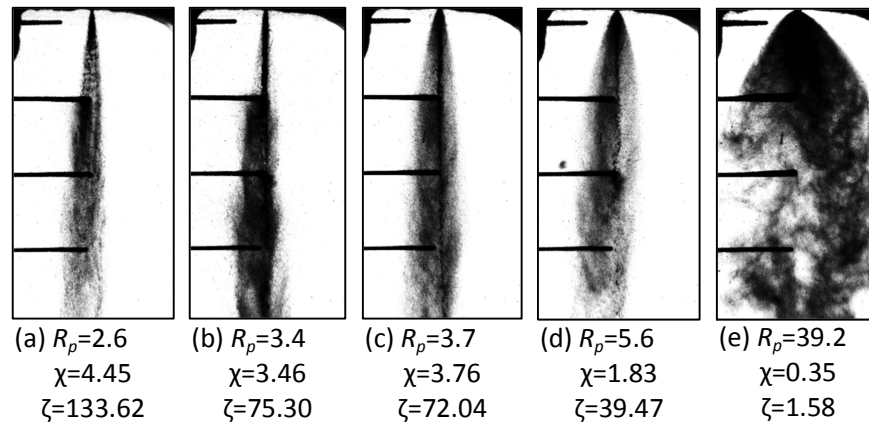


Fig. 3.14 LN<sub>2</sub> flashing spray under different superheat conditions (Injector #2)

Fig. 3.14 gives the spray evolution of injector #2 at different superheat levels. The mechanical atomization regime is clearly shown. Under low superheat conditions, a liquid core in the spray center can be seen clearly with the shattered spray around. The liquid core decreases as the superheat increases.

### 3. Experimental Investigation of Cryogenic Flashing Spray

Under the high superheat conditions, no ligments are clearly present, and the whole spray reveals fully flashing features (see Fig. 3.14e).

In summary, under low superheat conditions, the mechanical atomization dominates the liquid jet atomization. With increasing the degree of superheat, the heterogeneous nucleation starts to contribute to the jet atomization until it finally dominates the process. Consequently, as the superheat level increases, the spray experiences a complete process from the mechanical atomization to the flashing transition regime before it finally reaches the fully flashing regime.

The transient evolution of the fully flashing spray is captured with a high-speed Schlieren technique. The Schlieren technique is, in principle, sensitive to the first space derivative of the refractive index gradient (fluid density gradient). The instantaneous Schlieren images are shown in Fig. 3.15. The normalized light intensity ( $\Delta I/I$ ) profiles along the spray centerline are also plotted.  $I$  is the raw image intensity and  $\Delta I$  is the relative change with respect to the background image intensity. These profiles are averaged over 15 adjacent pixel rows below the spray centerline (see the rectangular region in the image of  $t=0\text{ms}$ ) to limit the effect of back noise. This region below the spray centerline is selected to avoid the thermocouple effect on the analysis of the light intensity.

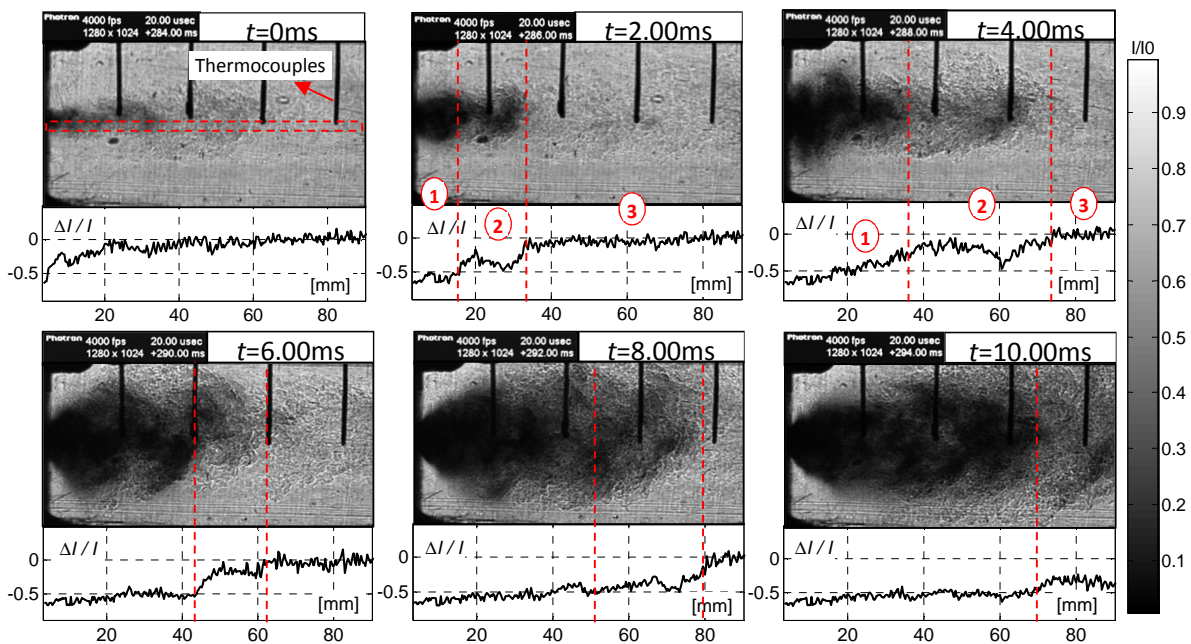


Fig. 3.15 Flashing spray transient process

At the injection beginning (i.e.  $t=0\text{ms}$ ), the image presents a rather weak intensity feature. Near the injector orifice, the relative intensities are below 0, and after a short distance, these values approach around 0. The negative intensity implies a disturbance of the fluid. The zero intensity means the low pressure gas in the chamber are still not affected by the injected spray. After a short time period, at  $t=2.00\text{ms}$ , the image shows three distinct regions, i.e. a dark region near the injector orifice, a high turbulence region and a rather weak intensity region downstream. These three regions can also be

indicated by the intensity profiles, which are respectively marked as 1, 2 and 3. In specific, region 1 gives much smaller negative intensity, which corresponds to the liquid spray with high density. Then, the relative intensity has a drastic increase from at about -0.5 to near 0 at approximate 30mm downstream of the injector (see region 2). This region displays highly turbulent structures, which is supposed to be the results of interaction between the evaporated vapor and the surrounding ambient gas. At region 3, the relative intensities are near 0 since the main evaporated gas does not reach to this region. The more distinct turbulence region can be found in the image at  $t=4.00\text{ms}$ . After about 10.00ms, the relative intensities along the spray centerline has much small negative values, and the spray inside the chamber shows strong flash atomization and vaporization with a bell-shaped profile.

### 3.3.3 Effect of Injector Geometry on Flashing Spray

The objective of this section is to assess the impact of injector geometry on the cryogenic superheated spray jet. Two main parameters, i.e. injector aspect ratio ( $L/D$ ) and injector orifice diameter ( $D$ ), are chosen to perform the study. The injectors of various specifications can be found in Tab. 3.2.

#### 3.3.3.1 Effect of Injector Aspect Ratio on Flashing Spray

The injector aspect ratio ( $L/D$ ) exerts a direct influence on the spray, since it affects the fluid instability and the pressure drop, which offers the flow inlet boundary conditions to the downstream situation (e.g. the flow inside the combustion chamber). This effect is more serious for the superheated flow, since the nucleation process is highly sensitive to the residence time and the condition of the wall contact. In this section, the injectors of 0.5mm inner diameter with different injector aspect ratios ( $L/D= 2$  and 20) are taken as an example to explore the effect of injector aspect ratio on the flashing phenomenon. Fig. 3.16 exhibits the spray patterns in different test cases. The specific test operation conditions are listed in Tab. 3.4.

Tab. 3.4 Boundary conditions of Fig. 3.16

Injector #1 ( $D=0.5\text{mm}$ & $L/D=2$ )				Injector #3 ( $D=0.5\text{mm}$ & $L/D=20$ )			
$T_{inj}$ (K)	$p_{inj}$ (bar)	$p_c$ (bar)	$R_p$	$T_{inj}$ (K)	$p_{inj}$ (bar)	$p_c$ (bar)	$R_p$
92	9.8	0.10	42.6	93	9.9	0.10	46.2
88	9.8	0.30	10.0	88	10.2	0.29	10.0
85	9.8	0.51	4.8	89	9.9	0.68	4.9
86	9.8	0.64	3.9	90	9.8	0.97	3.7

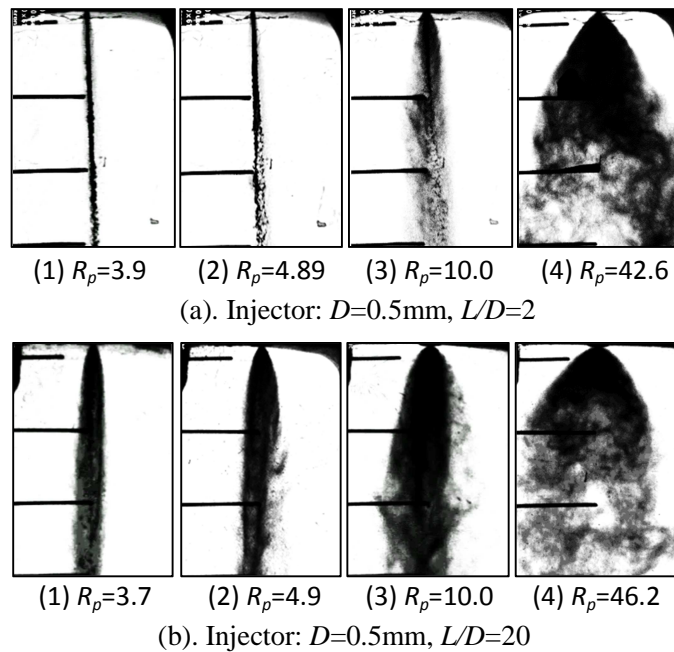


Fig. 3.16 Cryogenic sprays with different injector aspect ratios

In Fig. 3.16, the graphs strongly demonstrate the substantial influence of the injector length-to-diameter ratio ( $L/D$ ) on the flashing spray, and with a large  $L/D$ , the flashing spray is more violent. See Fig. 3.16a (2) and Fig. 3.16b (2), in which the spray jets are at a similar superheat level. Fig. 3.16a (2) shows a long intact liquid jet and then the spray breaks into large liquid ligaments downstream of the injector, and no distinct droplets are present. However, in Fig. 3.16b (2), after the spray emerges from the longer injector ( $L/D=20$ ), the jet starts to disintegrate right near the injector orifice and becomes atomized downstream from the ligaments into smaller droplets. The injector aspect ratio contributes much on the spray behavior under such conditions. The difference in spray behaviors due to the injector geometry is even more noticeable in Fig. 3.16a (3) and Fig. 3.16b (3), where the thermal effect starts to outweigh the spray atomization. In the fully flashing regime, described in Fig. 3.16a (4) and Fig. 3.16b (4), the liquid jets display similar spray features, with both sprays producing a huge bell-shaped spray angle and becoming exquisitely atomized. In sum, the spray jets in Fig. 3.16b show a stronger lateral propagation in comparison with the images in Fig. 3.16a, which demonstrates that a much more violent flashing occurs when a longer injector is employed.

The Classical Nucleation Theory (CNT) might provide some insight into the effects of the injector geometry on the flashing phenomenon. According to the CNT, the bubble nucleus will be formed and grow up until the internal energy of the molecule cluster overcomes the nucleation barrier and the bubble nucleus size becomes larger than the critical nucleation size. Practically, with the same diameter, longer injectors possess more manufacturing flaws than the shorter one, e. g. machine-formed pits and scratches. These manufacturing flaws provide more heterogeneous nucleation sites. This makes the long injectors inclined to generate more bubble nucleation and trigger more violent nucleate boiling, resulting in an

more exquisite atomization. This is true even under low superheat conditions (e.g. see the jet atomization in Fig. 3.16b(2)). The heterogeneous energy barrier is low, indicating that the required superheat to generate the heterogeneous nucleation is less compared with the homogeneous nucleation. Therefore, the bubble nucleation can be formed as heterogeneous nucleation under low superheat conditions, leading to a strong atomization. Moreover, the inception of nucleate boiling is not only determined by the liquid superheat level, but also by the bubble evolution time [91]. Longer injectors allow the liquid jet longer residence time inside the injector, which provides more time for the initial nucleus to grow up to reach the critical bubble nucleus. This facilitates heterogeneous nucleation and enhances the spray atomization.

The spray angles are also analyzed in this section. The original shadowgraph images are binarized to detect the edge profiles of the sprays, from which the spray angles at different axial positions are estimated. The definition of the spray angle is shown in Fig. 3.17. At the specific axial position, the upper and lower branches of the spray profiles are used to calculate the corresponding half spray angles  $\alpha$  and  $\beta$ . The total local spray angle  $\theta$  is defined as

$$\theta(z) = \alpha(z) + \beta(z) = \arctan(y_u - y_0)/(z - z_0) + \arctan(y_l - y_0)/(z - z_0) \quad (3.6)$$

where  $z_0$  and  $y_0$  are the positions of the injector orifice,  $y_u$  and  $y_l$  are y-coordinates of corresponding upper and lower spray profiles.

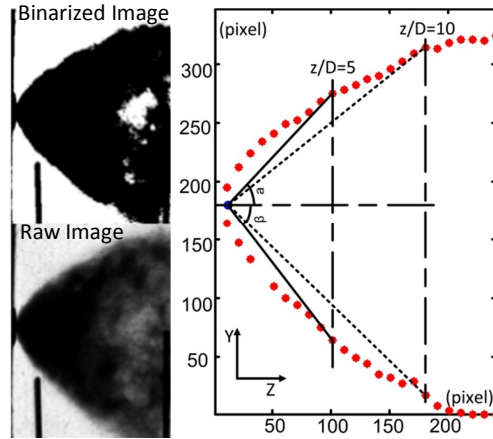


Fig. 3.17 Definition of the spray angle

Fig. 3.18 shows the estimated spray angles at various superheat degrees with different injector lengths. The figure shows that as the superheat increases, the spray angle increases. For example, under low superheat degrees of injector #1 ( $L/D=2$ ), at  $\ln(R_p) \sim 1.5$  the spray has a small open angle of just about  $30^\circ$  (measured at  $z/D=5$ ), while this angle is almost tripled and increases to about  $90^\circ$  at high superheat level with  $\ln(R_p) \sim 3.8$ . The figure demonstrates that the longer injector produces a larger spray angle than that of the shorter ones under the same superheat conditions. For example, at  $\ln(R_p) \sim 3.8$  and  $z/D=5$ , the spray angle is about  $140^\circ$  with the longer injector ( $L/D=20$ ), while the angle is only about  $90^\circ$  with the shorter one ( $L/D=2$ ) at the same superheat level.

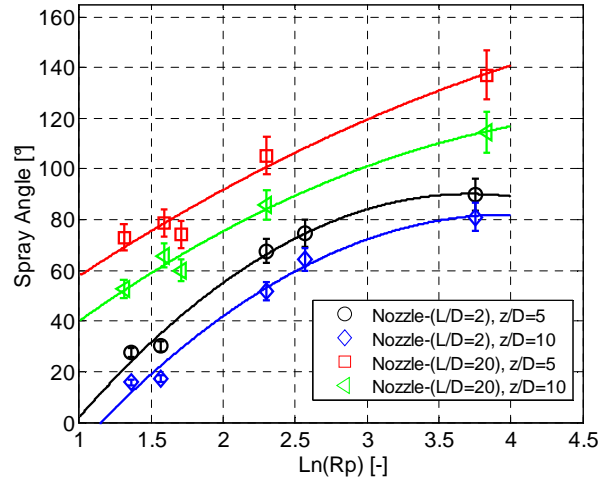


Fig. 3.18 Spray angles at various superheat degrees with different injector aspect ratios

In summary, under the same superheat conditions ( $R_p$ ), the injector with a larger aspect ratio facilitates the flashing atomization and evaporation.

### 3.3.3.2 Effect of Injector Diameter on Flashing Spray

In this section, the effect of the injector diameter on the flashing will be discussed. The test boundary conditions are listed in Tab. 3.5, and the corresponding spray images are shown in Fig. 3.19.

Tab. 3.5 Boundary conditions in Fig. 3.19

Injector #4 ( $L/D=10$ & $D=0.9\text{mm}$ )				Injector #5 ( $L/D=10$ & $D=1.5\text{mm}$ )			
$T_{inj}$ (K)	$p_{inj}$ (bar)	$p_c$ (bar)	$R_p$	$T_{inj}$ (K)	$p_{inj}$ (bar)	$p_c$ (bar)	$R_p$
96	7.9	0.12	48.6	98	7.8	0.13	52.0
96	8.0	0.48	12.1	97	6.5	0.38	13.2
97	8.0	0.70	9.0	98	7.6	0.71	9.5
97	7.4	0.97	6.5	97	7.0	0.97	6.5

The graphs show that under similar test boundary conditions, such as the same superheat level and same  $L/D$ , the liquid jet released from larger orifice injectors triggers flashing with more ease and presents a more violent atomization than the smaller ones. By releasing the superheated water into a low pressure chamber, Peter [36] also pointed out that the cylindrical injector with a larger diameter is more easily to trigger strong flash atomization than the ones with smaller diameter. Here, take the images of Fig. 3.19a (2) and Fig. 3.19b (2) as an example, which are at the similar superheat level of  $R_p \sim 9$ . The injector #4 ( $D=0.9\text{mm}$ ) under this condition displays a cylindrical-like spray shape with a small spray angle, while with injector #5 ( $D=1.5\text{mm}$ ) a much larger spray angle are shown, indicating a stronger atomization in this situation. This positive relationship between the injector diameter and the flash atomization can also find its explanation in the nucleation theory. Under similar boundary conditions (i.e. same  $L/D$  and same  $R_p$ ), a larger injector diameter means a larger contact surface of the liquid jet with the injector wall. The

larger wall surface offers more irregular sites and increases the population of the heterogeneous nucleation sites, leading to more bubble nuclei generation. When the jet is released into the vacuum chamber, these bubbles grow up and break up the liquid jets, resulting in a violent flashing spray.

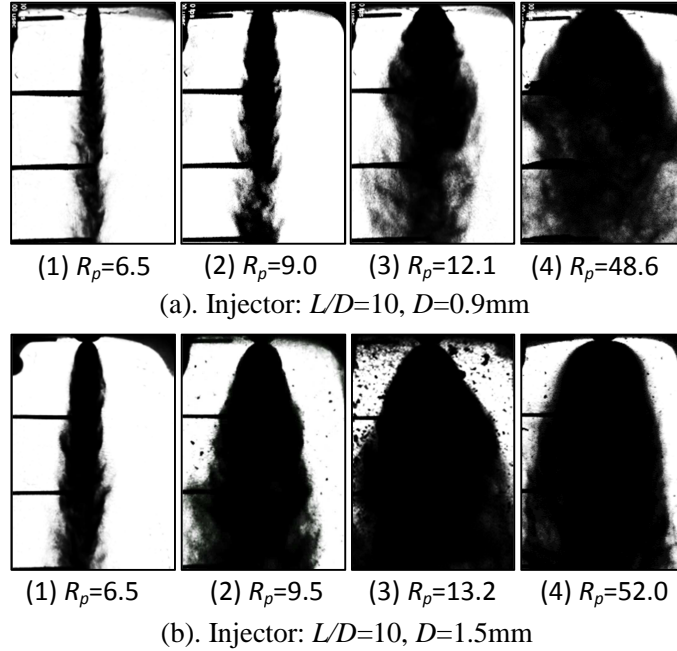


Fig. 3.19 Cryogenic sprays with different injector diameters

Fig. 3.20 illustrates the spray angles at various superheat levels with different injector diameters. It shows that under the same boundary condition, an increase in the orifice diameter gives rise to the elevated spray angle. For the large injector with  $L/D=10$  and  $D=1.5\text{mm}$ , with the superheat degrees  $\ln(R_p)$  increase from about 1.9 to approximate 4.0, the spray angles at  $z/D=5$  almost increase by twice, from about  $55^\circ$  to about  $123^\circ$ . For the smaller one with  $D=0.9\text{mm}$ , the corresponding spray angles are increasing from about  $50^\circ$  to about  $120^\circ$ , which are rather close to the spray angles of the larger injector. This demonstrates that the injector diameter shows a positive effect on the flash atomization, but this effect is not as significant as the injector aspect ratio does (see Fig. 3.18). These different effects will be explained as follows.

The nucleation rate has been well defined by the classical nucleation theory, as shown Eq. (2.26) in Chapter 2. Here, we focus on the potential factors related to the injector geometry that may affect the nucleation rate. Since the flashing sprays are mainly caused by the heterogeneous nucleation in the present test cases, the contact surface between the liquid and the injector will be an important factor to the bubble nucleation. Therefore, injector inner surface area  $A_s$  should be mainly taken into account for the nucleation rate estimation. In addition, the number density of the molecules which can contact the injector wall directly affects the nucleation rate, and it should also be considered. As mentioned before, the residence time  $\tau$  inside the injector is significant to the bubble nucleation, therefore,  $\tau$  is also considered as a main factor to the nucleation rate. Therefore, considering the above factors, the corrected nucleation rate  $J_{cor}$  can be defined by

### 3. Experimental Investigation of Cryogenic Flashing Spray

$$J_{cor} \sim P_{nucl} [A_s, V, \tau, \dots] J \quad (3.7)$$

where  $P_{nucl}$  is the probability of the heterogeneous nucleation caused by the injector geometry. It is obviously that a larger area of the nozzle surface, a longer residence time will cause a larger probability of the nucleation. A large injector diameter will decrease the number ratio between the molecules which can contact the injector wall ( $\propto LD$ ) to the total molecules inside the injector ( $\propto LD^2$ ). This will decrease the probability of the nucleation. Therefore  $P_{nucl}$  can be expressed by

$$P_{nucl} \propto \frac{\tau A_s}{V} \propto \left( \frac{L}{u} \frac{DL}{D^2 L} \right) = \left( \frac{L}{D} \right) \frac{1}{u} \quad (3.8)$$

where  $u$  is the injection velocity and  $V$  is the volume of the injector inner hole.

The test cases of Fig. 3.20 are in the similar pressure drop conditions, thus in the similar injection velocity conditions, therefore, the corrected nucleation rate is proportional to the injector aspect ratio, and is independent on the injector diameter itself. This might be the reason that the impact of the injector aspect ratio on the flashing spray in these test cases is much stronger than the injector diameter does.

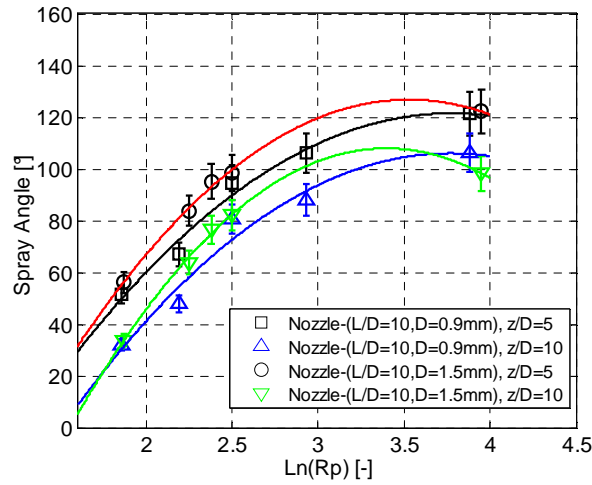


Fig. 3.20 Spray angles at various superheat degrees with different injector diameters

In summary, the test results show that under the same superheat conditions ( $R_p$ ), the large diameter injector shows a positive but small effect on the flashing atomization and evaporation process.

#### 3.3.4 Thermal Characteristics of Flashing Spray

This section concentrates on the thermal characteristics of the flashing jet. The temperature evolution along the spray centerline will be discussed. Inside the chamber, the first thermal probe (TC1) is set

outside of the jet spray to detect the near-injector surrounding temperature. The thermocouple (TC7) is instrumented far away from the spray to detect the ambient temperature inside the chamber. The spray thermal behavior is recorded by the thermocouples TC2 to TC6, of which TC2 is located 23mm below the injector orifice, and the others (TC3, TC4, TC5 and TC6) are positioned following TC2 with a distance of 20mm in between. The installation locations can be found in Fig. 3.3 and Fig. 3.12.

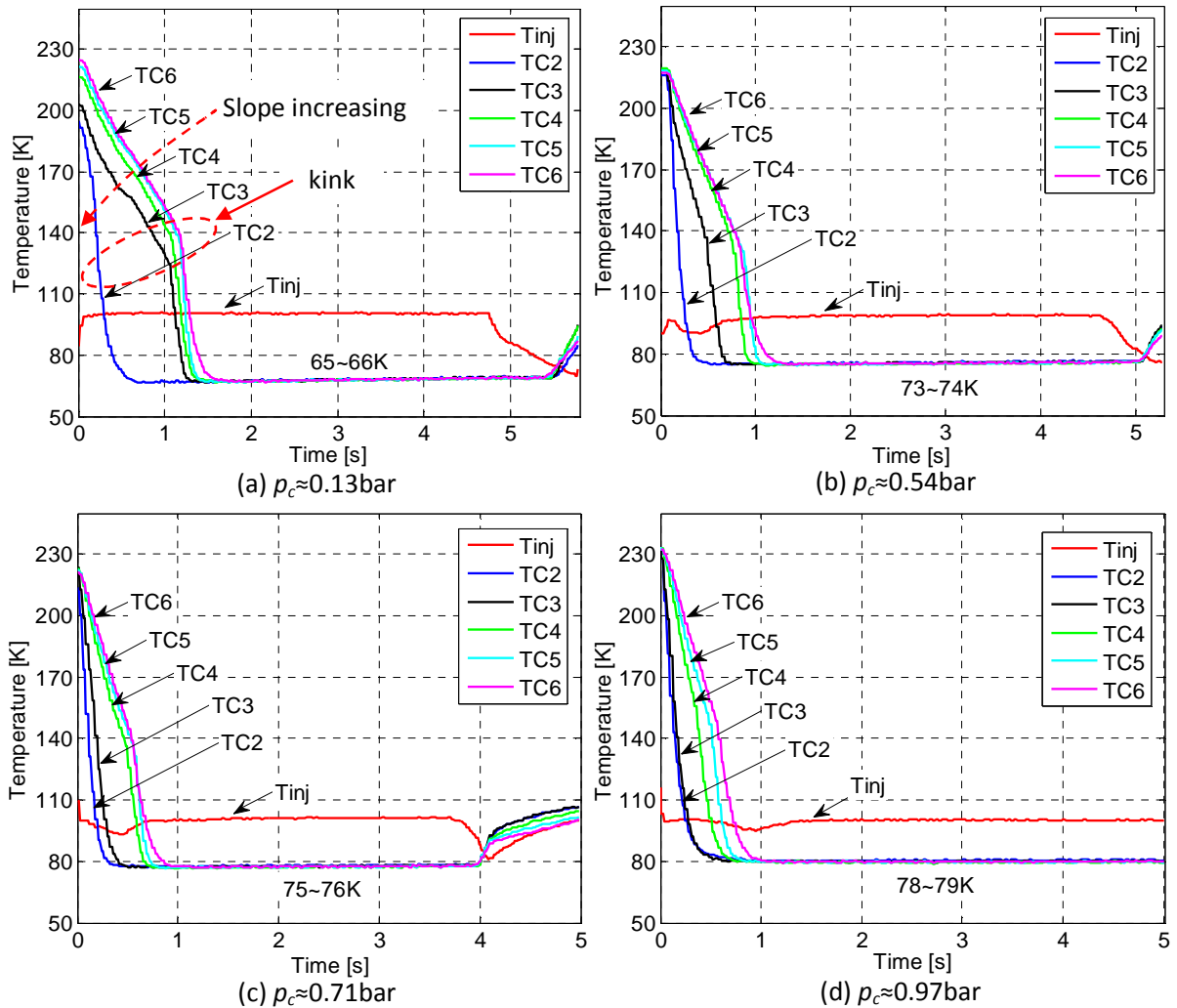


Fig. 3.21 Temperature evolution along  $\text{LN}_2$  spray centerline ( Injector #5)

Fig. 3.21(a-d) describe the temperature evolution along the spray centerline at different chamber pressures with injector #5. The figures illustrate that the temperature evolution profiles  $T(t)$  show self-similarity at different detection positions. Some kink points of the temperature curves can be found in the figure (see the dashed region in Fig. 3.21a). The profiles show a temperature decrease before the kink points, followed by a drastic drop before leveling off at stable values until the main injection valve shuts off. To elaborate, at start, the temperatures both inside the chamber and inside the injector are low (220K~230K) as a result of the chill-down process prior to the spray injection. As the main injection valve opens, the injected spray gets subcooled and the corresponding injection temperature ( $T_{inj}$ ) falls

### 3. Experimental Investigation of Cryogenic Flashing Spray

---

below the fluid's initial temperature due to a heat exchange between the fluid and the LN<sub>2</sub> bath (see Fig. 3.11). The subcooled injection, to some extent, can minimize the occurrence possibility of the two-phase flow inside the injector, and therefore reduces its impact on the external flashing inside the chamber. When the liquid jet passes the injector, the heterogeneous and even homogeneous nuclei grow up, and then break up the liquid jet, and burst into the vacuum chamber, triggering a violent flashing atomization and vaporization, leading to a temperature drop.

The temperature distribution  $T(z)$  along the spray centerline can also be implied by Fig. 3.21. The figure shows that before the kink points, the slopes of the temperature curves (from TC2 to TC6) decrease, and the slope of TC2 curve is much larger than that of other curves. After the kink points, the curves show similar slope values. This implies that the temperature distributions along the spray centerline present a steep temperature drop followed by a gradual trend in the beginning of injection, and just shortly afterwards (<2s in this case) the spray temperature shows a uniform distribution with saturation temperatures. Such temperature distributions can be explained as follows:

Initially, when LN<sub>2</sub> is injected into the low pressure chamber, the spray becomes superheated owing to the sudden depressurization. The resulting flash atomization and vaporization is at the expense of the liquid jet's latent heat of vaporization, resulting in a large temperature drop at a short time. TC2 is located closer to the injector orifice, and it responds earlier to this large temperature drop (see the large slope of the TC2 curve). Due to the temperature drop, the rest of the spray at the place where TC3 ~TC6 are instrumented has lower superheat, thus triggering a weaker atomization and vaporization, leading to a slight local temperature fall (see the small slopes of TC2 to TC6). In addition, the heat transfer between the spray jets and the surrounding also contributes to this temperature change. Because of the low concentration of the liquid phase downstream the injector, the warmer ambience dominates the heat transfer (i.e. heat convection and radiation), as a consequence, hinders the temperature drop.

As the injection continues, the massive atomization and evaporation of LN<sub>2</sub> consumes more latent heat of vaporization. Also the large concentration of the liquid spray downstream the injector will dominate the heat transfer between the spray and the warmer surrounding. Both effects cool down the spray, triggering a more drastic temperature drop. Furthermore, the jet pump used to maintain the vacuum conditions during the test continuously extracts the high temperature ambient vapor out of the system, and the low temperature LN<sub>2</sub> is injected into the chamber. This will decrease the energy of the whole spray and the surrounding and weaken the heat transfer from the surrounding to the spray, additionally leading to the rapid temperature decrease downstream the injection. This faster temperature decrease can be clearly seen in the temperature curves after the kink points.

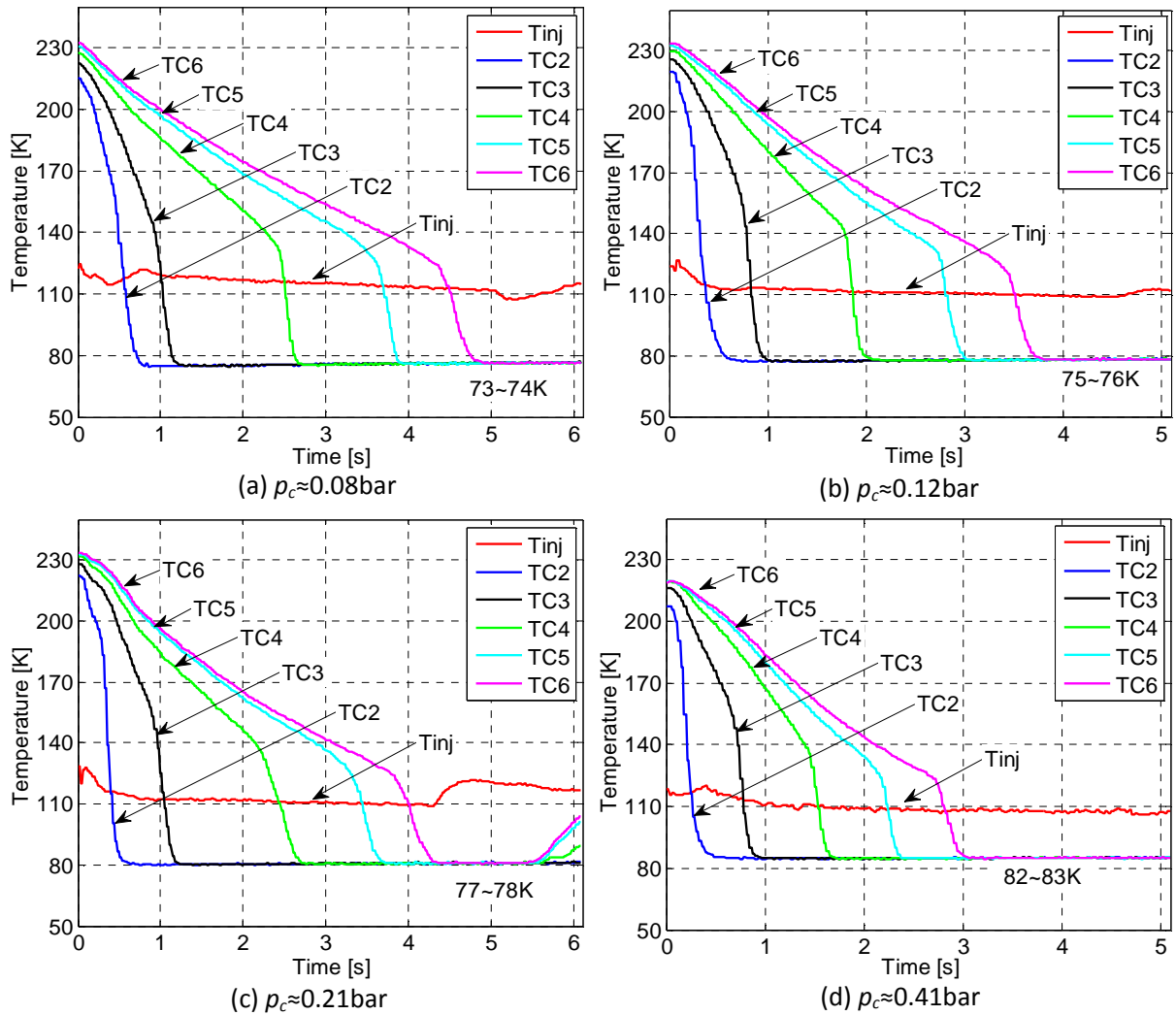


Fig. 3.22 Temperature evolution along LOx spray centerline ( Injector #1)

The thermal distributions of LN<sub>2</sub> and LOx flashing sprays with injector #1 are also presented in Fig. 3.22 and Fig. 3.23. The figures show similar characteristics except the time scale of the spray approaching the quasi-stable state (~5ms), which is due to the different boundary conditions. In Fig. 3.21, the test is conducted with the injector of diameter of 1.5mm. Fig. 3.22 and Fig. 3.23 show the test results of injector with diameter of 0.5mm. Larger injector orifice generates larger mass flow rate of the spray and therefore will generate a larger amount of evaporated vapor. Since the temperature measurement, in principle, is a heat transfer balance between the measured fluids and the thermocouple, the larger amount of evaporated vapor will cool down the thermocouple faster, which as a results, shows a shorter time before relaxing to the quasi-stable state.

### 3. Experimental Investigation of Cryogenic Flashing Spray

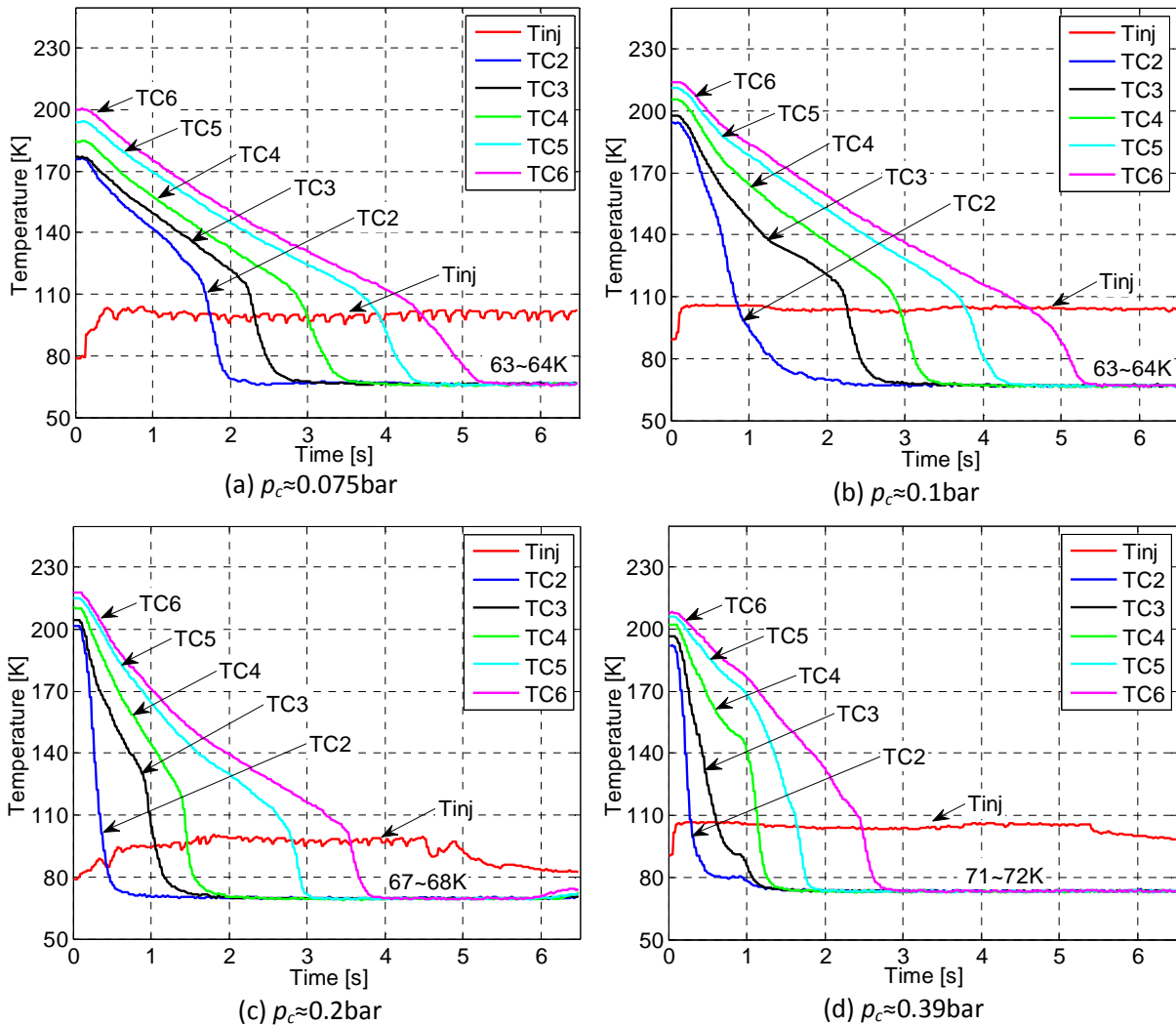


Fig. 3.23 Temperature evolution along LN<sub>2</sub> spray centerline ( Injector #1)

### 3.3.5 Flashing Spray Solidification

In this section, we will closely examine the solidification phase change under the flashing conditions. Kim et al. [92] studied the water spray freezing phenomena under vacuum conditions. The authors pointed out that the large heat transfer from evaporated vapor to water droplets induces the ice formation. In the present experiments, both solid nitrogen and solid methane have been observed in the sudden depressurization process.

Tab. 3.6 Properties of cryogenic fluids (@1.0 bar)

Fluids	$T_{sat}$ (K)	$T_{tri}$ (K)	$p_{tri}$ (kPa)	$T_{sat}-T_{tri}$ (K)	$L_v$ (kJ/kg)	$L_f$ (kJ/kg)
LN <sub>2</sub>	77.2	63.2	12.6	~14	200	25.7
LOx	90.2	54.4	0.15	~36	213	13.9
LCH <sub>4</sub>	111.5	90.7	11.7	~20	510	58.9

Fig. 3.24 shows the deposition of solid nitrogen and solid methane upon the thermocouples during the test. It can be justified as follows. In generally, the sudden pressure drop causes a violent spray atomization and vaporization of LCH<sub>4</sub> and LN<sub>2</sub>, and large amount of the evaporated vapor from the droplet surface is generated by consuming the latent heat of vaporization and sensible heat of the remaining droplet, thus to resulting in a drastic temperature decrease of the remaining droplet, leading to the droplet solidification. Tab. 3.6 lists some properties of the studied cryogenic fluids. It shows that the temperature margins between the boiling point and triple point of LN<sub>2</sub>, LCH<sub>4</sub> and LOx is relatively narrow (<36 K). The small temperature difference makes the phase transition of solidification easy to happen. In addition, the latent heat of vaporization is almost one order of magnitude larger than the latent heat of fusion of these fluids, which indicates that a small amount of vaporization can induce a large amount of liquid to freeze. Therefore, solidification in this situation is favored. According to the table, it shows that the triple point pressure of oxygen is sufficiently low, which is about 1.5mbar. It is out of the vacuum ability of our test setup. This is the reason of the absence of the solid oxygen during the present experiments.

In the test it is found that the existence of solid phase is pressure dependent. When the chamber pressure is below the triple point pressure, the phase change of solidification is likely going on. Once the pressure exceeds the triple point pressure due to the continuous injection and the spray evaporation, the melting or sublimation phase transition occurs, instead.

From the view of thermodynamics, these phenomena can be schematically explained with the phase change diagram (nitrogen taken as an example, as shown in Fig. 3.11). Initially, the liquid jet is located at Point A. After a sudden depressurization, the ambient pressure drops below the liquid's triple point pressure (Point B'), which makes the liquid largely superheated (metastable liquid). The metastable liquid jet will then experience a phase transition via violent atomization and vaporization. It greatly decreases the spray temperature to generate the solid phase, making the jet reach the local minimum energy (Point C'). Although the jet pump extracts vapor out of the chamber continuously, the chamber pressure still increases slightly due to the spray injection and evaporation. Combined with the heat gained from the warmer surrounding, the fluid's phase transition goes along the solid-gas saturation line. Once the pressure exceeds the fluid's triple point pressure, the solid phase disappears.

In the upper-stage rocket engine, the formation of solid propellant particles may exert several negative influences. Firstly, it may change the local mixture ratio and the mixing process of propellants in the engine transient start-up process, which leads to the engine start up under off-design operation conditions. Secondly, it may cause difficulties to a reliable ignition. The solid phase at or close to the ignitor position will require more external energy for the ignition system to vaporize the propellants. These may potentially cause a delayed or even failed ignition. Moreover, if much solid phase propellants are deposited on the chamber wall, much vapor propellant will be generated inside the chamber once the

### 3. Experimental Investigation of Cryogenic Flashing Spray

---

engine starts. This may trigger the combustion pressure peak, cause the combustion instability, and even damage the chamber structure. Therefore, special attention and action should be taken to the propellants' solidification in the space application (e.g. specific sequence design with short time chill-down process or long time gas-purge process).

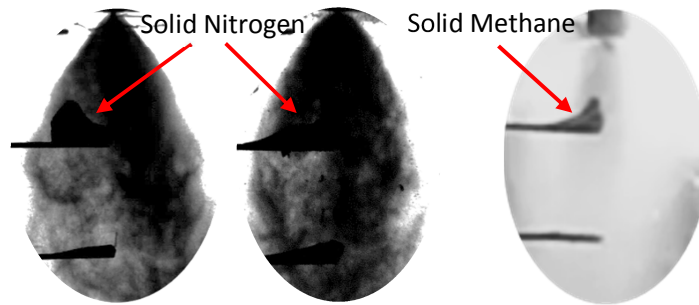


Fig. 3.24 Formation of solid nitrogen and solid methane in the flashing spray

#### 3.3.6 Flashing Atomization Criterion

As the literature study showed in Chapter 2, the flashing atomization is largely different from the normal mechanical atomization due to the superheat boiling effect. This section explains the atomization mechanism of the cryogenic flashing spray from the perspective of nucleation theory. Literature review shows that much valuable research has been conducted to explore the mechanism of flashing spray atomization. Kitamura et al. [21], Cleary et al. [23] and Witlox et al. [34] studied the flashing of superheated jets, and proposed an empirical correlation for prediction of the onset of flashing atomization using the dynamic parameters such as the Weber number and Jacob number. However, under flashing conditions, the nucleate boiling will play an important role in the spray atomization. It is therefore more reasonable to consider the thermal parameter rather than the dynamic parameter in such spray study. With this consideration, Lamanna et al. [31] focused their attention on the thermodynamic aspect of the flashing spray atomization. Based on the nucleation theory, the authors employed the Gibbs number for prediction of the flashing atomization regimes, as described in Eq. (3.9). The proposed parameter is in an order of magnitude of 0 when the fully flashing happens.

$$\chi = \frac{\Delta G^*}{k_B T_{ij}} \sim \frac{\text{Nucleation Barrier}}{\text{Average Thermal Motion Energy}} \quad (3.9)$$

Lienhard and Karimi [93] studied the limit of homogeneous nucleation in a liquid and argued that the homogeneous nucleation (featured by explosive flashing spray) could be predicted through a comparison between the nucleation barrier and “potential well energy” (energy required to breakup the molecule bound) rather than the molecular thermal motion energy. The proposed parameter is described in Eq. (3.10). The value is in an order of magnitude of 1 when the explosive flashing occurs.

$$\xi = \frac{\Delta G^*}{k_B T_{cri}} \sim \frac{\text{Nucleation Barrier}}{\text{Molecular Bound Break Energy}} \quad (3.10)$$

In the present study, the cryogenic flashing experimental data show that both the above-mentioned parameters find their limitation in the indication of the studied flashing sprays, though the parameter  $\chi$  shows better results than  $\zeta$ . Specifically, the parameter  $\chi$  functions well at low injection temperatures, but it could not predict good results at high injection temperatures [27, 59]. In order to eliminate the effect of the injection temperature, a new parameter is employed in replacement of the initial injection temperature and the critical temperature in Eq. (3.9) and Eq. (3.10), as shown:

$$\zeta = \frac{\Delta G^*}{k_B \Delta T} = \frac{\Delta G^*}{k_B (T_{inj} - T_{sat(p_c)})} \sim \frac{\text{Nucleation Barrier}}{\text{Excessive Average Thermal Motion Energy}} \quad (3.11)$$

This parameter describes the relationship between the bubble nucleation barrier and the excessive thermal energy. It means that the flash-boiling depends not only on the nucleation barrier itself, but also on the thermal motion energy available to the cluster molecules, instead of the initial thermal fluctuation energy or the “potential well energy”. Since the flashing phenomenon is in essence a thermodynamic transition process, not only the initial thermal state but also the final thermal state exerts its influence on this process. Therefore, the excessive averaged thermal motion energy is reasonable to be used.

Considering the definition of nucleation barrier, see Eq. (2.13) in Chapter 2, the new parameter is expressed by

$$\zeta = \frac{\Delta G^*}{k_B \Delta T} = \frac{16\pi}{3} \frac{\sigma^3 (v^l)^2}{(k_B T_{inj})^3 [\ln(R_p)]^2} \frac{T_{inj}}{\Delta T} \quad (3.12)$$

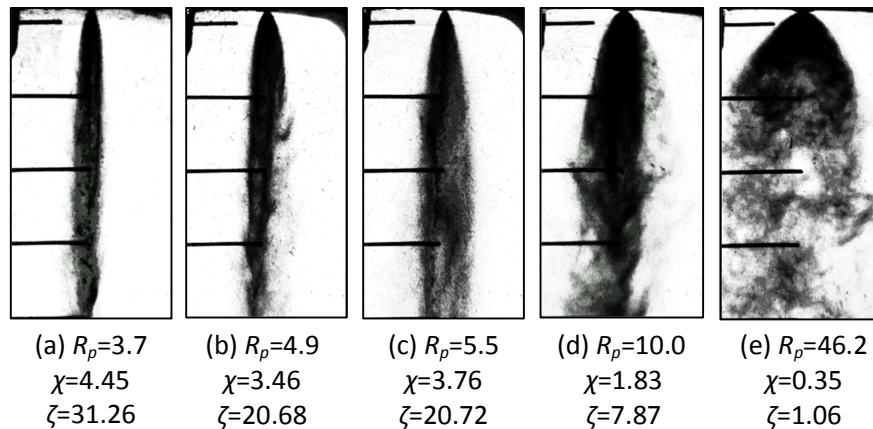


Fig. 3.25 LN<sub>2</sub> flashing evolution process at different superheat degrees ( $p_{inj} \sim 10$ bar, Injector #3)

### 3. Experimental Investigation of Cryogenic Flashing Spray

Fig. 3.25 displays LN<sub>2</sub> spray images under different superheat conditions with injector #3. The injection temperature is within a range of 87K to 93K. The superheat degrees as well as the corresponding  $\zeta$  and  $\chi$  are listed below the respective images. Under lower superheat conditions, e.g.  $R_p=3.7$ , the disintegrated smaller liquid ligaments or droplets can be seen, and the spray shows the typical characteristics of mechanical atomization. The corresponding parameter  $\zeta$  is higher than 30. As the superheat level increases, the parameter  $\zeta$  is decreasing instead. When the superheat is around 46, the  $\zeta$  has a value as small as about 1 or even smaller than 1, under which the spray shows fully flashing features with a violent atomization and wide spray lateral propagation (bell-shaped spray profile).

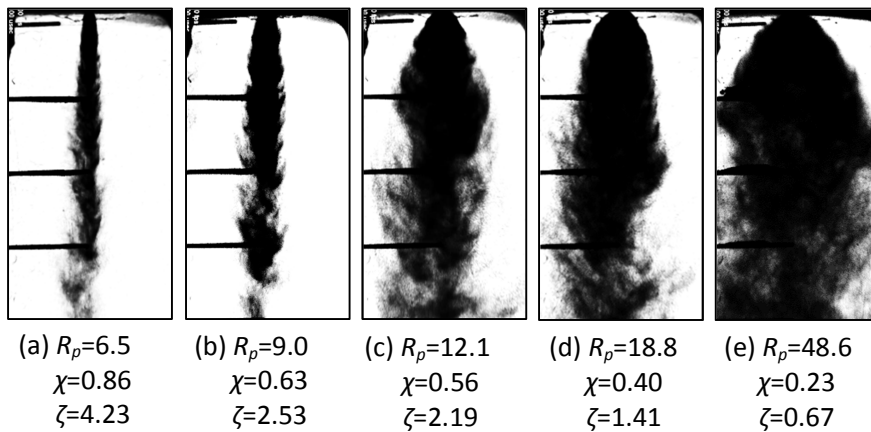


Fig. 3.26 LN<sub>2</sub> flashing evolution process at different superheat degrees ( $p_{inj} \sim 8\text{bar}$ , Injector #4)

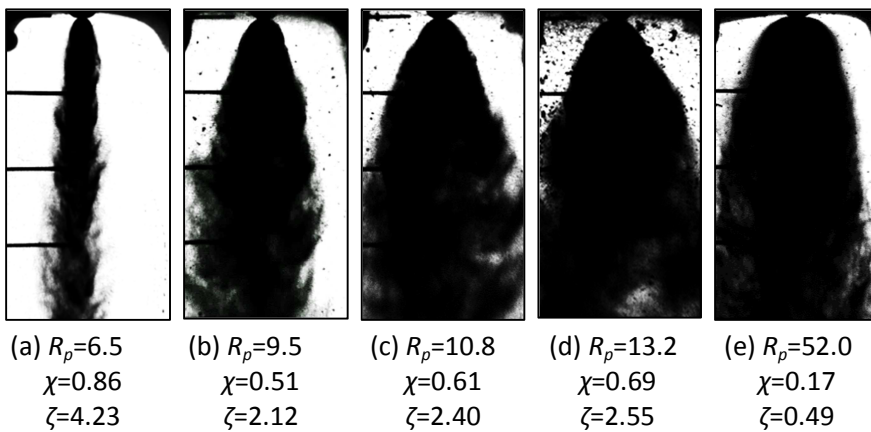


Fig. 3.27 LN<sub>2</sub> flashing evolution process at different superheat degrees ( $p_{inj} \sim 8\text{bar}$ , Injector #5)

Fig. 3.26 and Fig. 3.27 show LN<sub>2</sub> spray evolution at different superheat levels of injector #4 and injector #5. The spray injection temperature is about 97K~98K. The superheat degrees with the corresponding  $\zeta$  and  $\chi$  are also listed under each image. Due to the higher injection temperature  $T_{inj}$ , the liquid surface tension  $\sigma$  is lower than that in Fig. 3.25. This leads to a smaller parameter  $\zeta$ , since  $\zeta$  is proportional to

$(\sigma/T_{inj})^3$  (see Eq. (3.12)). To be more specific, at the low superheat conditions, e.g. in Fig. 3.26a and Fig. 3.26b, the sprays typically show the mechanical atomization features, and the corresponding  $\zeta$  is much larger. With the superheat degree increasing, the spray undergoes the flashing transition and shows a fierce atomization, exemplified in Fig. 3.26d. In cases alike, a parameter larger than 1 is expected. When the superheat level increases further, such as in Fig. 3.26e and Fig. 3.27e, the superheat level reaches up to a value about 50, whereas the answering parameter  $\zeta$  drops below 1. These images show the fully flashing phenomenon.

From the above analyses, we can see that under different superheat conditions, in response to different atomization regimes (i.e. mechanical atomization, flashing transition atomization and fully flashing atomization), the non-dimensional parameter  $\zeta$  has a distinguished value in different regimes. Yet it seems to follow a rough rule. Under this rule, the parameter can classify these atomization regimes with a threshold value around 1. The mechanical atomization corresponds to the value much larger than 1 and the fully flashing regime corresponds to the value smaller than 1.

Follow-up tests of LN<sub>2</sub>, the LOx spray tests are conducted to validate the new parameter. Fig. 3.28 to Fig. 3.31 display the recorded Schlieren images of some test cases with injector #1 as an example. The analysis results confirm our presumption and demonstrate that in the mechanical atomization regime,  $\zeta$  is larger than 1, the flashing transition regime corresponds to a value around 1, and the value is less than 1 in the fully flashing regime. The feasibility of parameter  $\zeta$  can be checked against its definition in Eq. (3.11). The parameter compares the energy required for nucleation formation with the energy available to the molecule. Under the low superheat conditions, where the mechanical atomization has a dominant role, the excessive molecule thermal energy is rather small even though the molecule thermal energy might be high, (this is why we use the  $\Delta T$ ), and the molecule cluster could not overcome the nucleation barrier for bubble formation and further growth. As a consequence, the spray shows a weak atomization. The parameter  $\zeta$  in this regime has a value much larger than 1, coincident with the theoretical analysis.

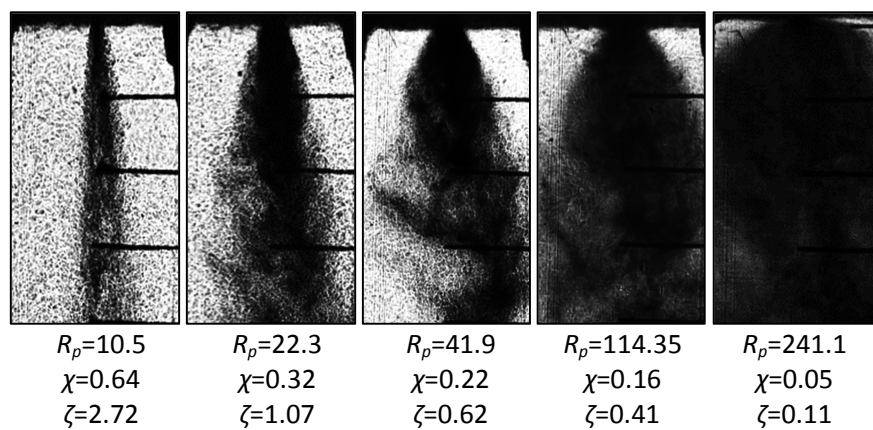


Fig. 3.28 LN<sub>2</sub> flashing evolution process at different superheat degrees ( $p_{inj} \sim 10$ bar, Injector #1)

### 3. Experimental Investigation of Cryogenic Flashing Spray

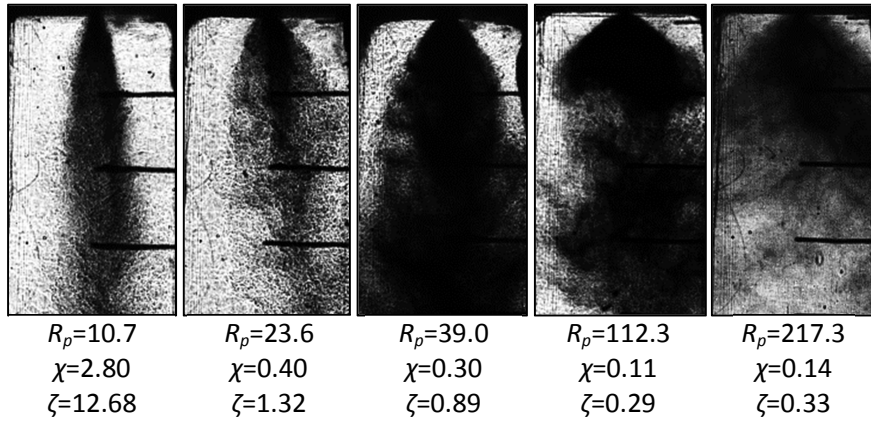


Fig. 3.29 LOx flashing evolution process at different superheat degrees ( $p_{inj} \sim 10\text{bar}$ , Injector #1)

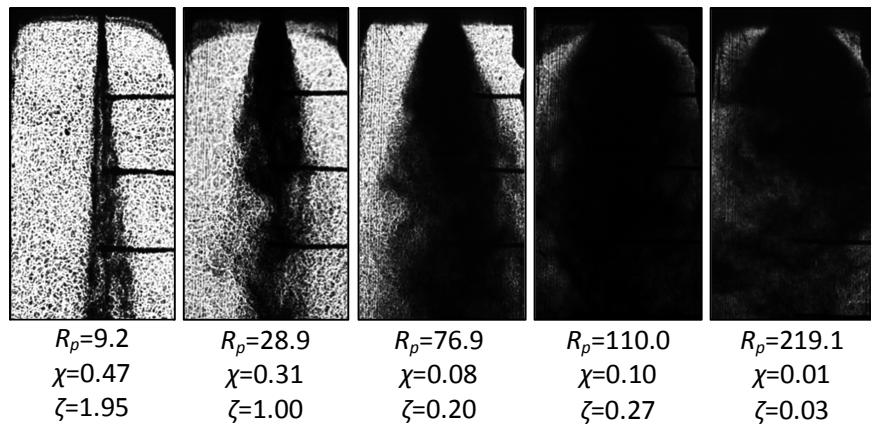


Fig. 3.30 LN<sub>2</sub> flashing evolution process at different superheat degrees ( $p_{inj} \sim 15\text{bar}$ , Injector #1)

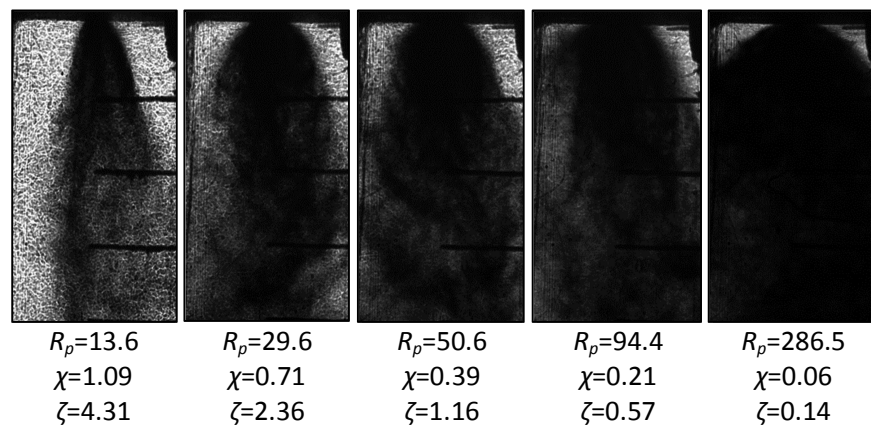


Fig. 3.31 LOx flashing evolution process at different superheat degrees ( $p_{inj} \sim 16\text{bar}$ , Injector #1)

The test data are analyzed statistically and the corresponding parameters  $\zeta$  are estimated. A large amount of tests are conducted under different operation conditions, with the injection temperature of LN<sub>2</sub> ranging from about 85K to 110K and of LOx within a range of around 100K to 120K. Fig. 3.32 plots the parameter values under different superheat conditions of the LN<sub>2</sub> and LOx spray.

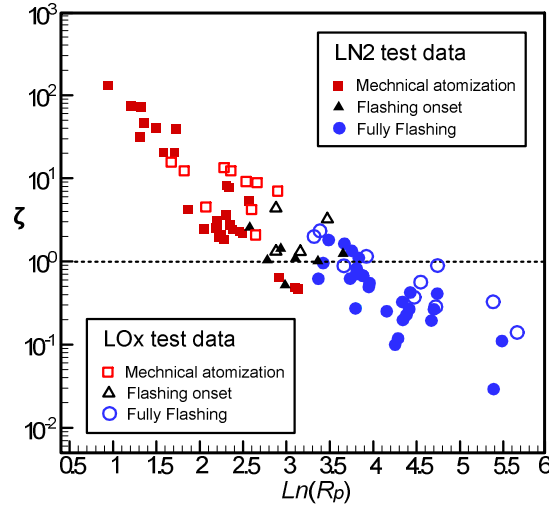


Fig. 3.32 Parameter  $\zeta$  under different superheat conditions

Quantitatively, the fully flashing transition occurs when the parameter  $\zeta$  is around 1, and a value smaller than 1 corresponds to the fully flashing regime, and the parameter with a value much larger than 1 indicates the mechanical atomization regime. It is obvious, however, that there are some exceptions in the diagram. For example, in some test cases of fully flashing regime, the parameter  $\zeta$  is larger than 1. The main reason is supposed to be the evaluation of the nucleation barrier. The  $\zeta$  larger than 1 in the fully flashing regime is found to be associated with a low injection temperature (e.g.  $T_{inj}/T_{cri} < 0.7$ ), under which, the mechanical atomization or heterogeneous nucleation exerts a considerable influence on the spray. However, for the calculation of the parameter  $\zeta$  (see Eq. (3.12)), the homogeneous rather than the heterogeneous nucleation barrier is used. Since the homogeneous nucleation barrier is higher than that of the heterogeneous nucleation, it will inevitably lead to a large  $\zeta$  under such conditions, and the exceptional larger  $\zeta$  as well as the inconsistency makes sense.

### 3.4 Summary

This chapter mainly describes in detail the experimental work of the cryogenic flashing sprays (i.e. LN<sub>2</sub>, LCH<sub>4</sub> and LOx). The characteristics of these flashing sprays, i.e. the flashing evolution process, transition criteria, temperature distribution, spray lateral propagation and spray solidification are analyzed and discussed at great length. Some conclusions are summarized as follows:

### 3. Experimental Investigation of Cryogenic Flashing Spray

---

1). The morphological study shows that with the degree of the superheat increasing, the spray jet undergoes a complex evolution, from the mechanical atomization regime to the fully flashing regime. The fully flashing spray is featured by a bell-shaped spray profile with a large spray angle and fine spray droplets. Analyses of the lateral spray propagation indicate that the superheat enlarges the spray angle. The temperature along the spray centerline shows a decrease followed by a sharp temperature drop prior to the saturation temperature that corresponds to the chamber pressure. In addition, in the stable state, the temperature distribution remains uniform. During the test, solid nitrogen and solid methane have been observed as a result of the massive atomization and vaporization. However, solid oxygen failed to be observed, which is attributed to the higher operation chamber pressure (~40mbar) than the triple point pressure of oxygen (~1.5mbar).

2). Based on the nucleation theory, a non-dimensional energy barrier  $\zeta$  is proposed for the classification of atomization regimes of the flashing spray. From the spray mechanical atomization regime to the fully flashing regime, the value of the parameter  $\zeta$  correspondingly decreases from much larger than 1 to less than 1, and in the onset of the fully flashing regime,  $\zeta$  is around 1.

3). This chapter provides a comprehensive insight into the flashing phenomena with cryogenic fluids. The results are beneficial to the design of the upper-stage rocket engine. For example, the parameter  $\zeta$  could specifically provide some information about the critical boundary conditions that trigger the fully flashing phenomena. The investigation of the spray droplet solidification is beneficial to understand and thus to avoid the potential risks, i.e. ignition delay, engine hard start-up and combustion pressure peak.

## Chapter 4. Investigation of Cryogenic Spray with Rainbow Refractometry

The previous chapter describes the morphological study of cryogenic sprays. In this chapter, for quantitative measurements, the Global Rainbow Refractometry (GRR) is for the first time applied to investigate the cryogenic spray droplets (i.e.  $\text{LN}_2$ ,  $\text{LOx}$  and  $\text{LCH}_4$ ), thus to characterize the spray droplet temperature and size. This chapter mainly includes three parts: design and establishment of the GRR setup; development of inversion algorithms for the data processing based on the light scattering theory; analyses of the obtained rainbow patterns, from which to retrieve the droplet temperature and size.

### 4.1 Introduction

Over the last few decades, much research was dedicated to the investigation of cryogenic sprays. The Schlieren technique and Shadowgraph technique were widely employed to conduct the morphological study of cryogenic propellant spray under subcritical and supercritical pressure conditions [28, 94]. However, test data of quantitative characteristic of cryogenic sprays are still lacking due to the extreme harsh boundary conditions. NASA reports show that some test results of the  $\text{LN}_2$  spray have been obtained with the scattered light scanner technique and Malvern particle analyzer technique [95, 96]. Various test campaigns with  $\text{LOx}/\text{H}_2$  were performed at DLR and ONERA to study the  $\text{LOx}$  spray atomization using Phase Doppler Anemometry (PDA) and Particle Tracking Velocimetry (PTV) [97]. As for the thermal characteristics of cryogenic sprays, few test data are available. Even the Laser Induced Fluorescence (LIF) technique, relying on the photoluminescence processes, finds its limitation in the cryogenic spray application due to the condensation or solidification of fluorescence tracers at the low temperature. In the late 1980s, Roth et al. [98] proposed a Standard Rainbow Refractometry (SRR) technique, which obtained the single spherical droplet refractive index and size information simultaneously. This technique is based on light scattering principles (e.g., Lorenz-Mie scattering theory). With analysis of the angular scattering patterns, one can obtain both droplet refractive index and the size information simultaneously for perfectly droplets. After its emergence, this technique was developed into the Global Rainbow Refractometry (GRR) by van Beeck and Riethmuller [99] in the late 1990s, to investigate the ensemble of droplets (including non-spherical droplets). To date, the rainbow refractometry has proved its capacity to measure the species concentration [100, 101, 102], temperature of burning droplets [103] and droplets with a inhomogeneous temperature [104, 105]. However, to the best of our knowledge, no reports have so far shown the application of this technique to the typical

cryogenic liquid sprays. In this chapter, the GRR technique is employed to quantitatively investigate the cryogenic spray droplets (i.e. LN<sub>2</sub>, LOx and LCH<sub>4</sub>) to extend our previous morphological studies.

## 4.2 Rainbow Phenomenon

The rainbow is a common phenomenon, which is caused by light reflection, refraction, and dispersion in transparent droplets. Many theories contribute to the understanding of this phenomenon, such as the geometrical optics theory, Airy approximation, Lorenz-Mie theory, Debye-series method, complex angular momentum theory (CAM), and catastrophe theory [106]. Among them, the Lorenz-Mie theory is the most complete and rigorous but is also the most computationally time-consuming. Fig. 4.1a shows a typical scattering signal for a spherical water droplet, calculated by Lorenz-Mie theory in the neighborhood of the rainbow angle ( $D=100\mu\text{m}$ ,  $m=1.335+1\text{e-}8\text{i}$ ), and the method can be found in Appendix II. The rainbow angle  $\theta_{rg}$  here refers to the primary rainbow angle that can be calculated by

$$\theta_{rg} = -2\tau_{rg} + 4\arccos\left[\cos^{-1}(\tau_{rg})/m\right]$$

$$\sin \tau_{rg} = \sqrt{(m_0^2 - 1)/3}$$
(4.1)

where  $m_0$  is the ratio between the real part of the refractive index of the droplet and the one of the medium.  $\tau_{rg}$  is the incident angle (see Fig. 4.1a) for which the corresponding scattering angle is the geometric rainbow angle  $\theta_{rg}$ . The angle  $\theta_{rg}$  corresponds to the minimum deviation of light rays that have undergone one internal reflection. This characteristic of concentration of light rays near  $\theta_{rg}$  gives rise to the (primary) rainbow with a high scattering intensity.

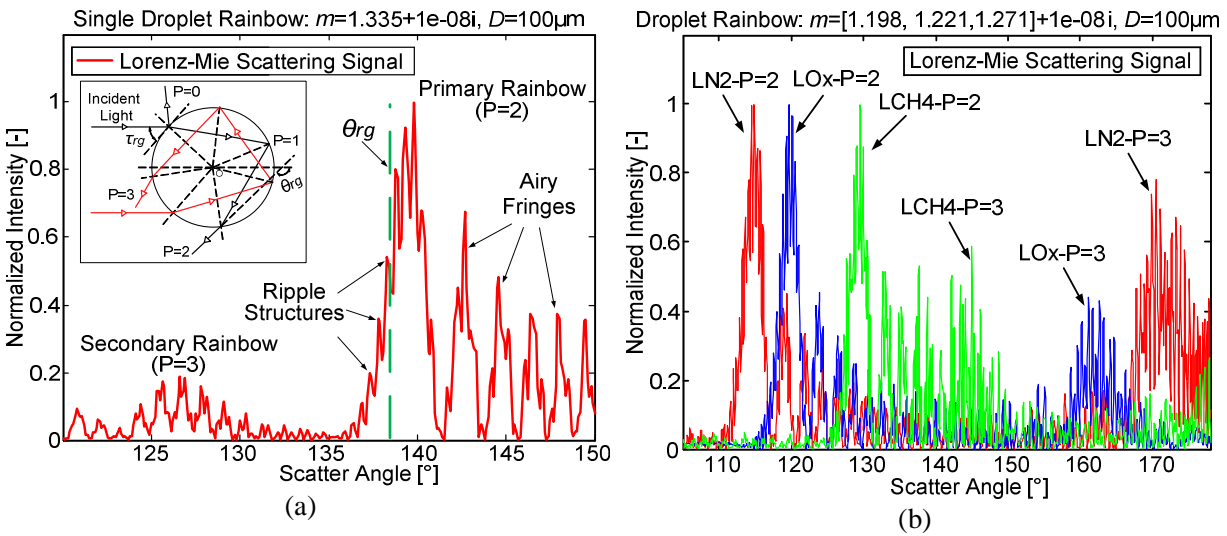


Fig. 4.1 Single droplet scattering intensity near the rainbow angle

It is clear in the figure that the scattering light intensity is characterized by the supernumerary arcs (Airy fringes) superimposed with the high frequency oscillation structures (ripple structures). The Airy fringes are caused by the interference of the internally reflected light. The ripple structures are the results of the interference between the light rays from the internal reflection and external reflection of the droplets [107]. In Fig. 4.1a, the primary rainbow corresponds to rays that have undergone one internal reflection ( $P=2$ , as illustrated in the subfigure in Fig. 4.1a). The secondary rainbow results from the second internal reflection ( $P=3$ , see the subfigure in Fig. 4.1a). Fig. 4.1b presents the normalized scattering signals around the primary rainbow angle for  $\text{LN}_2$ ,  $\text{LOx}$  and  $\text{LCH}_4$ , respectively. The three curves present similar features, namely the higher frequency ripple structures along with the Airy fringes of lower frequency. However, the location of the three intensity peaks differs, as the three angles corresponding to their maximum intensity value shift towards larger values. This angle shift is attributed to the increased refractive index of these fluids ( $m$  equals to  $1.198+1e-8i$ ,  $1.221+1e-8i$  and  $1.271+1e-8i$  for  $\text{LN}_2$ ,  $\text{LOx}$  and  $\text{LCH}_4$  respectively).

Also note the similar spacing between the Airy fringes of the involved fluids, which is attributed to the droplet size (defined to be the same with all the three fluids in the calculation). The rainbow for water and the studied cryogenic fluids exhibit some differences. For the water droplet, the secondary rainbow ( $P=3$ ) is located at about  $\theta=128^\circ$ , and the primary rainbow angle at about  $\theta=139^\circ$  ( $P=2$ ). For the cryogenic sprays of  $\text{LN}_2$ ,  $\text{LOx}$  and  $\text{LCH}_4$ , the respective locations are at around  $171^\circ$ ,  $163^\circ$  and  $147^\circ$ , all of which are larger than the corresponding primary rainbow angle. In the present study, we mainly focus on the primary rainbow since it has enough information to derive the results of droplet size and refractive index (temperautre).

## 4.3 Experimental Setup

### 4.3.1.1 Test Setup and Operation Conditions

The study fluids are  $\text{LN}_2$ ,  $\text{LOx}$  and  $\text{LCH}_4$ .  $\text{LOx}$  and  $\text{LCH}_4$  are obtained from the gas liquefaction systems, as described in Chapter 3. The cryogenic fluids are injected into the ambient pressure environment with injector #5 ( $D=1.5\text{mm}$ ,  $L/D=10$ ). The spray mass flow rate is measured by the calibrated injector. The injection pressure was measured by the pressure sensor with a range of 0-10bar and an uncertainty of 0.25% (BFSL). A calibrated type T thermocouple (grounded junction,  $d=1.0\text{mm}$ ) was used for temperature measurement. Tab. 4.1 gives the test conditions.

Tab. 4.1 General test conditions

Test Fluids	$p_{inj}$ (bar)	$T_{inj}$ (K)	$T_{spy}$ (K)	$\dot{m}$ (g/s)	Re	$We_g$
$\text{LN}_2$	2.34	85	80	18.7	$1.79 \times 10^5$	725.3
$\text{LOx}$	1.32	92	89	11.6	$7.25 \times 10^4$	32.3
$\text{LCH}_4$	1.29	113	107	6.7	$6.98 \times 10^4$	39.7

## 4. Investigation of Cryogenic Spray with Rainbow Refractometry

Fig. 4.2 and Fig. 4.3 show the schematic of the test setup for the measurement of the cryogenic spray droplets. The measurement volume (the measured droplets' location) is chosen around the spray periphery about 35 mm downstream the injector orifice. A continuous diode-pumped solid-state laser (LY532) operating at a wavelength of 532nm is used to illuminate the spray. The liquid droplets scatter the polarized laser beam toward the first plano-convex lens ( $f=100\text{mm}$ ,  $d=75\text{mm}$ ), which performs an optical Fourier transform. This means that the position of the scattered light at the focal plane of the first lens depends only on the scattering angle and is independent of the droplet position in the measurement volume. An aperture (spatial filter) is located right at the image plane of this lens to select the measurement volume for droplets in the spray. Only light scattered from droplets through the aperture contributes to the detected rainbow signal. A second lens ( $f=75\text{mm}$ ,  $d=50.8\text{mm}$ ) is used to focus the aperture-filtered light onto a CCD camera. The CCD has a spatial resolution of  $2048 \times 1088$  pixels and the pixel pitch is  $5.5\mu\text{m}$ . The angular position of the rainbow on the CCD is analyzed to determine the droplet refractive index, from which the droplet temperature is finally obtained.

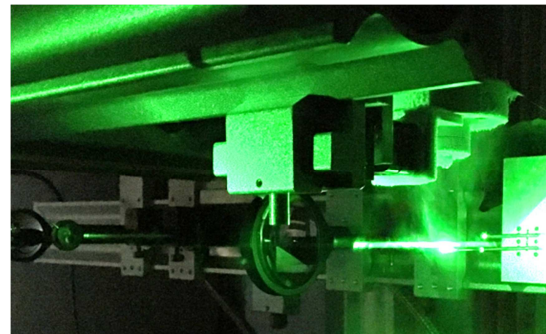
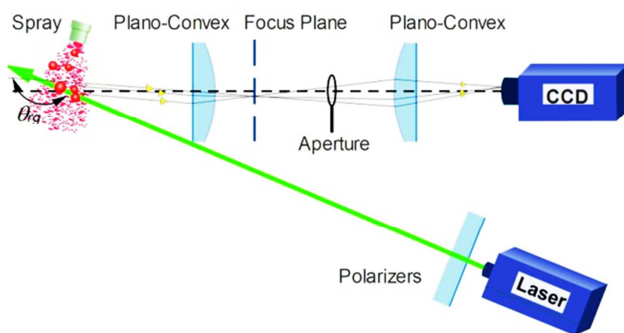


Fig. 4.2 Schematic of Global Rainbow Refractometry

Fig. 4.3 Global Rainbow Refractometry setup

### 4.3.1.2 Rainbow Refractometry Calibration

The correlation between the absolute scattering angle and the rainbow position associated with the CCD pixel is critical for the rainbow signal post-process. Therefore, a calibration of the optical system is needed to obtain such correlation. The calibration is conducted by locating a mirror on a high-precision rotational platform (with a resolution of  $2.4'$ ) at the probe volume (i.e., the position of the measured droplets). By rotating the mirror, the reflected laser rays are recorded on the CCD, thus determining the relationship between the absolute scatter angle and the CCD pixel. Fig. 4.4 schematically illustrates the calibration process. In the figure,  $n$  is the sampled calibration point,  $f(n)$  is the pixel corresponding to location " $n$ ", and  $\theta(n)$  and  $\varphi(n)$  are the absolute scatter angle and the mirror angle. The initial mirror angle  $\varphi(0)$  is determined when the incident laser ray and the reflected ray coincide with each other. Rotate the mirror until the first reflected ray is recorded on the CCD, and mark the mirror angle  $\varphi(1)$  and the corresponding pixels  $f(1)$ . Continue to rotate the mirror cautiously by a specific angle step and record the angles and pixels. Repeat this process to the end point " $n$ ". As a consequence, to every calibration point, the correlation between the CCD pixels and the absolute scatter angle is then determined by

$$\begin{cases} f(1) \rightarrow \theta(1) = \pi - 2[\varphi(0) - \varphi(1)] \\ \vdots \\ f(n) \rightarrow \theta(n) = \pi - 2[\varphi(0) - \varphi(n)] \end{cases} \quad (4.2)$$

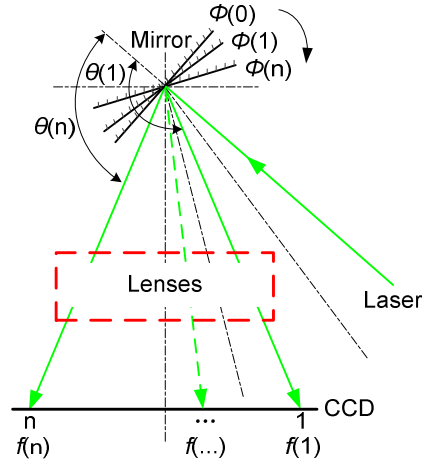


Fig. 4.4 Calibration of the scatter angle and CCD pixels

A cubic polynomial regression is fit to the calibration data, presented in Fig. 4.5.

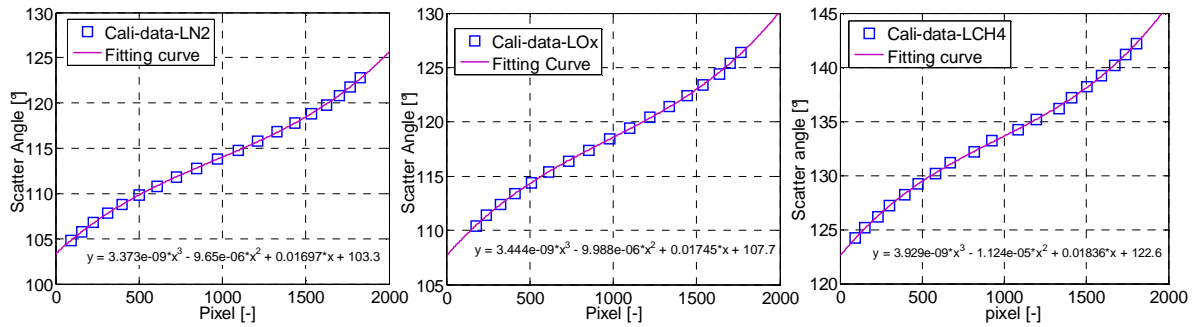


Fig. 4.5 Correlation of the scatter angle with CCD pixels

### 4.3.1.3 Temperature-Refractive Index Correlation

As mentioned before, the rainbow signal provides the information of the refractive index. For a quantitative retrieval of temperature, a describing the dependence of the refractive index on temperature of the desired fluid is required. By means of the Wollaston cell test, Johns and Wilhelm [108] obtained the refractive index of LN<sub>2</sub> and LOx at temperatures ranging from their respective freezing to boiling points at different wavelength. In our test, the temperature-refractive index relationship at a laser wavelength of 532nm is obtained by interpolation of the Johns and Wilhelm's test data. Fig. 4.6 and Fig. 4.7 illustrate the temperature-refractive index relationship for LN<sub>2</sub> and LOx, respectively. Both diagrams

#### 4. Investigation of Cryogenic Spray with Rainbow Refractometry

show a linear relationship, in which a small variation of the refractive index with a value of  $10^{-4}$  corresponds to a large temperature change of about 0.1K. This can provide a high temperature resolution for the final result derivation.

For  $\text{LCH}_4$ , an experimental correlation proposed by Yoshihara et al [109] is employed, as shown:

$$m_{\text{LCH}_4} = 1.384 - \alpha T \quad (@ \lambda = 514.5 \text{nm}) \quad (4.3)$$

where  $\alpha = 9.61 \times 10^{-4} \text{ K}^{-1}$ .

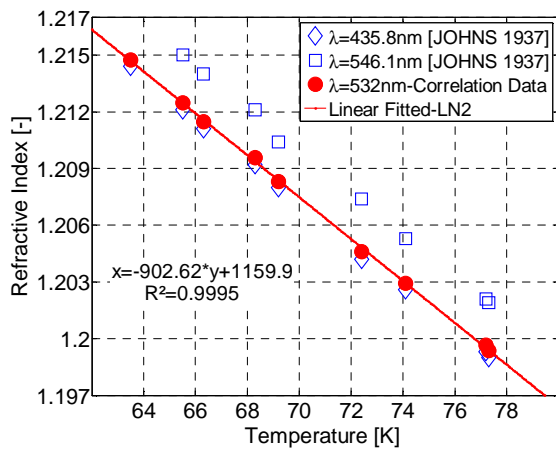


Fig. 4.6 Temperature-refractive index diagram of  $\text{LN}_2$

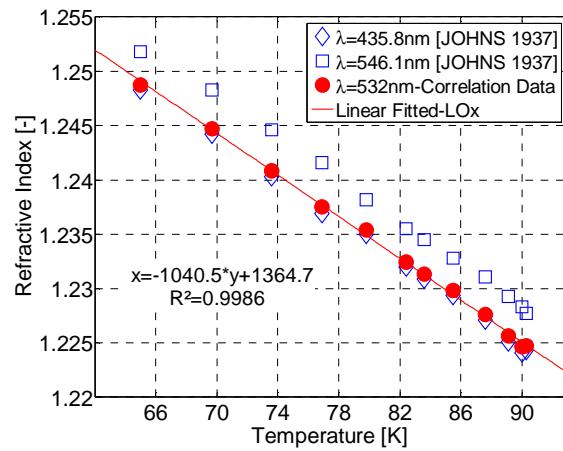


Fig. 4.7 Temperature-refractive index diagram of  $\text{LO}_x$

### 4.4 Data Inversion Algorithms

The data processing algorithms of the rainbow signal are discussed in this section. As mentioned earlier, the rainbow refractometry directly records the scattering interference patterns (Airy fringes with/without ripple structures). Various data inversion methods were developed to extract the droplet refractive index and size from the rainbow signals. Based on the Airy theory, van Beeck et al. [110] and Vetrano et al. [50] proposed an inversion algorithm with the assumption of the droplet size distribution. The authors pointed out that the droplet size can be computed from the Airy fringe spacing (some characteristic points can be chosen) without prior knowledge of the refractive index. Saengkaew et al. [111] developed a method taking all the signal points into account without an assumption of the droplet distribution based on the CAM theory that was proposed by Nussenzveig et al. [112, 113]. This method can yield the results as accurate as Lorenz-Mie theory and as fast as the Airy theory.

According to van de Hulst et al [114], the Airy theory is limited to  $\chi > 5000$  and  $|\varepsilon| < 0.5^\circ$  for obtaining quite accurate results, where  $\chi$  is the size parameter with  $\chi = \pi D / \lambda$  and  $\varepsilon = \theta - \theta_{rg}$ . The CAM theory, however, as Nussenzveig pointed out, can be even applied for  $|\varepsilon| < (2/\chi)^{1/3}$  and  $\chi$  as small as 30 [112]. Taking this into account, the improved van Beeck method, based on the CAM theory instead of the Airy theory, is used to calculate the average droplet size and temperature.

In sum, the data process strategy is performed as follows: the mean droplet size and temperature are calculated with the improved method, as called Characteristic Points Method here (CPM). The size probability distribution and temperature are retrieved with Saengkaew's method, as named Global Points Method here (GPM).

#### 4.4.1 Characteristic Points Method

According to the CAM theory, the scattering intensity of the scattered electric field in the vicinity of the rainbow can be expressed as a linear combination of both the Airy integral and its derivative, as shown in Eq. (4.4) [115] [116]:

$$I(\theta, \chi, m) \propto \left| \text{Ai} \left[ (-\chi^{2/3} \varepsilon / h^{1/3}) u(\varepsilon) \right] - i v(\varepsilon) \chi^{-1/3} \text{Ai}' \left[ (-\chi^{2/3} \varepsilon / h^{1/3}) u(\varepsilon) \right] \right|^2 \quad (4.4)$$

$$\begin{aligned} u(\varepsilon) &= 1 + B\varepsilon + o(\varepsilon^2) \\ v(\varepsilon) &= v_0 + V\varepsilon + o(\varepsilon^2) \\ B &= (875c^6 - 1257c^4 + 657c^2 + 45) / (8640c^3 s^3) \\ s &= \sin(\tau_{rg}) = \sqrt{(m^2 - 1) / 3} \\ c &= \cos(\tau_{rg}) = \sqrt{(4 - m^2) / 3} \\ h &= 3c / (4s^{3/2}) \end{aligned} \quad (4.5)$$

where  $\varepsilon = \theta - \theta_{rg}$ , and  $\chi$  is the size parameter with  $\chi = \pi D / \lambda$ . The expression for  $v(\varepsilon)$  functions as a background to enhance the amplitude of the rainbow intensity thus to avoid a zero intensity of the supernumerary, which has no significant effect on the retrieved results. Here,  $v(\varepsilon) = 0$  [116]. The function  $u(\varepsilon)$  affects the angular position of the supernumerary pattern.

The droplet mean size is determined by considering two characteristic points around the main rainbow with the angular position of  $\theta_i$  and  $\theta_j$ , using Eq. (4.6), where  $z_i$  and  $z_j$  are the Airy function arguments corresponding to  $\theta_i$  and  $\theta_j$ .

$$d_k(\theta, \lambda, m) = \frac{\lambda}{\pi} h^{1/2} \left[ \frac{z_i - z_j}{\varepsilon_i [1 + B\varepsilon_i + o(\varepsilon_i^2)] - \varepsilon_j [1 + B\varepsilon_j + o(\varepsilon_j^2)]} \right]^{3/2} \quad (4.6)$$

#### 4. Investigation of Cryogenic Spray with Rainbow Refractometry

---

From Eq. (4.6), it shows that the droplet size is related to the parameter  $h$ , so it couples with the refractive index. Therefore, the refractive index and the mean droplet diameter are then calculated with an iteration of Eq. (4.1) and Eq. (4.4) - Eq. (4.6) until one satisfies the given convergence conditions.

The global rainbow can be calculated by summing the scattering light of all single droplets, as shown in Eq. (4.7). The power factor “7/3” is the effect of droplet diameter on the scatter intensity.

$$I_{glob}(\theta, \chi, m) = \sum_{i=1}^N I(\theta, \chi, m) d_k^{7/3} \quad (4.7)$$

In data processing, the test signals are filtered (e.g. by FFT) to remove the high-frequency signal caused by the ripple structures and the background noise. By searching for the characteristic points (e.g. extreme points ( $\theta_{max1}$  and  $\theta_{max2}$ ) or inflection points ( $\theta_{inf1}$  and  $\theta_{inf2}$ ), as shown in Fig. 4.8) among the processed signal, the mean droplet size and the refractive index are derived using the CAM theory. In this study, the inflection points are used. The calculation flow chart is shown in Fig. 4.9.

Before the test data processing, the global rainbow signals of sprays simulated by Lorenz-Mie theory were used to assess the method validity and accuracy. The sprays were assumed with Gaussian size distributions with different mean size  $D$  and disperse factor  $\delta$ . The results are depicted in Fig. 4.10 and Fig. 4.11. Fig. 4.10 demonstrates that the derived mean droplet sizes from the rainbow signals by extreme point and inflection point method match well with the prescribed ones. With the prescribed droplet sizes increasing from 40 $\mu\text{m}$  to 200 $\mu\text{m}$ , the results accuracy correspondingly increase from about  $2 \times 10^{-1}$  to about  $5 \times 10^{-2}$ . As to the refractive index, both of the extreme point and inflection point method give out precise results, as shown in Fig. 4.11. The smaller droplet size indicates larger deviations from the calculated refractive index (e.g.  $2 \times 10^{-3}$  for  $D=40\mu\text{m}$  and  $\delta=10\mu\text{m}$ ), and such deviations drop to about  $1 \times 10^{-4}$  when the droplet size increases to 200 $\mu\text{m}$ .

In practice, the second peak of the primary rainbow (see  $\theta_{max2}$  in Fig. 4.8) is difficult to be recorded, especially for the small droplets and large size distribution. Therefore, the extreme point method might find challenges in practical situations. As well the inflection points need more care to estimate the location, since they are more sensitive to the filtering process. However, as discussed above, the inflection point method shows high accuracy as for estimation of the droplet size and refractive index. Therefore, In this study, the the inflection points were used.

#### 4. Investigation of Cryogenic Spray with Rainbow Refractometry

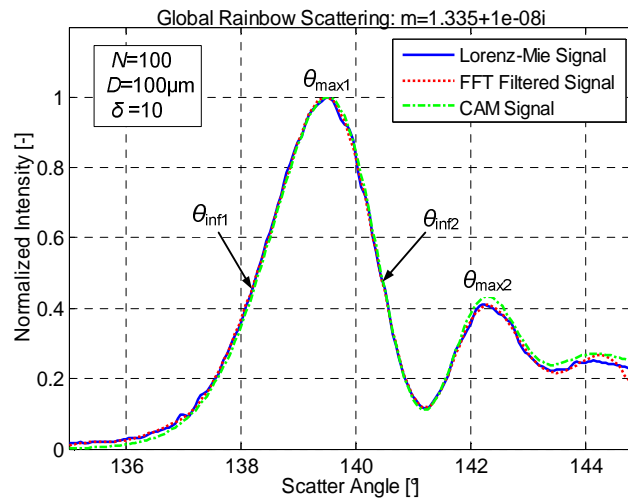


Fig. 4.8 Global rainbow signal of droplet size with Gaussian distribution ( $D=100$ ,  $\delta=10$ )

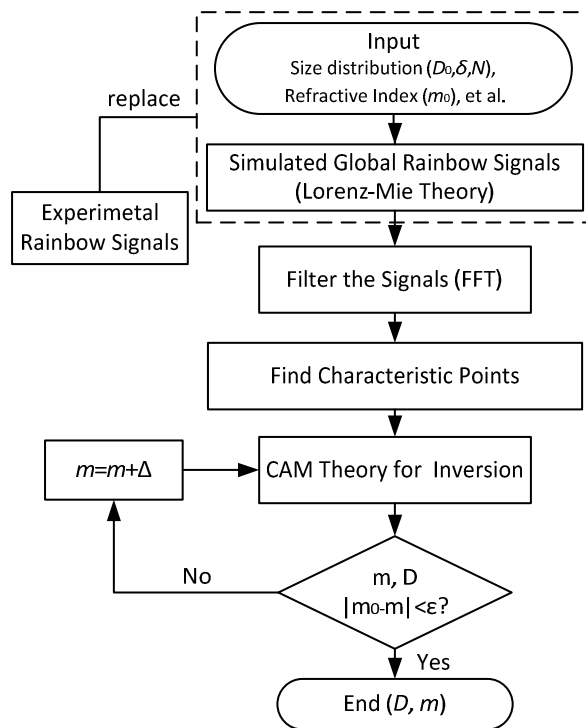


Fig. 4.9 Calculation flow chart of the characteristic point method

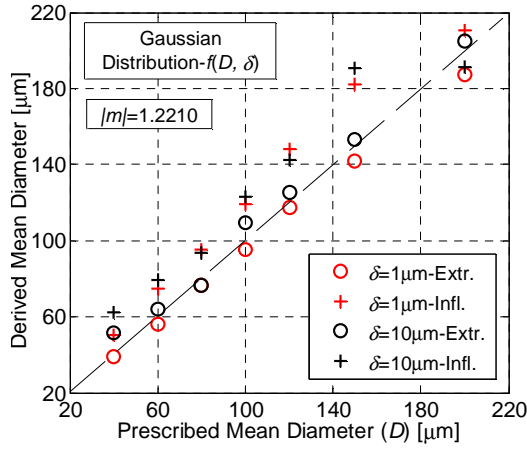


Fig. 4.10 Effect of prescribed droplet distribution on the derived mean diameter

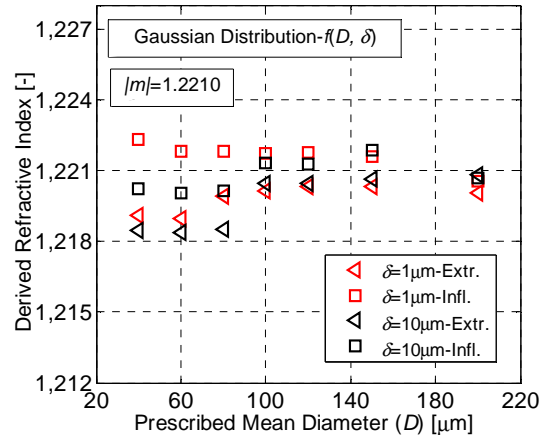


Fig. 4.11 Effect of prescribed droplet distribution on derived refractive index

### 4.4.2 Global Points Method

Considering the non-uniform droplet distribution in the probe volume, the Saengkaew’s inversion method taking into account global points is employed for the further study to get the size probability distribution and droplet temperature. The scattering light intensity equation, shown in Eq. (4.8), is solved using the non-negative least squares algorithm. The retrieved results are optimized using the golden section search and parabolic interpolation. This process iteratively searches for the minimum absolute difference between the sampled rainbow signal and the recomputed rainbow signal until the absolute difference is less than the termination tolerance. Usually it converges after several iterations. The detailed information of this method can be found in Ref. [111, 117].

$$I = AD = \begin{bmatrix} i_1 \\ i_2 \\ \vdots \\ i_n \end{bmatrix} = \begin{bmatrix} a(m, \theta_1, d_1) & a(m, \theta_1, d_2) & \dots & a(m, \theta_1, d_k) \\ a(m, \theta_2, d_1) & a(m, \theta_2, d_2) & \dots & a(m, \theta_2, d_k) \\ \vdots & \vdots & \ddots & \vdots \\ a(m, \theta_n, d_1) & a(m, \theta_n, d_2) & \dots & a(m, \theta_n, d_k) \end{bmatrix} \begin{bmatrix} d_1 \\ d_2 \\ \vdots \\ d_k \end{bmatrix} \quad (4.8)$$

where  $I$  is the intensity vector of the rainbow signals that is recorded by CCD,  $A$  is the scattering matrix coefficient which is computed using CAM theory, and  $D$  is the size distribution vector.

## 4.5 Results and Discussions

The test results of LN<sub>2</sub>, LOx and LCH<sub>4</sub> sprays are analyzed in this section. During the test, it shows that under high Reynolds number conditions (e.g.,  $Re > 10^6$ ), the signal-to-noise ratio of the rainbow is rather poor due to the fine droplet size and the high evaporation rate of such sprays, whose scattering light signal is superposed by the dense vapor reflection signal. A pulsed laser, instead of the continuous wave laser, may be more suitable for capturing the rainbow signal under this condition. For moderate Reynolds number conditions (still turbulent), the interference patterns are rather distinguishable. The primary rainbow, including some supernumerary arcs can be clearly recorded.

Due to its chemically inert safety, LN<sub>2</sub> spray is used as the primary object to test the GRR system. The test is conducted under moderate Reynolds number ( $\sim 10^5$ ) conditions to avoid a fierce atomization and vaporization, but still has enough dynamic force for the liquid jet to breakup into small droplets. Lin and Reitz [86] classifies the liquid jet breakup based on Ohnesorge's categorization, as shown below:

$$\left\{ \begin{array}{ll} a. We_g < 0.4, We_l > 8; & \text{(Rayleigh breakup)} \\ b. 0.4 < We_g < 13; & \text{(First wind induced)} \\ c. 13 < We_g < 40; & \text{(Second wind induced)} \\ d. We_g > 40; & \text{(Atomization)} \end{array} \right. \quad (4.9)$$

The Reynolds number is defined as  $Re = \rho u D_0 / \mu$ , where  $u$ ,  $\rho$ ,  $\mu$  and  $D_0$  are the jet exit velocity, liquid density, kinematic viscosity and nozzle diameter, respectively. The Weber number is expressed as  $We_g = \rho_g u^2 / \sigma$ , where  $\rho_g$  is the vapor density and  $\sigma$  is the surface tension of liquid droplets. The spray Reynolds numbers and the Weber numbers estimated at the injector orifice are about  $1.8 \times 10^5$  and 725 ( $We_g \gg 40$ ), respectively, as shown in Tab. 4.1. Therefore, the LN<sub>2</sub> test falls within the "atomization regime", which confirms that the fluid has enough dynamic force to disintegrate the spray jet.

Fig. 4.12a presents the monochromatic global rainbow pattern of LN<sub>2</sub> spray droplets. The primary rainbow, including some supernumerary structures (Airy fringes), is clearly recorded. The Airy fringes, as aforementioned, are caused by the interference between the adjacent light rays that undergo one internal reflection. The high frequency ripple structures resulting from the interference of internally and externally reflected light are damped by the presence of a large number of small droplets, which produces rather smooth Airy fringes. This can also be seen in Fig. 4.12b, which presents a smooth scattering intensity curve with the absolute scatter angle. The curve is obtained by averaging the intensity value of 40 pixel rows of the rainbow image around the horizontal centerline (see the rectangular region with dash line in the figure), and then by normalizing its maximum intensity. The rainbow signal shows that the global scattering intensity peaks at approximately 114°. To extract the droplet size distribution, the inversion methods discussed in Sec. 4.4 are employed. More than 500 sample points around the rainbow angle are selected for the droplet size derivation, as shown in Fig. 4.12b. The derived results are optimized by comparing the sampled rainbow curve with the recomputed rainbow signal under the given convergence conditions. Fig. 4.12b also plots both the sampled and

#### 4. Investigation of Cryogenic Spray with Rainbow Refractometry

recomputed rainbow signals, which match perfectly with each other. Fig. 4.12c shows the extracted probability distribution of the droplet size. It can be seen that the droplet distribution in the measured volume behaves a bimodal or even multimodal feature, ranging from about 50 $\mu\text{m}$  to 320 $\mu\text{m}$ . The majority of droplets has the diameter of around 130 $\mu\text{m}$ , with another group of large droplets with a diameter of about 320 $\mu\text{m}$ .

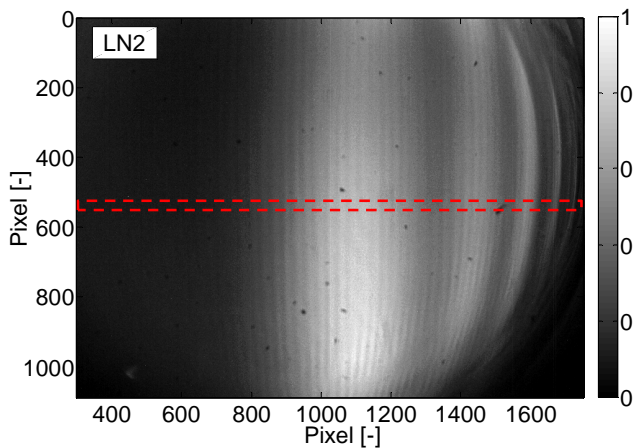


Fig. 4.12a LN<sub>2</sub> rainbow image

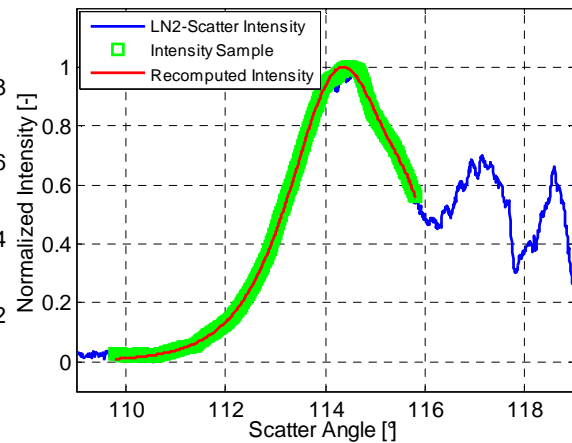


Fig. 4.12b LN<sub>2</sub> rainbow scattering intensity and recomputed intensity

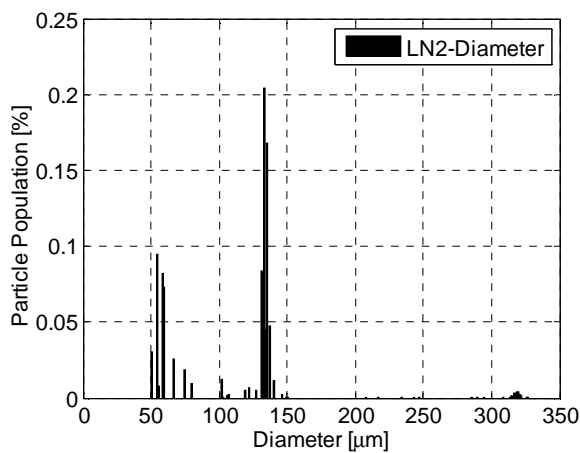


Fig. 4.12c LN<sub>2</sub> droplet size probability distribution

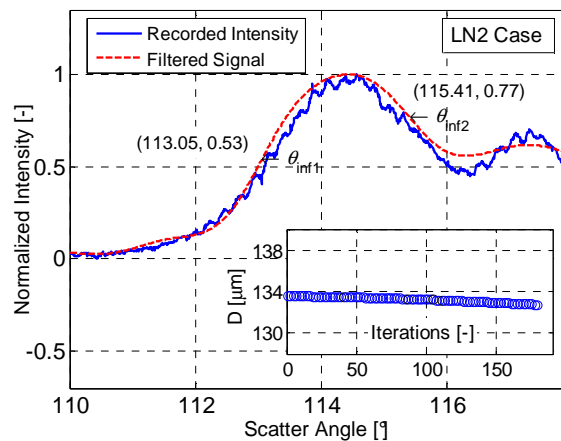


Fig. 4.12d Derived LN<sub>2</sub> droplet mean diameter

The derived mean droplet size and temperature of LN<sub>2</sub> spray are shown in Fig. 4.12d. The detected inflection points of the filtered rainbow signal are plotted, from which the mean droplet size is estimated by iterations until the given convergence criteria are met. The test results of the LN<sub>2</sub> spray are summarized in Tab. 4.2. It reveals that the derived temperatures by both methods are rather similar, at about 78.5K and 78.6K, respectively. Compared to the temperature measured with the thermocouple (80

K), the derived temperature has a small discrepancy of around 2% in this case. With regard to the mean droplet size, both methods give comparable results of around  $130\mu\text{m}$ .

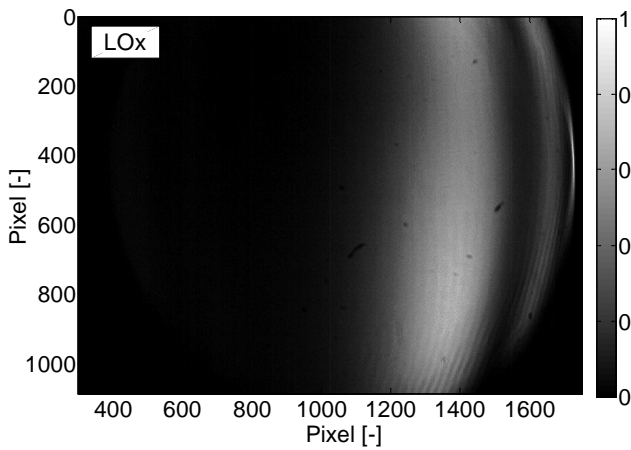


Fig. 4.13a LOx rainbow image

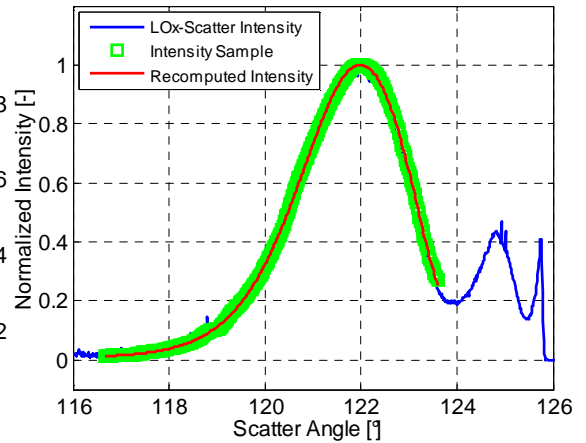


Fig. 4.13b LOx rainbow scattering intensity and recomputed intensity

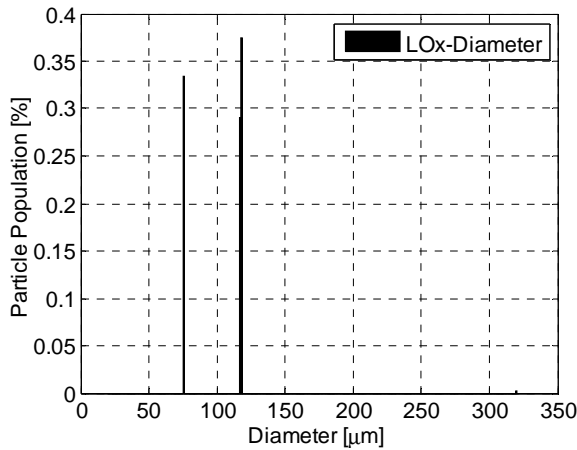


Fig. 4.13c LOx droplet size probability distribution

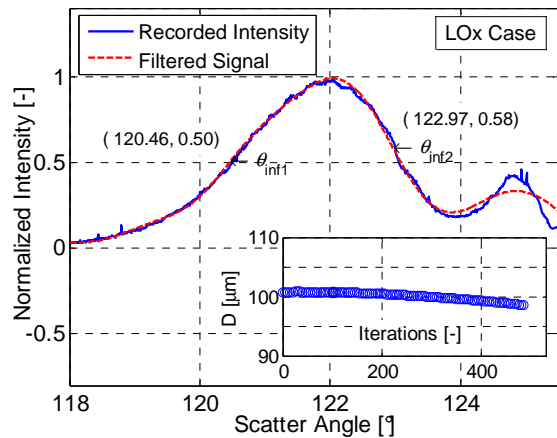


Fig. 4.13d Derived LOx droplet mean diameter

Following the pilot test with the  $\text{LN}_2$  spray, the investigation of the cryogenic propellants of LOx and  $\text{LCH}_4$  is performed. The injection boundary conditions are described in Tab. 4.1.

For LOx and  $\text{LCH}_4$  sprays, the corresponding Reynolds numbers are about  $7.25 \times 10^4$  and  $6.98 \times 10^4$  (turbulent flow), and the respective gas Weber numbers are about 32.3 and 39.7 ( $13 < We_g < 40$ ). Therefore, both sprays are located within the second wind induced atomization regime. Under such

#### 4. Investigation of Cryogenic Spray with Rainbow Refractometry

conditions the spray dynamic inertial force is strong enough to overcome the spray cohesive force, thus disintegrating the spray into small droplets.

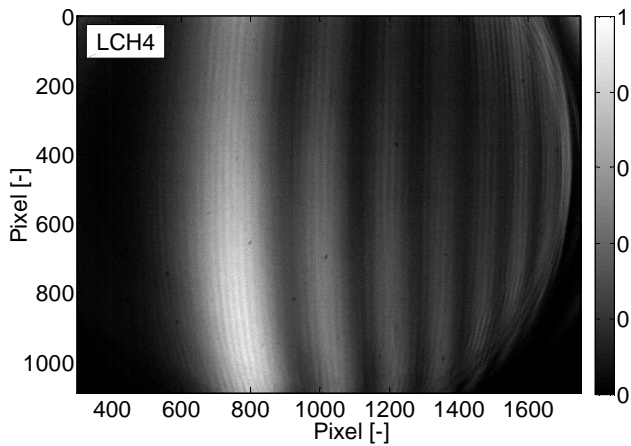


Fig. 4.14a LCH<sub>4</sub> rainbow image

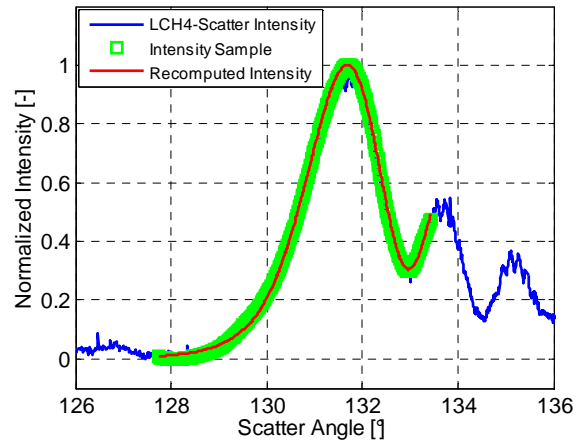


Fig. 4.14b LCH<sub>4</sub> rainbow scattering intensity and recomputed intensity

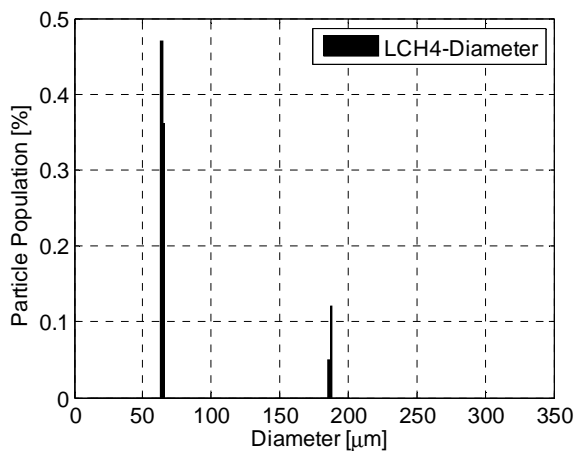


Fig. 4.14c LCH<sub>4</sub> droplet size probability distribution

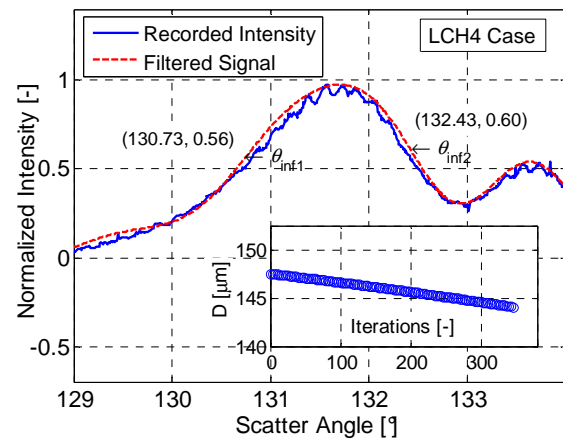


Fig. 4.14d Derived LCH<sub>4</sub> droplet mean diameter

Fig. 4.13a and Fig. 4.14a show the rainbow images for the LOx and LCH<sub>4</sub> spray droplets, respectively. Both images present the typical features of the global rainbow. Fig. 4.13b and Fig. 4.14b describe the relationship between the normalized scattering intensity and the scatter angle. It can be seen that the maximum scattering intensity point (near 122° for LOx and 132° for LCH<sub>4</sub>) of the main rainbow shifts toward a larger scatter angle, compared with that of LN<sub>2</sub> (about 114°). The increased angle corresponding to the maximum scattering intensity is attributed to the large refractive index of these fluids (the refractive indexes of LCH<sub>4</sub> and LOx are larger than that of LN<sub>2</sub>). The retrieved droplet size features a bimodal (see Fig. 4.14c) or even multimodal distribution (see Fig. 4.12c) with the Global Points Method (GPM). In Fig. 4.13c the major population of the LOx droplets has a diameter of around

120 $\mu\text{m}$ , which is comparable to the derived results for droplet sizes ( $\sim 100\mu\text{m}$ ) by the Characteristic Points Method (CPM). The LCH<sub>4</sub> spray droplets mainly have the diameter values of about 60 $\mu\text{m}$  and 190 $\mu\text{m}$ , which is also comparable with the results for droplet sizes ( $\sim 145\mu\text{m}$ ) of this method. From Tab. 4.2, it can be seen that the derived temperatures of LOx and LCH<sub>4</sub> with both methods are close to the directly measured value by the thermocouple, with a relative error of less than 5%. It demonstrates that the GRR technique is quite precise for temperature measurement.

Tab. 4.2 Derived results from Fig. 4.12, Fig. 4.13 and Fig. 4.14

Test Fluids	$D_{mean}$ ( $\mu\text{m}$ )	m	$T_{rg}$ (K)	$T_{test}$ (K)	Error (%)	Method
LN <sub>2</sub>	132.7	1.1979	78.6	80	1.70	CPM
	---	1.1981	78.5		1.91	GPM
LOx	98.5	1.2289	86.0	89	3.36	CPM
	---	1.2299	85.0		4.49	GPM
LCH <sub>4</sub>	144.3	1.2848	103.2	107	1.70	CPM
	---	1.2864	101.6		3.28	GPM

Note that the thermocouple reading value is not the exact temperature of the spray droplets due to the heat transfer between the thermocouple and its surrounding. An analysis is necessary to estimate this discrepancy for temperature correction.

Considering the thermocouple tip, in the equilibrium with the surroundings, the heat loss by radiation is balanced with the heat gain by convection, as shown in:

$$h_{\infty} A_t (T_d - T_t) = \varepsilon_t \sigma A_t (T_t^4 - T_{amb}^4) \quad (4.10)$$

where  $h_{\infty}$  is the heat transfer coefficient,  $T_d$  refers to the droplet temperature,  $T_t$  is the thermocouple measured temperature,  $A_t$  is the droplet surface area,  $\varepsilon_t$  is the emissivity of the thermocouple surface with a value of 0.71 for the inconel sheathed thermocouple, and  $\sigma = 5.67037 \times 10^{-8} \text{ W} \cdot \text{m}^{-2} \cdot \text{K}^{-4}$  is the Stefan–Boltzmann constant.

The thermocouple tip can be approximated as a sphere. Therefore, the convection heat transfer coefficient can be estimated with the Whitaker's correlation [10], which is usually used to the flow over a sphere, as shown in:

$$\overline{Nu}_{D_t} = h_{\infty} D_t / \lambda_d = 2 + (0.4 \text{Re}_{D_t}^{1/2} + 0.06 \text{Re}_{D_t}^{2/3}) \text{Pr}^{0.4} (\mu_d / \mu_s)^{1/4} \quad (4.11)$$

All properties except  $\mu_s$  are evaluated at the liquid temperature  $T_d$ . Since constant properties are assumed, viscosity of liquid farway from the thermocouple surface  $\mu_d$  equals to the one near the thermocouple surface  $\mu_s$ .  $D_t$  is the thermocouple tip diameter ( $D_t = 1\text{mm}$ ),  $\lambda_d$  is the thermal conductivity of the fluid and  $Pr$  is the Prandtl number, which is defined as  $Pr = c_p \mu_d / \lambda_d$ .

Substituting all parameters into Eq. (4.10) and Eq. (4.11), the corrected temperatures of the spray droplets are calculated with the values of 79.993 K, 88.992 K and 106.990 K for LN<sub>2</sub>, LOx and LCH<sub>4</sub>, respectively. This demonstrates that the bias error of the thermocouple measurement, due to heat transfer in the present test cases, is rather small and can be safely ignored.

During data processing, it turns out that the droplet size information extracted from the rainbow signal is sensitive to the inversion algorithms. For the inversion method CPM, which uses the inflection points here, the signal filtering process directly affects the derived droplet diameter. In addition, this method has its limitation in the accuracy of the droplet size measurement, especially when the droplets are of small size and have a wide size distribution. This has been discussed by van Beeck et al. [110]. Even for Saengkaew's method (i.e. GPM), many parameters are required for the inversion input, e.g. number of classes, number of computing points, minima and maxima angles, all of which affect the droplet size results [118]. A further test with PDA is therefore recommended for validation of GRR droplet size. Nevertheless, the implementation of PDA setup is out of the scope of the present work. The refractive index, however, is insensitive to the droplet size, and for both methods, the derived temperature agrees well with the thermocouple measurement value. This proves that the GRR technique can obtain a precise refractive index with a relatively limited sensitivity to droplet size. This feature of the GRR technique facilitates the PDA technique which can provide an accurate measurement of the droplet size if the refractive index is known [119].

## 4.6 Uncertainty Analysis

In this section, uncertainty of the rainbow test system is mainly analyzed from two aspects, i.e. the optical measurement system and the data post-processing.

The precision of the rainbow refractometry is directly influenced by the calibration process that is used to obtain the correlation between the absolute scatter angle and CCD pixels. As aforementioned, a rotational platform with an angle resolution of 2.4' is used for the calibration work. This resolution corresponds to an uncertainty of the absolute angle of  $\pm 0.08^\circ$ . It results in a refractive index error of about  $\pm 4 \times 10^{-4}$ . In post-processing of the test data, the errors from the inversion algorithm itself and from the temperature-refractive index relationship of the particularly studied fluids are mainly considered. The inversion algorithm based on the CAM theory has been validated by Saengkaew et al. [111], which is estimated with an uncertainty of the order of magnitude of  $-4$  ( $\sim \pm 2 \times 10^{-4}$ ) in terms of the refractive index. The derivation of the temperature-refractive index relationship is about  $\pm 5 \times 10^{-4}$  for LN<sub>2</sub> and LOx [108], and  $\pm 2 \times 10^{-4}$  ( $\lambda=514.5\text{nm}$ ) for LCH<sub>4</sub> [109]. Another factor that needs to be taken into account is the laser wavelength. For the LOx and LN<sub>2</sub> tests, the temperature-refractive index relationship with the specific test wavelength (i.e. 532nm) is obtained by correlating the test data in Ref. [108], as shown in Fig. 4.6 and Fig. 4.7. For LCH<sub>4</sub>, however, Eq. (4.3) only provides the temperature-refractive index relationship at the wavelength of 514.5 nm. Therefore, the error caused by the difference between this value (514.5 nm) and the wavelength of the test laser (532nm) should be addressed. Martonchik and Orton [120] measured the refractive index of LCH<sub>4</sub> at the boiling and melting temperatures with different laser wavelengths. These data are fitted by linear regression to obtain the slope of the refractive index versus wavelength,

which is about  $-3.62 \times 10^{-5}/\text{nm}$ . Thus the error caused by the laser wavelength difference (i.e.  $\sim 18\text{nm}$ ) is estimated at about  $7 \times 10^{-4}$ .

The uncertainty of the  $\text{LN}_2$ ,  $\text{LOx}$  and  $\text{LCH}_4$  refractive index is estimated with the Taylor series method of the uncertainty propagation considering all above parameter deviations, as shown in Eq. (4.12) [121]. The corresponding results are  $\pm 7 \times 10^{-4}$ ,  $\pm 7 \times 10^{-4}$  and  $\pm 1 \times 10^{-3}$ . Consequently, the uncertainty of the GRR test is calculated at about  $\pm 0.7\text{K}$ ,  $\pm 0.8\text{K}$  and  $\pm 1.0\text{K}$  in terms of the temperature measurement for  $\text{LN}_2$ ,  $\text{LOx}$  and  $\text{LCH}_4$  sprays, respectively.

$$\Delta T = \sqrt{\sum_{i=1}^N \left( \frac{\partial T}{\partial x_i} \Delta x_i \right)^2} \quad (4.12)$$

The tests for each fluid under similar boundary conditions are undertaken for a statistical study. The test results are shown in Fig. 4.15. The error bar is estimated with the abovementioned uncertainty analysis. The figure clearly indicates that the test data fall within a narrow band with a range of about  $6\text{K}$ , corresponding to a maximum relative error of about  $7.5\%$ . This means that GRR is very precise in the present cryogenic spray investigation, even at extremely low temperatures (e. g. about  $80\text{K}$ ).

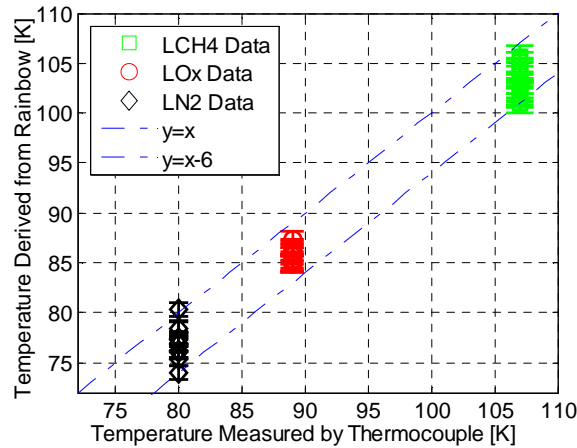


Fig. 4.15 Statistical results of measured temperatures

## 4.7 Summary

The quantitative study of the cryogenic spray is a great challenge due to the extremely harsh boundary conditions of such fluids (e.g. low temperature), and little related research has been reported. In this chapter, the Global Rainbow Refractometry (GRR) technique, which can provide simultaneous measurement of droplet size and refractive index, is for the first time applied to the  $\text{LN}_2$ ,  $\text{LOx}$  and  $\text{LCH}_4$  spray droplets investigation. The GRR setup is built and the test results are summarized as below:

#### 4. Investigation of Cryogenic Spray with Rainbow Refractometry

---

- 1). The global rainbow interference patterns of the cryogenic spray droplets are successfully recorded, which shows the low frequency Airy fringes superimposed with high frequency ripple structures.
- 2). Based on the CAM theory, an improved inversion algorithm is developed. This method obtained comparable results with Saengkaew's method as to the temperature (refractive index) and mean droplet size. The droplet size probability distribution has been obtained with Saengkaew's method, which features a bimodal or multimodal distribution.
- 3). The temperatures measured with the thermocouple are corrected by considering the radiative heat transfer between the thermocouple and its surrounding. The error caused by the heat transfer is in the magnitude of  $10^{-2}$ K, which can be safely ignored. Temperature uncertainty measured with the GRR technique is discussed and estimated to be within  $\pm 1.0$ K, considering the uncertainty both from the optical measurement system and the data post-processing. The derived temperature from the rainbow signal matches well with the temperature measured with the thermocouple. Statistical analysis shows that the GRR derived temperatures present discrepancies within 6 K (relative value of 7.5%) compared with those measured by the thermocouple for the LN<sub>2</sub>, LOx and LCH<sub>4</sub> spray droplets at the temperatures of 80K, 89K and 107K, respectively.

Furthermore, this work also demonstrates the powerful capability of the GRR technique in the cryogenic sprays, which will benefit the study of the cryogenic propellant injection in the space propulsion systems.

# Chapter 5. Modeling of Cryogenic Flashing Spray

In the previous chapters, both the morphological and laser-based quantitative investigation in the cryogenic spray have been performed experimentally. The typical behaviors of the cryogenic spray under low pressure conditions have been obtained. However, some information of the flashing spray is still limited, such as the droplet distribution, the velocity distribution, etc. In addition, the explosive evaporation and even the solidification phase transition have been observed, which implies that different heat transfer with different intensities dominate the flashing process. However, the transient nature of the injection process makes it extremely difficult to qualify the place, time and intensity of these dominating factors. Therefore, a Computational Fluid Dynamics (CFD) work for a further understanding of this spray is necessary. In this chapter, the development and verification of a proper numerical model to unveil some features of the flashing spray will be explored.

This chapter mainly includes three parts: development of a flashing spray model; implementation and validation of the developed model; characterization of the simulated flashing spray (i.e. the spray morphology, the spray temperature, the dominated heat transfers of the spray; the spray velocity, the spray droplet size distribution, etc.).

## 5.1 Introduction

As aforementioned, the flashing phenomenon can occur when a liquid is out of the thermal equilibrium due to a sudden depressurization, which consequently causes bubble formation and growth, spray atomization and vaporization. This is a rather complex non-equilibrium phase change phenomenon and CFD modeling of such flows still remains to be a great challenge. For the typical two-phase flow simulation, the Euler-Lagrange approach is one of the most popular methods, with which the liquid is treated as a Lagrangian discrete phase and the surrounding gas as an Eulerian continuous phase. The two phases can be coupled by taking into account the interphase exchanges of heat, mass and momentum.

The literature study shows that the flashing evaporation models are still lacking, though much effort has been put into the simulation work for the flashing spray. Among them, the thermal equilibrium method and the thermal non-equilibrium method are most frequently used. The thermal equilibrium method presumes an infinite heat transfer flux at the droplet surface, on which the two phases are in thermal

equilibrium. The Homogeneous Equilibrium Model (TEM), employing the thermal equilibrium method, has been widely used [63, 64, 122, 123, 124]. The thermal non-equilibrium method such as Homogeneous Relaxation Model (HRM) assumes that the vapor temperature stays the same as the saturation temperature but is different from the surrounding liquid phase temperature. This model was proposed by Bilckli and Kestin [67] and subsequently been frequently used [68, 70, 125]. Applied the Adachi-correlation [126], Zuo et al. [75] developed and validated a flashing model, by considering both of the flashing evaporation, and vaporization dominated by conduction and convection. This model was later adopted and/or improved by Raju [76], Schmehl and Steelant [77] and Ramcke et al. [78, 79] for the flashing spray study. All the derived models show good computational results, when compared with the experimental data. The difference between these models is the droplet energy equation. Zuo et al. decoupled the external heat transfer from the droplet temperature change, while Ramcke et al. took that effect into account. Nevertheless, none of them consider the radiation effect on the droplet mass evaporation nor the momentum exchange between the discrete and continuous phases. In a flashing spray the discrete phase (fine droplets) will be highly interactive (mass, heat and momentum exchange) with the continuous phase. Therefore, development of a proper numerical model by taking into account the above-mentioned factors is necessary.

## 5.2 Flashing Spray Model Development

Due to its inherent suitability for modeling multiphase sprays, the Euler-Lagrange approach is employed for the computational study of the flashing spray. In this method, the continuous phase (Euler phase) is simulated by solving the unsteady Navier-Stokes equations, while the dispersed phase (Lagrangian phase) is solved by tracking the droplet trajectory under Newton's second law. The two phases are coupled by the exchanges of momentum, mass and heat.

### 5.2.1 Flashing Evaporation Model

Flashing evaporation is different from common evaporation. Under flashing conditions, dependent on the superheat degree, both the internal and external heat transfer will contribute to the fluid evaporation process. Specifically, at low superheat, the evaporation is controlled by heat conduction from the droplet interior, and the heat convection and radiation from the surrounding gas. Under high superheat conditions, i.e. in the fully flashing regime, the internal nucleate boiling will dominate the droplet evaporation. The differences between the normal evaporation and the superheat evaporation can be mainly summarized as follows [75, 76]. Firstly, under flashing conditions (flash boiling), the liquid superheat acts as the internal heat source to keep the droplet surface at the saturation temperature. Therefore, the vapor mass fraction near the droplet surface approaches unity, leading to an infinitely large mass transfer number. In the typical approach, it is then assumed that the whole droplet is evaporated immediately, which seems to contradict the vaporization process at superheated conditions. In addition, when flashing occurs, the external heat transferred from the surroundings is assumed to contribute totally to the droplet evaporation and no external heat is transferred into the droplet. Thirdly, the vaporized mass by flashing will partly counterbalance the vapor flow generated by the external heat

transfer process and thus may reduce the external heat transfer to the droplet. Because of these differences, development of a flashing evaporation model instead of using the common evaporation law is necessary.

### 5.2.1.1 Evaporation by Superheat

Under flashing conditions, as aforementioned, different mechanisms dominate the droplet evaporation. This process is fairly complex and it would not be feasible to consider all the physical aspects. Hence, the internal heat transfer process inside the droplets is simplified by taking into account an effective heat transfer coefficient. Here, the internal heat transfer is modeled with Adachi's empirical correlation [126], in which an effective internal heat transfer coefficient is proposed to describe the evaporation mass flow rate by superheat, as shown:

$$\dot{m}_{flash} = \frac{\alpha_f A_p (T_p - T_b)}{L(T_b)} \quad (5.1)$$

$$\alpha_f = \begin{cases} 0.76(T_p - T_b)^{0.26}, & (0\text{K} \leq \Delta T \leq 5\text{K}) \\ 0.027(T_p - T_b)^{2.33}, & (5\text{K} \leq \Delta T \leq 25\text{K}) \\ 13.8(T_p - T_b)^{0.39}, & (25\text{K} \leq \Delta T) \end{cases} \quad (5.2)$$

where  $\alpha_f$  is the effective internal heat transfer coefficient (with units in kW/m<sup>2</sup>/K),  $A_p$  is the droplet surface area,  $T_p$  is the droplet temperature, and  $L(T_b)$  is the latent heat of vaporization at the boiling temperature  $T_b$ .

### 5.2.1.2 Evaporation by Conduction and Convection

Since the droplets will be highly interacting with the surrounding gas, the conductive and convective heat transfer of the surrounding gas is therefore considered. Fig. 5.1 presents the schematic of a droplet model. The analytical framework is based on the following assumptions:

1. Steady heat transfer process
2. Spherical and symmetric droplet geometry
3. Saturation temperature at droplet surface
4. Spatially uniform temperature distribution inside the droplet ( $Bi < \sim 10^{-2}$ )

The mass conservation equation of the droplet evaporation is shown as below:

$$4\pi r_0^2 \rho_0 v_0 = 4\pi r^2 \rho_r v_r = \dot{m}_{flash} + \dot{m}_{heat} \quad (5.3)$$

where  $\dot{m}_{flash}$  is the flash evaporation rate, which can be calculated with Eq. (5.1),  $\dot{m}_{heat}$  is the evaporation rate by conductive and convective heat transfer, which can be estimated by Eq. (5.7) and  $r_0$ ,  $\rho_0$  and  $v_0$  are the droplet's initial radius, density and evaporation velocity, respectively.

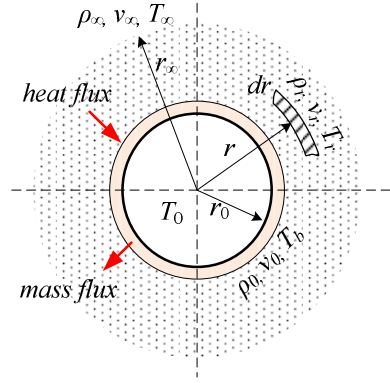


Fig. 5.1 Schematic of droplet model

Considering the net heat flux to a small element, the energy conservation equation, which is derived from the heat diffusion equation in steady state with considering the inner energy generation, can be described as

$$\rho v c_p \frac{dT}{dr} = \frac{1}{r^2} \frac{d}{dr} \left( \lambda r^2 \frac{dT}{dr} \right) \quad (5.4)$$

The boundary conditions of the energy equation are listed as follows:

$$\begin{cases} \left. \frac{dT}{dr} \right|_{r=r_0}^{T=T_b} = \frac{\dot{m}_{heat} L(T_b)}{4\pi r_0^2 \lambda} \\ \left. \frac{dT}{dr} \right|_{r=r_\infty}^{T=T_\infty} = 0 \end{cases} \quad (5.5)$$

By solving Eq. (5.4), Eq. (5.3) with the boundary conditions of Eq. (5.5), and assuming of  $r_\infty \gg r_0$ , the evaporation mass flow rate due to heat conduction between the droplet and surrounding can be evaluated, as shown [75]:

$$\dot{m}_{heat} = 4\pi \frac{\lambda}{c_p} \frac{r_0}{1 + \dot{m}_{flash}/\dot{m}_{heat}} \ln \left[ 1 + \left( 1 + \frac{\dot{m}_{flash}}{\dot{m}_{heat}} \right) \frac{h_\infty - h_b}{L(T_b)} \right] \quad (5.6)$$

When taking into account of the heat convection caused by the relative velocity of the droplets and surrounding gas, based on the film theory, Zuo et al. [75] give a modified equation, as shown:

$$\dot{m}_{heat} = 2\pi \frac{\lambda}{c_p} r_0 \frac{Nu^*}{1 + \dot{m}_{flash}/\dot{m}_{heat}} \ln \left[ 1 + \left( 1 + \frac{\dot{m}_{flash}}{\dot{m}_{heat}} \right) \frac{h_\infty - h_b}{L(T_b)} \right] \quad (5.7)$$

where  $\lambda$  is the thermal conductivity,  $h_b$  and  $h_\infty$  are the gas mixture enthalpies respectively at the droplet surface and far away from the droplet.

Due to the surface boiling, the droplet evaporation will introduce a blowing effect that results in a thickening of the laminar boundary layers around the droplet surface, which consequently decreases the heat transfer between the droplets and the surrounding. The Stefan flow is thus considered in this case. The modified Nusselt number [127] is given by

$$Nu^* = 2 + \frac{0.552 Re_{spe}^{1/2} Pr_{spe}^{1/3}}{F_T} \quad (5.8)$$

where  $Pr$  is the Prandtl number, and  $F_T$  is a universal function of the heat transfer number, defined by

$$F_T = (1 + B_T)^{0.7} \frac{\ln(1 + B_T)}{B_T} \quad (5.9)$$

where  $B_T$  is the Spalding heat transfer number, defined by

$$B_T = \frac{c_{pv}(T_\infty - T_b)}{L(T_b)} \quad (5.10)$$

The thermodynamic and transport properties are evaluated at a specific temperature decided by the one-third rule suggested by Sparrow and Gregg [128], which is shown as follows:

$$T_{spe} = T_b + \frac{T_\infty - T_b}{3} \quad (5.11)$$

### 5.2.1.3 Evaporation by Radiation

Considering the high ambient temperature and the low-pressure conditions, the ambient radiation is taken into account for the spray evaporation, which is given by

$$\Phi_{radi} = \varepsilon \sigma A_p (T_{amb}^4 - T_b^4) \quad (5.12)$$

$$\dot{m}_{radi} = \frac{\Phi_{radi}}{L(T_b)} \quad (5.13)$$

where  $\varepsilon$  is the emissivity of the droplet surface,  $\sigma$  is the Stefan–Boltzmann constant,  $A_p$  is the droplet surface area and  $T_{amb}$  is the ambient temperature.

## 5.2.2 Droplet Energy Balance

Under superheat conditions, all the heat transfer from the surroundings to the droplets is assumed to fully vaporize the liquid surface and none is left to be transferred into the interior of the droplet. Therefore, the droplet temperature is highly dependent on the superheat evaporation and can be decoupled from the external heat transfer. The droplet temperature is updated according to the heat balance between the droplet and the energy loss due to flashing evaporation, as shown:

$$\frac{d(c_p m_p T)}{dt} = -\dot{m}_{flash} L(T_b) \quad (5.14)$$

## 5.2.3 Droplet Trajectory

The droplet trajectory is calculated under the Lagrangian reference frame by solving Newton’s equation of motion via integrating all the forces acting on the droplet, e.g. the drag force, gravity force and some additional forces due to the submicron droplets (pressure gradient, Saffman lift, etc.). The trajectory equation is described in Eq. (5.15). In this research, the drag force plays the most important role in the two-phase momentum exchange. Therefore, the gravity force and some additional forces are ignored.

$$\frac{d\bar{v}_p}{dt} = \frac{18\mu C_D Re}{24\rho_p d_p^2} (\bar{v}_p - \bar{v}) + \bar{g} \frac{(\rho_p - \rho)}{\rho_p} + \bar{F} \quad (5.15)$$

where  $\mu$  is the dynamic viscosity,  $C_D$  is the drag coefficient and  $Re$  is the relative Reynold number that is defined by

$$Re = \frac{\rho |\bar{v}_p - \bar{v}| d_p}{\mu} \quad (5.16)$$

The most important contribution to the two-phase momentum exchange is established by means of a drag force. Therefore, a proper modeling of the drag force is critical for the prediction of droplet trajectory and the turbulent features of the spray. Several empirical or semi-empirical approaches have been developed to model this drag force. Among them, the common drag force “ $C_D Re/24$ ” in the Discrete Phase Model (DPM) simulation is the spherical drag law based on the Morsi and Alexander model, which is shown as below:

$$C_D = a_1 + \frac{a_2}{Re} + \frac{a_3}{Re^2} \quad (5.17)$$

where  $a_1$ ,  $a_2$  and  $a_3$  are different constants in different  $Re$  regions, which can be seen in Ref. [129]. However, for the flashing spray, due to the high superheat, the effect of the droplet evaporation will be increasingly important for the drag force estimation. Actually, evaporation will thicken the boundary layer surrounding the droplet surface and is expected to reduce the droplet drag force [130]. Therefore, the Schiller-Naumann Model, which is commonly used in the spray modeling, is adopted and further modified by the effective evaporation correlation that is proposed by Eisenklam et al. [130]. It is implemented into the force balance equation to predict the droplet trajectory, as shown:

$$C_D = \begin{cases} 24(1 + 0.15Re^{0.687}) / [Re(1 + B_M)], & Re \leq 1000 \\ 0.44 / (1 + B_M), & Re > 1000 \end{cases} \quad (5.18)$$

where  $B_M$  is the Spalding mass transfer number.

### 5.2.4 Source Terms Development

As discussed before, the DPM simulation is performed by solving the Reynolds averaged N-S equation for the continuous phase and addressing the force balance equation for the discrete phase. The coupling (i.e. mass, heat and momentum exchange) of the Eulerian and Lagrangian phases is introduced by adding the corresponding source terms to the governing equations. This section mainly discusses the coupled source terms. Fig. 5.2 is the schematic of the source exchange in a computational cell.

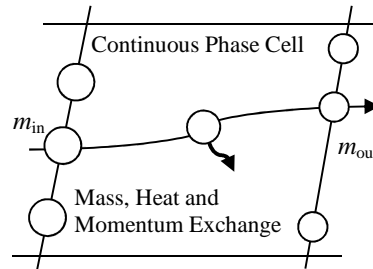


Fig. 5.2 Schematic of the mass, heat and momentum exchange

#### 5.2.4.1 Mass Exchange

The Euler-Lagrange approach considers the mass exchange, which can be added as a mass source term to the mass conservation equation of the Eulerian phase, as shown:

$$\frac{\partial \rho}{\partial t} + \nabla \cdot (\rho \bar{v}) = \underbrace{\varphi_m}_{source} \quad (5.19)$$

The mass transfer from the discrete phase to the continuous phase is computed by examining the change in mass of a particle, as it passes through each control volume. Here, the vaporized mass caused by conductive, convective, radiative heat transfer and flash boiling is taken into account. The mass source is positive when the particles are a source of mass to the continuous phase with the unit quantity of mass-flow, which is

$$\Phi_m = \sum n_{num} (m_{out} - m_{in}) = \sum (\dot{m}_{flash} + \dot{m}_{heat} + \dot{m}_{radi}) \quad (5.20)$$

where  $\varphi_m$  is the volumetric  $\Phi_m$  per cell (i.e.  $\varphi_m = \Phi_m / V_{cell}$ ),  $m_{out}$  and  $m_{in}$  are the respective particle mass at the entry and exit of the current cell,  $n_{num}$  is the particle number flow rate entered the current cell, in unit of “particles/s” and  $N$  denotes the number of particles in the current cell.

#### 5.2.4.2 Heat Exchange

The heat exchange can be added as a heat source term to the energy conservation equation of the Eulerian phase, as shown:

$$\frac{\partial(\rho e)}{\partial t} + \nabla \cdot (\bar{v}(\rho e + p)) = \nabla \cdot \left( \underbrace{(\lambda \nabla T)}_{heat\ conduction} - \underbrace{\sum h_j \bar{J}_j}_{species\ diffusion} + \underbrace{\bar{\tau} \cdot \bar{v}}_{viscous\ dissipation} \right) + \underbrace{\varphi_e}_{source} \quad (5.21)$$

where  $\varphi_e$  is the volumetric  $\Phi_e$  per cell,  $e$  is the specific internal energy,  $\lambda$  is the heat conductivity,  $h_j$  and  $\bar{J}_j$  are the sensible enthalpy and diffusion flux of species  $j$ , respectively, and  $\bar{\tau}$  is the viscous stress tensor, which is given by

$$\bar{\tau} = \mu \left[ (\nabla \bar{v} + \nabla \bar{v}^T) - \frac{2}{3} \nabla \cdot \bar{v} I \right] \quad (5.22)$$

where  $I$  is the unit tensor.

The heat exchange from the continuous phase to the discrete phase is computed by examining the energy change of particle as it goes through each continuous phase cell. The exchange is positive when the particles are a source of heat in the continuous phase and the unit quantity for energy source is power. When the mass is added to the Eulerian phases, the corresponding energy source added to the system is shown as:

$$\Phi_e = \sum n_{num} \left[ -(m_{in} - m_{out}) L(T_b) + m_{in} h_{ss\_in} - m_{out} h_{ss\_out} \right] \quad (5.23)$$

## 5. Modeling of Cryogenic Flashing Spray

---

where  $h_{ss\_in}$  is the particle standard state enthalpy at the entrance of the current cell. The standard state enthalpy is defined as the enthalpy difference between the current state and the reference state ( $T_{ref}=298.15K$ ,  $p_{ref}=1$  atm), as shown:

$$h_{ss} = h_T - h_{ref} = \int_{T_{ref}}^T c_p dT \quad (5.24)$$

The latent heat at the reference condition is defined by

$$L(T_{ref}) = L(T_b) - \int_{T_{ref}}^{T_b} c_{pv} dT + \int_{T_{ref}}^{T_b} c_{pl} dT \quad (5.25)$$

Thus, the heat source added to the system is described as

$$\Phi_e = \sum n_{num} \left[ (m_{out} - m_{in}) L(T_{ref}) + m_{in} \int_{T_{ref}}^{T_{in}} c_{pl} dT - m_{out} \int_{T_{ref}}^{T_{out}} c_{pl} dT \right] \quad (5.26)$$

where  $T_{ref}$  is the reference temperature,  $L(T_{ref})$  is the latent heat of vaporization at the reference state and  $c_{pl}$  is the liquid specific capacity.

### 5.2.4.3 Momentum Exchange

The Euler-Lagrange approach considers the momentum exchange, which can be added as momentum source terms to the momentum conservation equation of the Eulerian phase, as shown:

$$\frac{\partial(\rho \bar{v})}{\partial t} + \nabla \cdot (\rho \bar{v} \bar{v}) = -\nabla p + \nabla \cdot \bar{\tau} + \rho \bar{g} + \underbrace{\bar{\varphi}_{mom}}_{source} \quad (5.27)$$

The momentum transfer from the discrete phase to the continuous phase is computed by examining the change in momentum (x-, y-, and z-direction momentum) of the particle as it passes through each control volume. These values are positive when the particles are a source of momentum in the continuous phase, with the unit quantity of force, as shown:

$$\bar{\Phi}_{mom} = \sum \left( \frac{18\mu C_D \text{Re}}{24\rho_p d_p^2} (\bar{v}_p - \bar{v}) + \bar{F}_{other} \right) \quad (5.28)$$

where  $\bar{\varphi}_{mom}$  is the volumetric  $\bar{\Phi}_{mom}$  per cell,  $\bar{F}_{other}$  are some additional forces due to the submicron droplets, such as the pressure gradient, Saffman lift, which can be added according to the conditions.

## 5.2.5 Temperature Dependent Properties

Due to the complex thermal process of the flashing phenomenon, some first-order phase transitions (e.g. vaporization, boiling, condensation and even solidification) can occur. Therefore, the temperature dependent physical and transport properties of the test fluids should be taken into account. Fig. 5.3 illustrates some properties of the studied fluid (saturation properties of the liquid phase and isobaric properties of gas phase). The data are from the NIST database [131]. Since the properties of the continuous and disperse phases are highly temperature dependent, in the simulation, they are implemented with polynomial fitting of the NIST data.

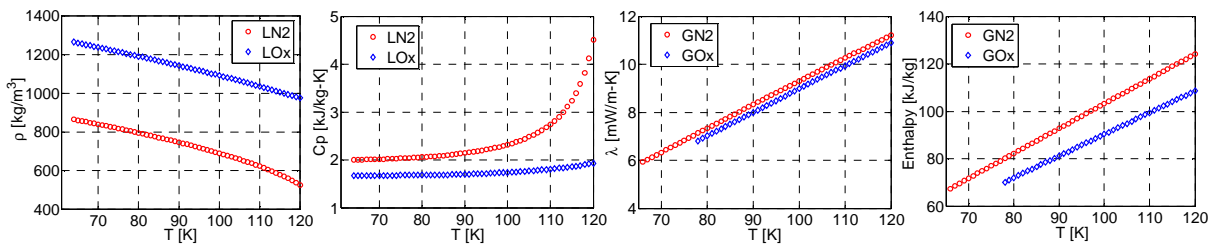


Fig. 5.3 Several properties of the simulated fluids

With the above discussion, the simulation model for the flashing spray is thus developed, namely Flashing Spray Model (FSM). This model will be implemented into the CFD solver to perform a numerical investigation of the cryogenic flashing sprays.

## 5.3 Simulation Procedure

### 5.3.1 Simulation Setup

The numerical simulation of the present work is performed with the CFD software package ANSYS FLUENT<sup>®</sup> 17.2, and the computed mesh grid is generated by ICEM<sup>®</sup> 17.2. The Euler-Lagrange approach is employed for the flashing two-phase flow simulation. The continuous phase is calculated under the Euler frame by solving the 3-D unsteady Reynolds-Averaged Navier-Stokes (U-RANS) equations with the pressure-based solver. The dispersed phase is tracked in the Lagrangian frame with Newton's second law. For the continuous phase, the two-equation  $k$ - $\epsilon$  turbulence model is chosen for its robustness, and the standard wall function is applied to the near-wall treatment. The PISO pressure correlation method is employed for pressure-velocity coupling. The discretization of the governing equation is performed with the 2<sup>nd</sup> order upwind scheme in space and with the 1<sup>st</sup> order implicit scheme in time. The interaction between the two phases is coupled by mass, momentum and energy exchange. Due to the coupling calculation, the turbulent dispersion is important to the DPM simulation, which will enhance the computation stability by smoothing the source terms and by eliminating the local spikes in coupling to

## 5. Modeling of Cryogenic Flashing Spray

the continuous phase. In this study, the effect of turbulent fluctuation on the particle dispersion is modeled using the stochastic tracking (discrete random walk).

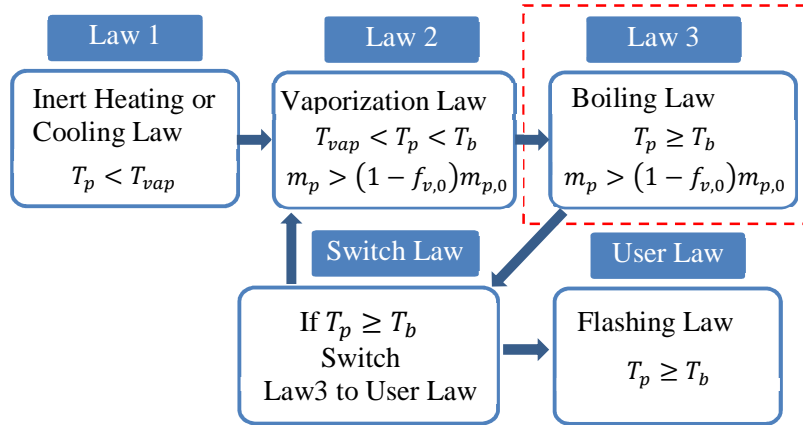


Fig. 5.4 Flowchart of the simulation laws

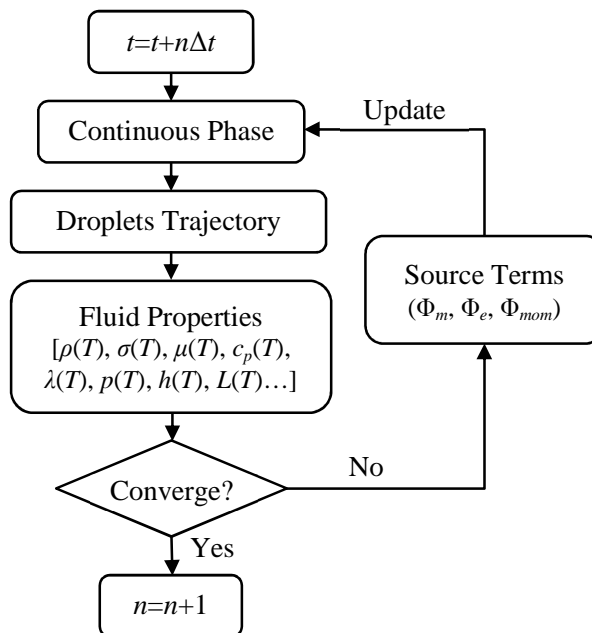


Fig. 5.5 Flowchart of unsteady simulation per time step

As the ANSYS solver still lacks a proper flashing model, a developed code with several User Defined Functions (UDFs) is supplemented to the solver to perform the present study. This code is to specifically

describe the Flashing Spray Model (FSM) developed in the previous sections. In summary, a superheated droplet model has been implemented to calculate the heat, momentum and mass source terms. A developed flash boiling law and a modified spray drag law are implemented to describe the flashing evaporation and droplet trajectory. Due to the low pressure and low temperature conditions, the physical and transport properties of the fluids are highly temperature dependent. They are handled with polynomial interpolation data from the NIST database. During computation, the simulation will switch from the flashing evaporation to the default well-known  $D^2$  law once the fluid' superheat decreases below zero. The flow chart of the simulation model is illustrated in Fig. 5.4, and the simulation process per time step is described in Fig. 5.5.

### 5.3.2 Computational Mesh and Boundary Conditions

The Euler-Lagrange approach is applicable to a flow with both the continuous phase and the discrete phase. Fig. 5.6 shows the computational domain, mesh and boundary conditions.

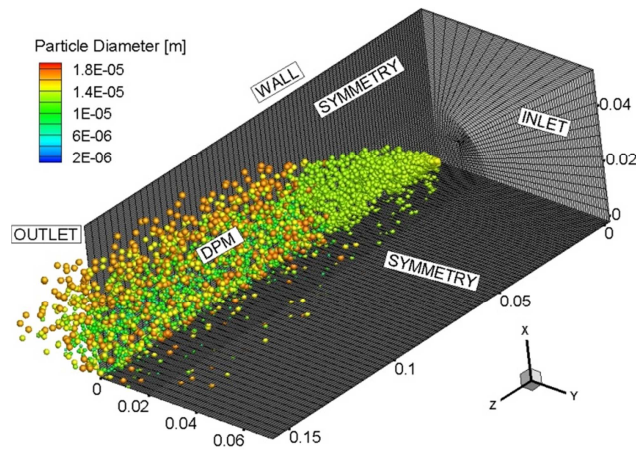


Fig. 5.6 Computational domain, mesh and boundary conditions

Eulerian phase boundary conditions: a constant velocity is prescribed as the inlet boundary condition. Non-slip adiabatic boundary conditions are applied at the chamber wall. At the exit of the chamber, the outlet pressure condition is adopted with the test-measured value. In order to save the computational cost, a quarter of the chamber size (110mm×144mm×160mm) is adopted for the computational domain, and the corresponding symmetry boundary condition is used.

Lagrangian phase boundary conditions: a solid-cone injection is employed as the droplet release type conditions. The injection mass flow rate, velocity and the initial spray cone-angle are prescribed using the test data. Because of the typical feature of flashing spray, e.g., the flash boiling dominated atomization and rather fine droplets size, in this paper, the droplet aerodynamic breakup and droplet collisions are ignored. Due to the complex phase change of the flashing atomization, a quantitative measurement of the initial droplet size distribution is rather difficult, and no such data of the typical cryogenic fluids is available. Hervieu and Veneau [41] measured the liquid propane droplet size and

pointed out that the typical droplet Arithmetic Mean Diameter ( $D_{10}$ ) falls in a range of 10 $\mu\text{m}$  to about 50 $\mu\text{m}$  under the flashing condition. Cleary et al. [23] proposed a transitional model of the flashing atomization and reported that at the beginning of the fully flashing regime, the droplet Sauter Mean Diameter ( $D_{32}$ ) is around 65 $\mu\text{m}$  or less. Lamanna et al. [49] claimed that, for the fully flashing sprays, the enhanced evaporation induces a narrow Rosin-Rammler distribution with  $D_{32}$  statistically less than about 25 $\mu\text{m}$ . In the present work, the initial droplet size is prescribed as the narrow Rosin-Rammler cumulative distribution with the  $D_{32}$  of below 25 $\mu\text{m}$ . The cumulative distribution function is

$$Q(d) = 1 - \exp\left[-\left(\frac{d}{d_{mean}}\right)^n\right] \quad (5.29)$$

where  $d_{mean}$  is the mean diameter and  $n$  is the distribution shape parameter.

### 5.3.3 Spatial and Temporal Resolution Validation

For the unsteady simulation, it is essential to achieve the independency of both spatial and temporal resolution. Traditionally in CFD simulation, the temporal resolution is determined by the stability requirement of the continuous phase, such as the well-known CFL criterion, as shown in Eq. (5.30). For DPM simulation, it is necessary that the particle travels a distance of mere fraction of the cell length in one time step [132]. This will guarantee several iterations of update on the mass, momentum and energy sources within the current cell per time step. Furthermore, the time step is relative to the computational expense and a small time step results in excessive computational cost. The spatial resolution affects the computational accuracy, and fine mesh reduces the spatial discretization error under the same discretization scheme, whereas it inevitably leads to large computational time. Consequently, a proper mesh size with the corresponding time step should be estimated with consideration of stability, accuracy and efficiency.

$$CFL = \sum_{i=1}^3 \frac{u_i \Delta t}{\Delta x_i} \leq 1 \quad (5.30)$$

A sensitive study has been performed to evaluate the accuracy and efficiency trade-offs. In the test, the droplet velocity is in the magnitude of several tens of meters per second with consideration of the expansion. Therefore, the time step or mesh size is generally estimated at  $\Delta t < 0.1 \min(\Delta x_i)$ .

Abraham [133] conducted a mesh resolution investigation in order to reproduce an accurate spray structure and found that the mesh near the injector should be at least in the same magnitude as the injector diameter. This criterion, however, is normally unrealistic for the industrial-scale application, where the accuracy has to be compromised on efficiency. Wang et al. [134] showed that in a typical optimization mesh study, by employing the KIVA code and detailed chemistry mechanism, the near-injector mesh can be as large as 17 times of the injector diameter. In our investigation, the minimum

mesh size is chosen after a sensitivity study, in the order of sub millimeters (the same order as the injector diameter). Then the corresponding time step is chosen with an order of magnitude of around  $-5$ .

Fig. 5.7 and Fig. 5.8 show the grid and time step sensitivity studies. In Fig. 5.7, three different mesh density numbers are studied with the fixed time step. The temperatures along the spray centerline of the gas and the droplets are obtained, and the average temperature is compared with the experimental data. It shows that the grid number about 180,000 (Mesh #2) can reproduce similar results as with mesh elements of about 400,000 (Mesh #3). In Fig. 5.8, four different time steps are studied under the same mesh condition. The simulation results demonstrate that a time step of  $1 \times 10^{-5}$ s is sufficient for the present simulation with Mesh#2.

In summary, with consideration of the computational stability, accuracy and efficiency, the fluid time step of  $1 \times 10^{-5}$ s with the mesh number of about 180,000 (No.#2c) is chosen for the CFD investigation of the flashing spray.

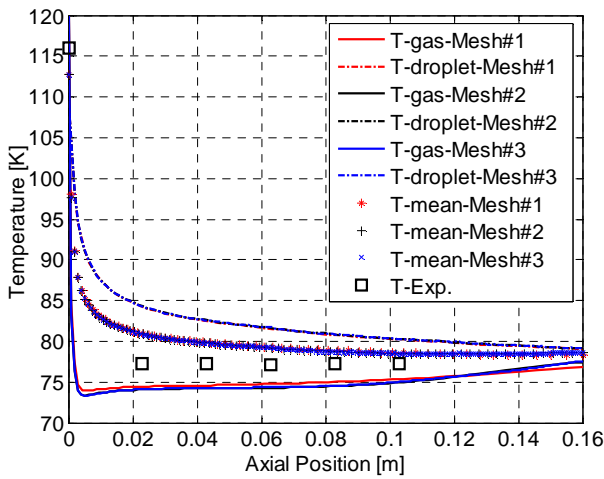


Fig. 5.7 Mesh sensitivity study

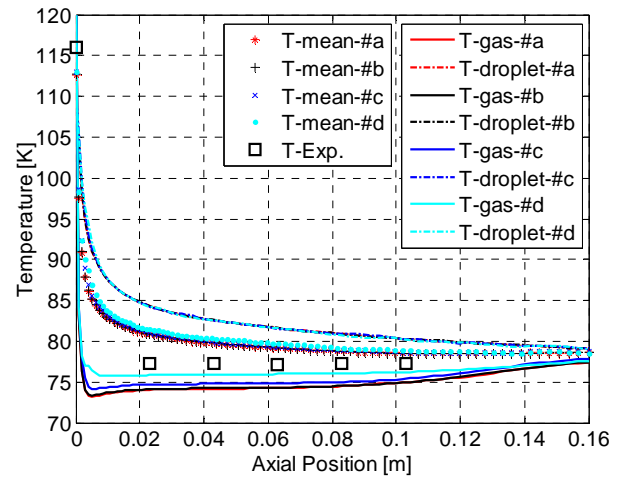


Fig. 5.8 Time sensitivity study

Tab. 5.1 Mesh size and time step sensitivity study

No.	Mesh Size	Time Step
#1	$7.5 \times 10^4$	$1 \times 10^{-5}$ s
#2	$1.8 \times 10^5$	a. $1 \times 10^{-4}$ s
		b. $5 \times 10^{-4}$ s
		c. $1 \times 10^{-5}$ s
		d. $5 \times 10^{-6}$ s
#3	$4.0 \times 10^5$	$1 \times 10^{-5}$ s

## 5.4 Results and Discussions

The temperature profile and the spray shape obtained from the 3D simulation are analyzed and validated by the experimental data of the LN<sub>2</sub> and LOx flashing sprays. Tab. 5.2 lists the simulated boundary conditions.

Tab. 5.2 Simulation cases

Cases	Fluids	$T_{inj}$ (K)	$p_c$ (bar)	spray half cone angle (°)	$v_p$ (m/s)	$\dot{m}$ (g/s)	$D$ (Rosin-Rammler)			
							$d_{max}$	$d_{min}$	$d_{mean}$	$n$
#1	LOx	111	0.210	85°	47	9.5	12	8	10	5
#2	LN <sub>2</sub>	101	0.104	44°	44	6.0	18	10	14	5
#3	LN <sub>2</sub>	97	0.150	42°	44	6.1	20	10	14	5
#4	LOx	116	0.206	45°	38	7.5	18	10	14	5

Typically, to track all the discrete particles in the DPM method is heavily time-consuming, since the cost is proportional to the square of total number of droplets. In order to save computational cost, Dukowicz [135] proposed a particle-fluid approach, in which droplets of similar properties are grouped into “parcels” and the spray is then solved statistically. In this work, the standard parcel method is used. The transient flashing spray is simulated in a time period of about 6ms, and about  $4 \times 10^5$  parcels with the total droplets number about  $2 \times 10^7$  are tracked. Fig. 5.9 shows the tracked spray droplets. A typical bell-shaped fully flashing spray is well reproduced.

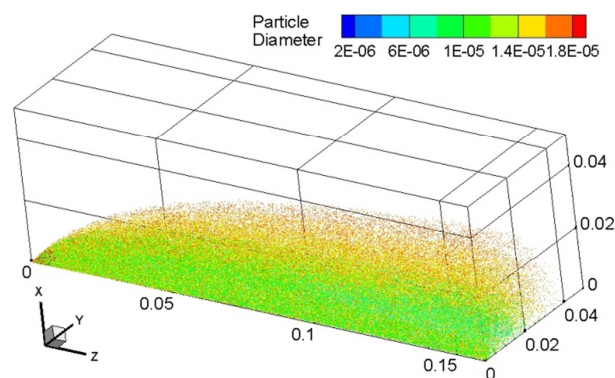


Fig. 5.9 Simulated spray shape under flashing conditions

### 5.4.1 Spray Morphological Characteristics

Literature studies show that the macroscopic morphology study is important to characterize a spray. In this section, the simulated spray morphology is analysed and compared with the experimental results.

Fig. 5.10 and Fig. 5.11 display both the numerical and experimental spray morphology of LOx and LN<sub>2</sub> under flashing conditions. The right half part is the experimental high-speed Schlieren image, and the left half part is the corresponding simulated spray with the same size scale as the test image. From the test picture the typical fully flashing morphology can be clearly seen, i.e. violent atomization and vaporization, bell-shaped spray with a large spray angle (the half spray width is around 26mm, while the injector radius is only 0.25mm). This violent vaporization and large spray angle have been explained in detail in Chapter 3. Under flashing conditions, the liquid cluster molecules with high internal energy will overcome the nucleation barrier (heterogeneous nucleation barrier in most cases), leading to energy favorable for the nuclei formation. The growth of the large number of nuclei favored and resulted in a drastic breakup of the liquid jet, leading to a fast lateral expansion of the spray. In comparison, the spray simulated are fairly comparable with the test images, and the bell-shape profiles are well reproduced. However, the detailed features of the spray turbulent structures shown in the test images were not predicted by the simulation. This is attributed to the URANS method with a large time step used in the simulation. The URANS method intrinsically averages the turbulence feature within a characteristic time  $\tau$ . Therefore, the method is only applicable to capture the “ensemble averaged” variables with a time scale larger than  $\tau$ , and fails to describe the detailed turbulence information with a time scale less than  $\tau$  [136]. However, all in all, the simulation succeeds to reportray the macroscopical morphology of the flashing spray.

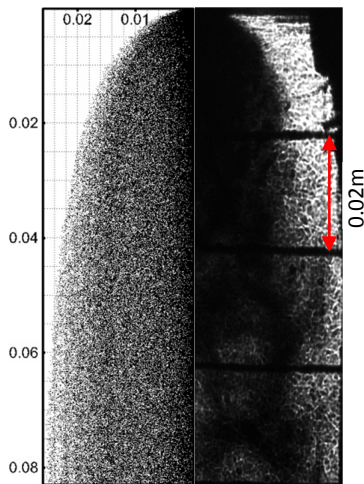


Fig. 5.10 LOx spray contour

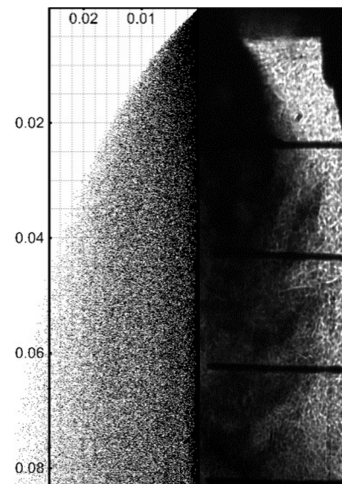
Fig. 5.11 LN<sub>2</sub> spray contour

Fig. 5.12 presents the temporal evolution of the Lagrangian trajectory of the LN<sub>2</sub> spray droplets, which is colored and sized by the droplet size magnification. The displayed droplet density number is reduced for better visualization. The figures generally show that the spray droplets experience a strong size reduction due to the intensive evaporation once injected before they eventually approach a uniform small size distribution downstream the injector. In specific, at the time  $t=0.75\text{ms}$ , a group of large droplets are released, only after about  $0.5\text{ms}$ , these droplets travel about  $30\text{mm}$  and reduce much of their sizes. Afterwards, the spray show a small change of the particle size (see the color). The figures show that much of the small droplets are concentrated near the spray axis and some large droplets move radially

## 5. Modeling of Cryogenic Flashing Spray

outwards. This distribution is mainly attributed to the interaction between the droplet and their surrounding gas phase, which will be discussed in Sec. 5.45 in detail.

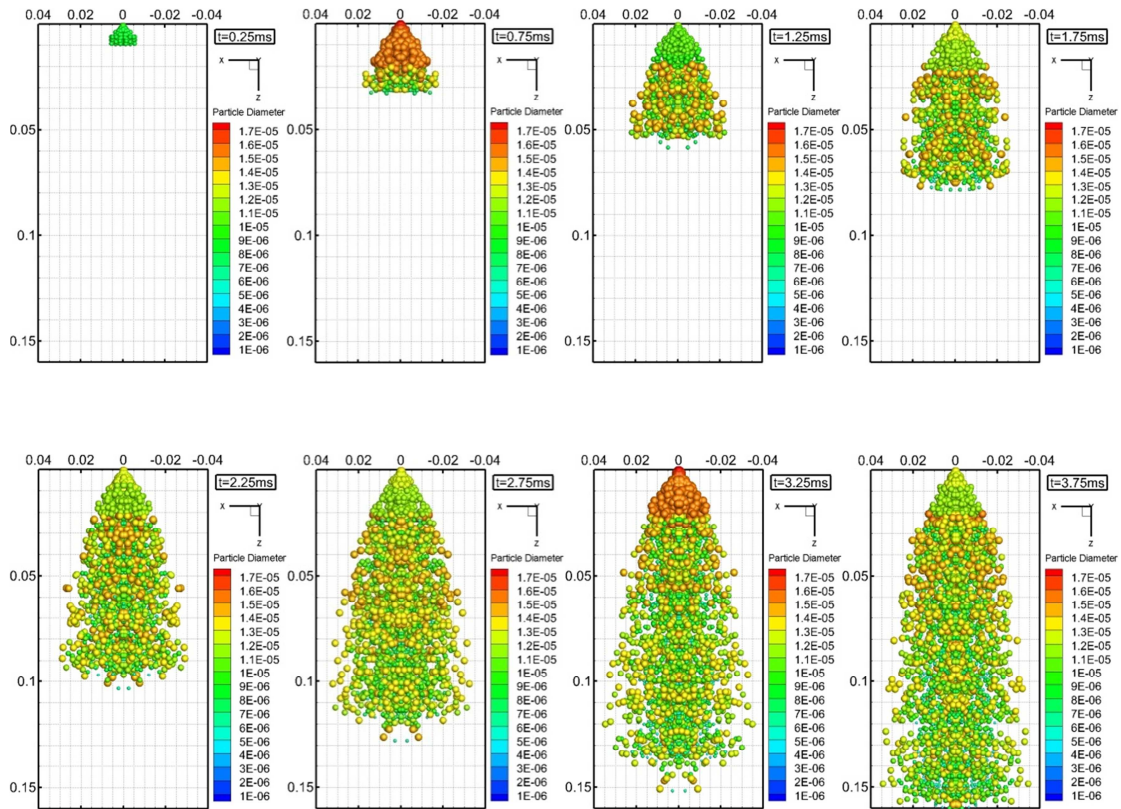


Fig. 5.12 Time evolution of LN<sub>2</sub> flashing spray

### 5.4.2 Temperature Characteristics

Fig. 5.13 and Fig. 5.14 illustrate the temperature profiles of the LOx and LN<sub>2</sub> spray along the spray centerline. In the experiment, five thermocouples are located along the spray centerline to record the local temperature. The first thermocouple is located about 23mm downstream of the injector orifice, and the others follow with a same distance interval of 20mm. Due to the multiphase characteristic of the spray, the measured temperature is assumed to be the equilibrium temperature of the local droplets ensemble and the surrounding vapor. This equilibrium temperature can be estimated with a weighted average temperature by the one-third rule, shown in Eq. (5.11). The star curves in both figures show that the weighted average results of the simulated temperature matches well with the experimentally measured temperature. In the vicinity of the injector orifice, both the droplets and the gas experience a drastic temperature drop, but the gas temperature decreases faster than the fluid droplets due to its smaller heat capacity. Specifically, taking the LOx case as an example, the temperature of the spray droplets decreases from 111K to about 84K, mere 7K above the saturation temperature ( $T_{sat}=77.4K$  @

0.21bar), and loses about 80% of its total superheat before the spray just travels about 20mm~30mm downstream of the injector orifice. This dramatic temperature decrease in a short distance implies a violent evaporation triggered by the flashing in this region. Lamanna et al. [49] reported a comparable case, in which within a short distance (about 20mm) the superheated acetone releases most of its latent heat after injection.

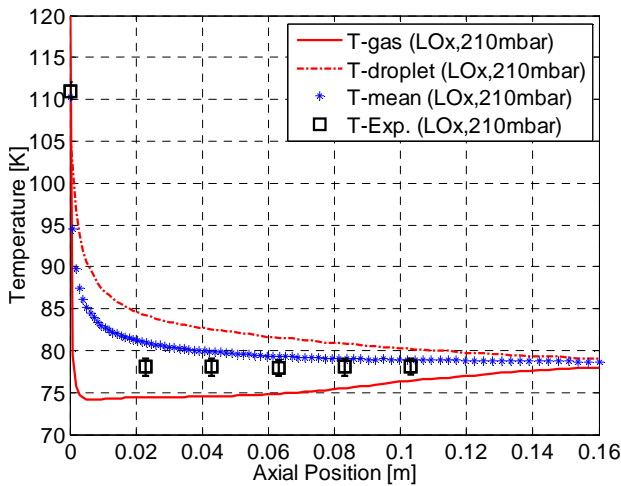


Fig. 5.13 LO<sub>x</sub> temperature distribution along the spray centerline

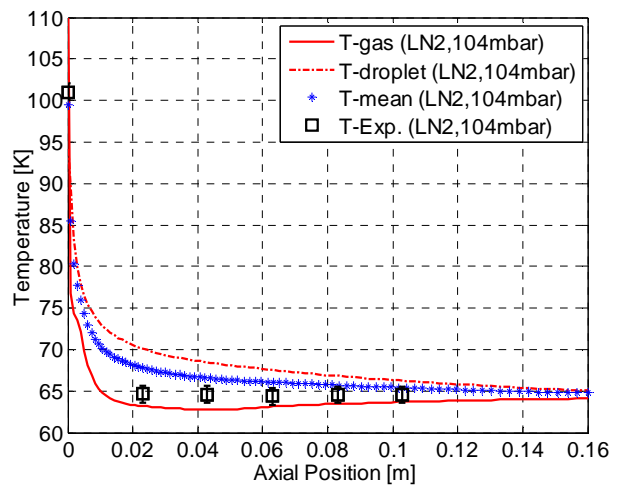


Fig. 5.14 LN<sub>2</sub> temperature distribution along the spray centerline

It can also be seen that the droplet temperature decreases monotonically along the spray axis, whereas the vapor decreases immediately to a low temperature in the beginning and then slightly increases downstream of the spray. From the perspective of heat exchange, under the flashing conditions the temperature decrease of both phases can be easily understood. When a droplet travels in the local computational cell, it will exchange mass with its surrounding gas. The mass evaporation due to flashing contributes to the droplet temperature change, and the mass evaporation by heat conduction and convection and radiation contributes to the energy balance of the surrounding gas. Since evaporation is an endothermic process, it makes the spray and the local gas cool down. Downstream of the spray, as warmer ambient gas is entrained inside the jet, the enhanced heat transfer results in an increase in the gas temperature.

To compare Fig. 5.13 and Fig. 5.14, we can find that in the very beginning, the temperature of oxygen gas is decreasing much faster than that of nitrogen gas. This is attributed to the difference of the specific heat capacity and specific latent heat between them, since the heat capacity of oxygen is smaller than that of nitrogen ( $c_{p-LN_2}=2.0$  kJ/kg/K and  $c_{p-LOx}=1.7$  kJ/kg/K), while its latent heat is a little larger ( $L_{LN_2}=199$  kJ/kg and  $L_{LOx}=213$  kJ/kg). This leads to the oxygen temperature decreasing faster when the same amount of mass is evaporated from the droplets.

Remarkably, near the injector orifice the gas temperature decreases rapidly below the saturation temperature. It can be expected that such a large gas temperature drop might lead to a local

## 5. Modeling of Cryogenic Flashing Spray

condensation. Such low temperatures of the spray was also obtained by Aguilar et al. [137], Yildiz [44] and Vu et al. [45] in the R134a spray studies. The dramatic temperature drop below the saturation temperature or even the triple point temperature might cause local spray condensation or even solidification. Actually, solid deposition of nitrogen and methane has been observed in our previous experiment (see Chapter 3) when the chamber pressure was below the triple point pressure (126mbar for nitrogen and 117mbar for methane).

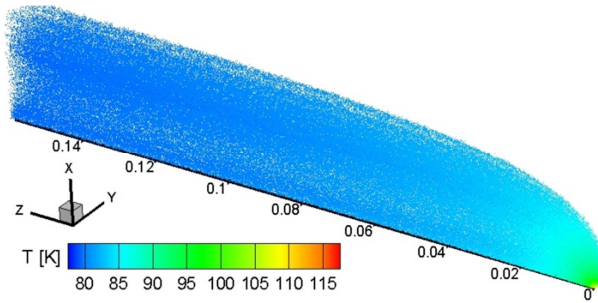


Fig. 5.15 Temperature contour of LOx droplets

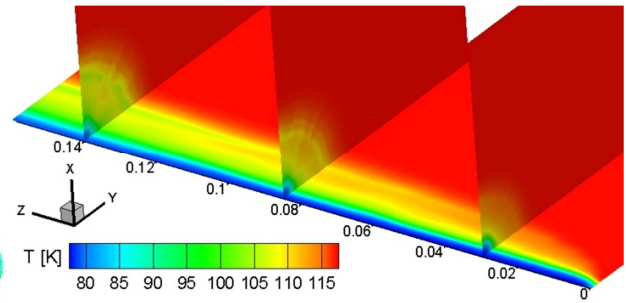


Fig. 5.16 Temperature contour of oxygen gas

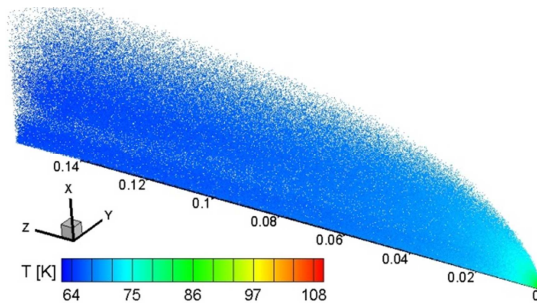


Fig. 5.17 Temperature contour of LN<sub>2</sub> droplets

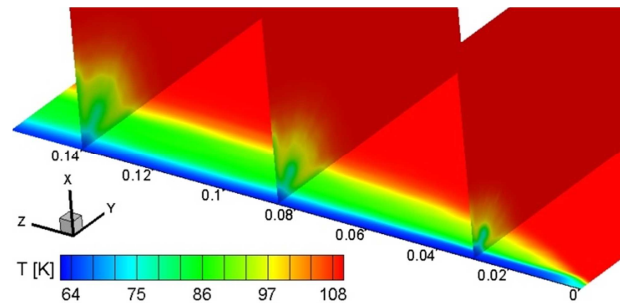


Fig. 5.18 Temperature contour of nitrogen gas

Fig. 5.15 and Fig. 5.17 describe the temperature contour of tracked LOx droplets and LN<sub>2</sub> droplets, respectively. It can be seen that the spray droplet temperature distribution is quite uniform in the radial direction of the spray. In the axial direction the temperature decreases monotonically from the initial temperature to the near saturation temperature. Fig. 5.16 and Fig. 5.18 show the temperature contours of surrounding oxygen gas and nitrogen gas at the symmetry plane of the simulation domain. It shows that the spray temperature is lower in the spray center and increases slightly in the axial direction. In the radial direction, the temperature increases due to the heat transfer from the warmer ambient gas.

As discussed before, along the spray centerline, the spray temperature is decreasing and downstream of the injector, the temperature has an increasing trend. We attribute this temperature distribution to the gradual weakening of the flashing evaporation and the strengthening of the heat transfer from the surrounding gas. Fig. 5.19 plots the distribution of the evaporation mass flow rates along the spray axis. The symbol curves are obtained by tracking the droplets in one iteration at a simulation time of 5.5ms,

and the symbols represents the tracked droplets (the number density is reduced for a better visualization). It shows that, initially, the spray experiences a violent flashing evaporation with the evaporation mass flow rate in the order of  $10^{-9}$ , and just after a rather short distance ( $<10\text{mm}$ ), this evaporation rate drops to about  $10^{-10}$ . Yet the evaporation mass flow rate due to conduction and convection is just in the order of  $10^{-12} \sim 10^{-11}$ , almost 2 orders of magnitude smaller than that by flashing. Because of the low ambient temperature, the evaporation mass flow rate caused by radiative heat transfer is even smaller, with a value in the order of  $10^{-13}$ . This demonstrates that the heat transfer by flashing overwhelmingly dominates the spray vaporization in the near-injector field. The high flashing evaporation mass flow rate is the reason of the initial drastic temperature drop, as shown in Fig. 5.13 and Fig. 5.14 (see the beginning of the temperature curve). As the droplet travels downstream, the superheat degree decreases and weakens the flashing evaporation. On the contrary, the high speed spray enhances the external heat transfer from the surrounding gas. At a short distance ( $\sim <20\text{mm}$ ), the evaporation caused by the external heat transfer balances the flashing evaporation, which still has a larger value than that of the radiation contribution (see Fig. 5.19). The total evaporation mass flow rate at this point is in the order of  $10^{-10}$  (one order of magnitude smaller than the initial value). The temperature decrease is slowed down, as a consequence. The temperature decrease is, as a consequence, slowed down. Downstream of the spray, as a result of the surrounding gas entrainment, the heat transferred from the surroundings surpasses the flashing evaporation by about 1 or 2 orders of magnitude. Considering the stronger conductive and convective heat transfer in this region, the external heat transfer shows a dominant role in the spray evaporation. This leads to an increase in the gas temperature downstream of the spray, as shown in Fig. 5.13 and Fig. 5.14.

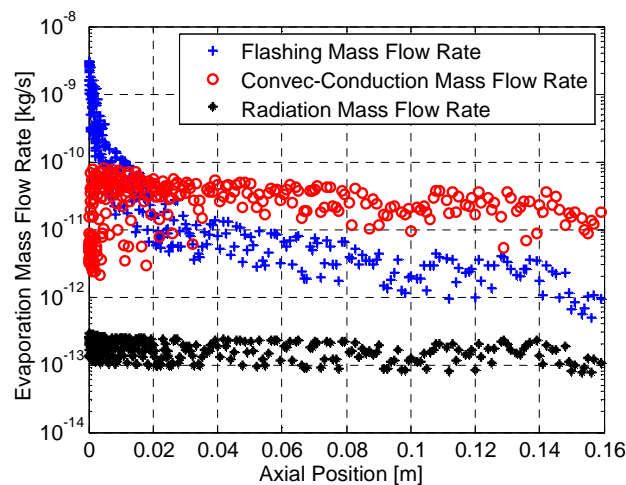


Fig. 5.19 Statistical results of evaporation mass flow rate of LOx spray

### 5.4.3 Velocity Characteristics

Fig. 5.20 and Fig. 5.22 respectively show the droplets and the gas velocity of the LOx and LN<sub>2</sub> spray along the spray centerline. The blue curve is the velocity profile of droplets and the red curve refers to

## 5. Modeling of Cryogenic Flashing Spray

the velocity profile of the gas phase. The marked point 1, point 2 and point 3 are the locations of the detected pressure, which will be explained later in Fig. 5.26 and Fig. 5.27.

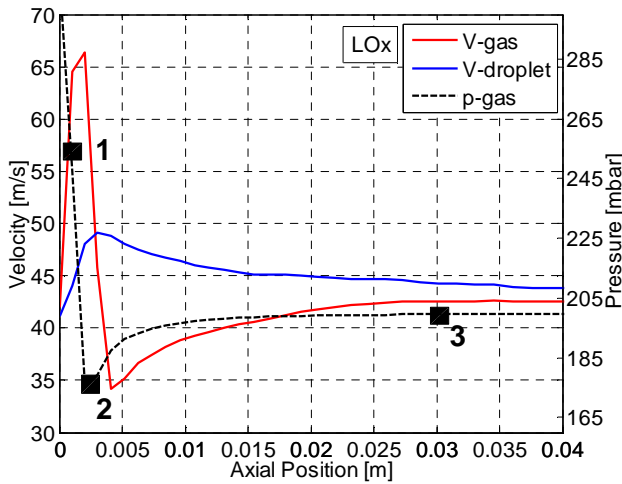


Fig. 5.20 LOx spray velocity in the spray axial direction

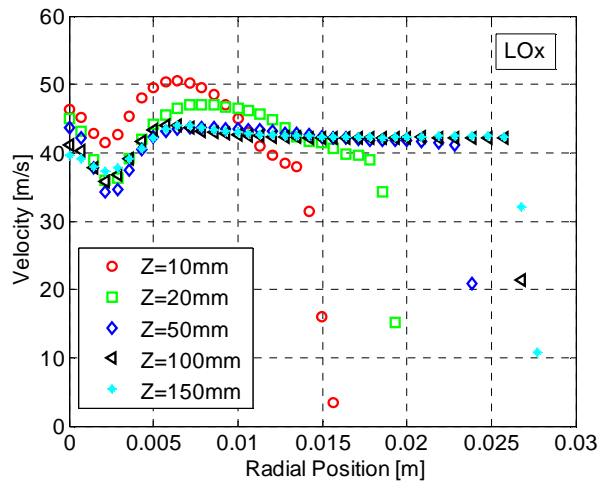


Fig. 5.21 LOx droplet velocity in the spray radial direction

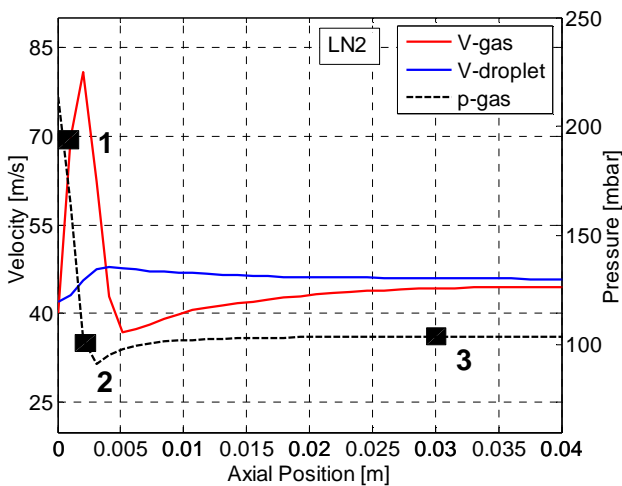


Fig. 5.22 LN<sub>2</sub> spray velocity in the spray axial direction

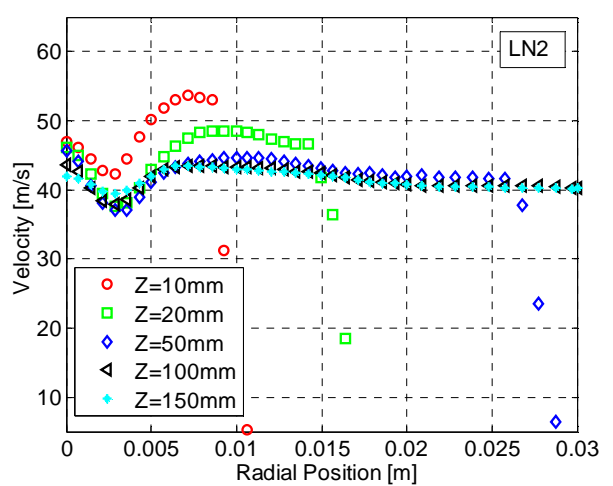


Fig. 5.23 LN<sub>2</sub> droplet velocity in the spray radial direction

At the injector orifice, the discrete phase and the continuous phase show a similar initial velocity. After injection the velocity of both phases increases in magnitude: the gas phase peaks at a velocity that almost doubles the initial velocity, and the droplets accelerate by almost 20% near the injector orifice. The large acceleration of both phases is due to the fluid expansion that is caused by the violent flashing evaporation. Afterwards, the droplet velocity decreases slightly, while the gas velocity experiences a drastic decrease. As a consequence of the momentum exchange of two phases, the gas velocity starts to

increase slightly, before it finally achieves a similar velocity to the droplets. This velocity profile agrees with the description of the typical velocity feature of the flashing spray, called “expansion-entrainment” region by Polanco et al. [90]. The droplet velocity profile is also comparable to the experimental data measured by Vu et al. [45] and Yildiz [44] in the R134A flashing study. Due to a rapid velocity increase near the injector orifice, the static pressure decreases dramatically. Following the rapid evaporation, the static pressure recovers and establishes a constant value within a short distance, as shown by the dash curves in the figures.

The droplet velocity distribution in the spray radial direction is plotted in Fig. 5.21 and Fig. 5.23. The velocity profiles show self-similarity, and two extremum points of the velocity appear. To be specific, in the radial direction, the gas velocity decreases and then increases to its maximum point, before it is followed by a decreasing trend. This behavior differs from the well-known Gaussian velocity distribution. It might be ascribed to the droplets’ evaporation and interaction with the gas phase. It can also be seen that the velocity profiles show more uniformity downstream of the spray. Further downstream of the spray (e.g. at “Z=150”) the velocity has a deviation of around 10%.

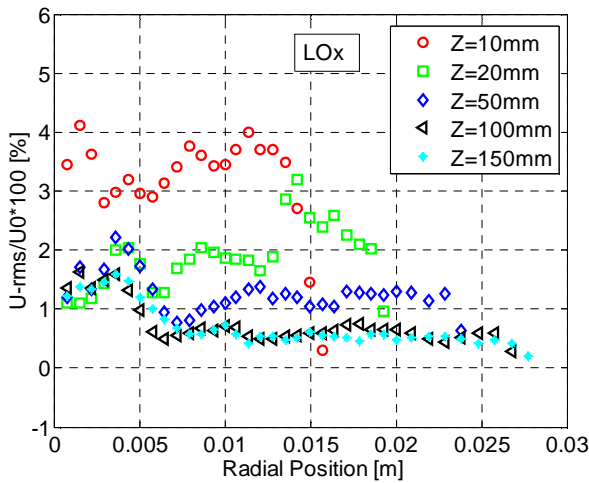


Fig. 5.24 Velocity fluctuation in the spray radial direction of LOx spray

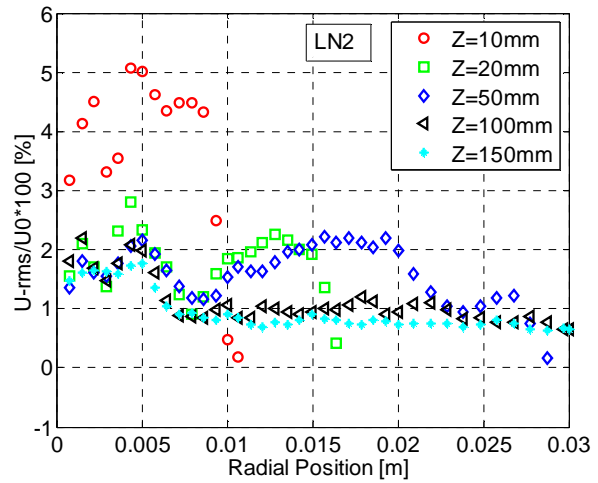


Fig. 5.25 Velocity fluctuation in the spray radial direction of LN<sub>2</sub> spray

Fig. 5.24 and Fig. 5.25 present the distributions of the normalized droplet velocity Root Mean Square (RMS) of the LOx and LN<sub>2</sub> sprays, respectively. The velocity RMS defined in Eq. (5.31) provides information on the turbulence characteristics of the flow field.

$$U_{rms} = \sqrt{\frac{u'_x u'_x + u'_y u'_y + u'_z u'_z}{3}} \quad (5.31)$$

The profiles present off-axis peaks, indicative of the shear layer developed there between the spray jet and the surrounding vapor. A large difference in the velocity RMS distribution can be seen between the

near-field spray and downstream-field spray. The velocity RMS profiles around the injector orifice commonly have larger values (with the peak values almost doubled by those downstream of the spray) and have three peaks, with one closer to the spray axis and the others closer to the outer spray. It also shows that the profiles in the near-field spray region have a large oscillation, with the velocity RMS variation at around 32%. However, as the spray develops downstream, the velocity RMS profiles turn out to be uniform far away from the spray centerline and have one distinct peak near the centerline. These features imply a strong turbulence in the near-field spray, and they are supposed to be mainly caused by the violent flashing vaporization.

### 5.4.4 Pressure Oscillation

Fig. 5.26 and Fig. 5.27 illustrate the pressure evolution at three different locations, i.e. point 1 (“ $Z=1\text{mm}$ ”), point 2 (“ $Z=2\text{mm}$ ”) and 3 (“ $Z=30\text{mm}$ ”) for LOx and LN<sub>2</sub> cases, respectively. Point 1 is located within a region where the static pressure is decreasing, point 2 near the minimum pressure point and point 3 at a stable pressure, as marked in Fig. 5.20 and Fig. 5.22. From the Fig. 5.26 and Fig. 5.27, we can find that the pressure fluctuates with a high frequency (see the enlarged subfigures) at point 1 and point 2, while the oscillating frequency is much lower downstream of the spray at point 3. The high-frequency pressure oscillation near the injector orifice implies complex fluid structures in this region. The fluid structures here can be considered from two points. One is induced by the violent phase change by the flashing evaporation. The violent phase change enhances the mass and momentum exchange between the discrete phase and the continuous phase, and induces the high frequency pressure fluctuation. The other reason might be the injection process itself. In the Euler-Lagrange approach, the discrete phase is injected to the continuous phase at every specified time step. This injection itself will introduce a specific frequency and affect the spray. Actually, the pressure oscillation due to the flashing evaporation was observed by Frost [138] in the investigation of a single droplet behavior under flashing conditions. The author attributed the pressure fluctuation to the bubble surface instability caused by bubble collapse and oscillation.

In this case, we are inclined to attribute the pressure oscillation to the flashing atomization and evaporation. Since the flash boiling occurs principally in the near-injector region, the explosive boiling of numerous droplets disturbs the environment in neighborhood, leading to the high-frequency pressure fluctuations. At downstream, e.g. point 3, as the superheat of liquid droplets is mostly consumed, the boiling-induced pressure oscillation becomes weak and accordingly causes a decaying fluctuation, as shown by the red curves in the figures.

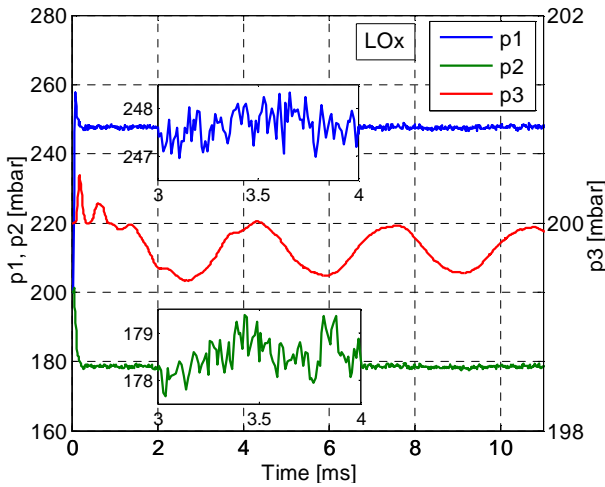
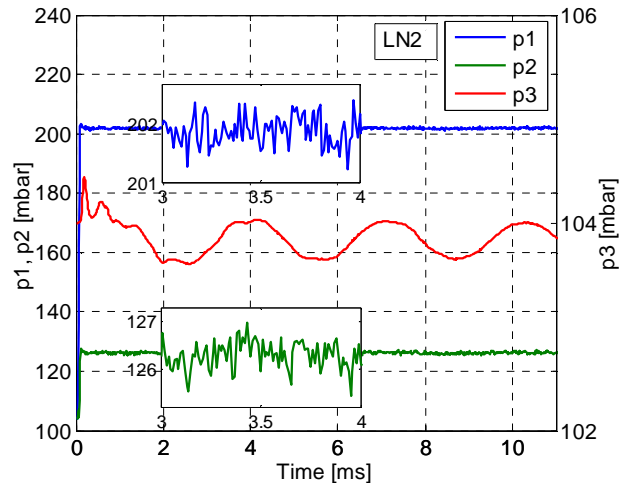


Fig. 5.26 LOx pressure evolution at different locations


 Fig. 5.27 LN<sub>2</sub> pressure evolution at different locations

### 5.4.5 Droplet Size Probability Distribution

The droplet size is a critical parameter for a spray, which is typically described by the Sauter Mean Diameter ( $D_{32}$ ), defined as

$$D_{32} = \frac{\sum N_i d_i^3}{\sum N_i d_i^2} \quad (5.32)$$

where  $d_i$  is the droplet diameter and  $N_i$  is the number of the sampled droplets.

Fig. 5.28 and Fig. 5.30 give the LOx and LN<sub>2</sub> droplet size distribution along the spray centerline. In the figures, the circular points are a snapshot of the droplet distribution at 5.5ms of the transient spray, and the red curve is the statistical average of the droplet diameters from 0ms to 5.5ms. It can be seen that after injection the droplet size of both sprays reduces rapidly under the “flashing law” mentioned in the previous section. Within a short distance of around 30mm, the initial reduction contributes to almost 70% and 80% of the size reduction in total for LOx and LN<sub>2</sub> sprays, respectively. This drastic size reduction is ascribed to the strong evaporation caused by the flashing vaporization in the beginning (with the value in the order of magnitude of -9 as aforementioned). The figure shows that the droplet size reduces as a power function along the spray axial centerline (see the fitted curve in the figure). This relationship is reasonable since the mass evaporation rates and the droplet mass in the developed Flashing Spray Model follow power functions and also the droplet size itself is a power function of the droplet mass. As a result of the initial Rosin-Rammler size distribution, the snapshot of the droplet size distribution in the local Eulerian cell is non-uniform, as shown by an oscillated feature (circular points in the figure).

## 5. Modeling of Cryogenic Flashing Spray

Fig. 5.29 and Fig. 5.31 show the LOx and LN<sub>2</sub> droplet size distribution in the spray radial direction. The CFD results demonstrate that the droplet diameters marginally decrease along in radial direction (with large number density of droplets) followed by an increasing trend far away from the spray center. A similar distribution was obtained by Lasheras et al. [139], Munnannur and Reitz [132] and Raju [76] with the experiment and simulation investigation of two-phase spray atomization. This kind of distribution can be understood as follows. Due to the small momentum force, the small droplets will be much affected by the surrounding gas. They are concentrated and following with the high velocity gas near the spray center. On the contrary, the large droplets move radially outwards with a little impact from the surrounding gas because of their larger inertial force.

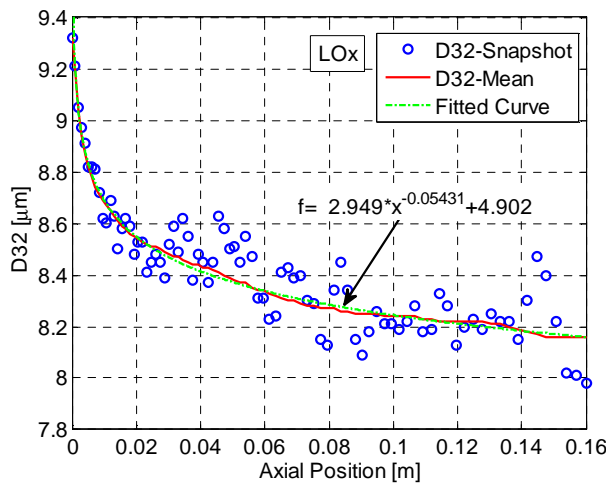


Fig. 5.28 LOx droplet size distribution along the spray centerline

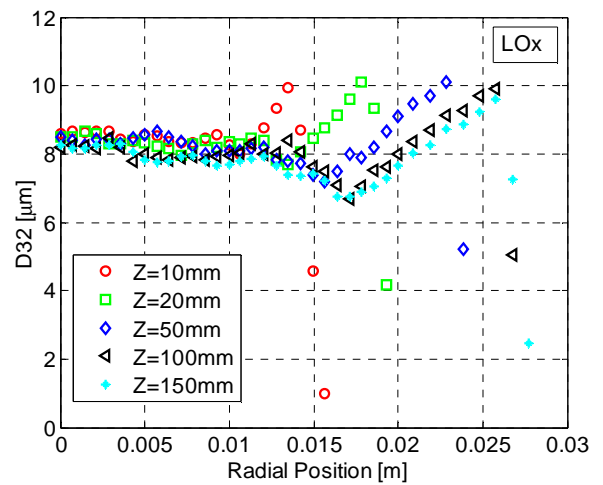


Fig. 5.29 LOx droplet size distribution in the spray radial direction

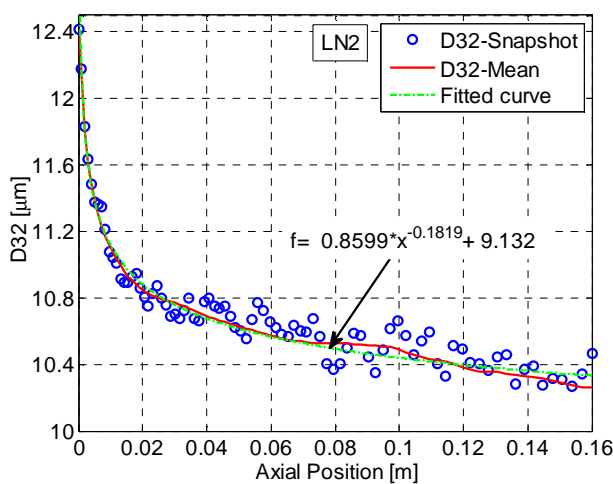


Fig. 5.30 LN<sub>2</sub> droplet size distribution along the spray centerline

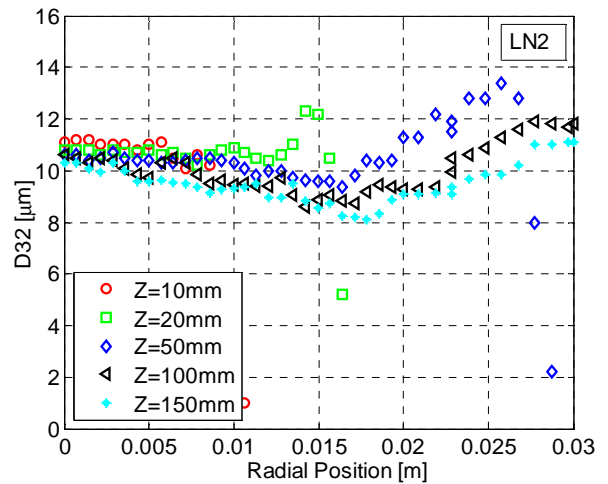


Fig. 5.31 LN<sub>2</sub> droplet size distribution in the spray radial direction

It has to be noted here that the radial distribution of the droplet size appears not to agree well with the experimental results by Yildiz [44] in the flashing spray study. The test results show a monotonically decreasing trend of the  $D_{32}$  in the radial direction. Using the test data by Yildiz, Raju [76] simulated the flashing spray with the DPM method, and the author pointed out that the simulated droplet size results (similar to Fig. 5.29 and Fig. 5.31) is mainly affected by the assumption of the initial droplet size distribution. In an actual spray atomization, the large droplets (or liquid bulk) tend to stay at the spray center and the smaller ones are located peripherally. However, in this simulation, the droplets are point-injected with the assumption of a Rosin-Rammler size distribution but prescribing no specific distribution in the spray radial direction. This boundary condition contains more small droplets in the spray center than the practical situation does. The smaller droplets are then swept downstream towards the spray center and middle, where the gas velocity is higher, while the larger droplets with a high momentum are inclined to move laterally outside the spray.

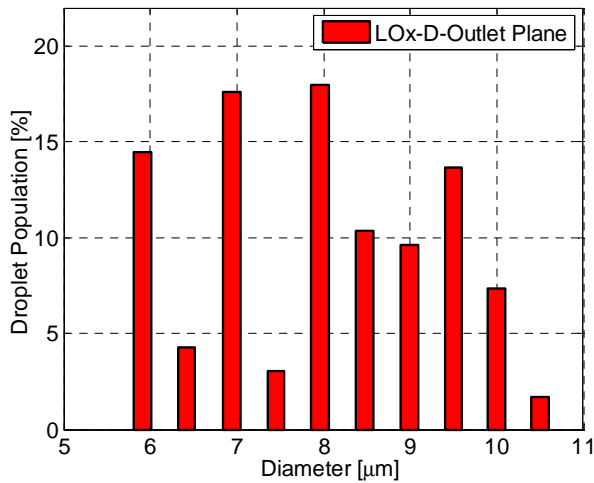


Fig. 5.32 Statistical distribution of LOx droplet size at the outlet plane

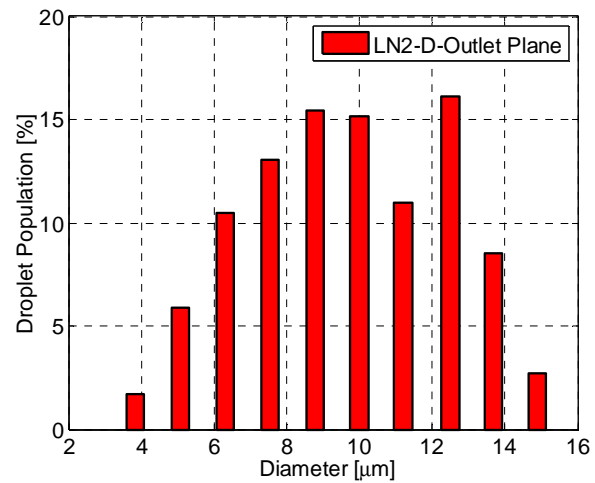


Fig. 5.33 Statistical distribution of LN<sub>2</sub> droplet size at the outlet plane

Fig. 5.32 and Fig. 5.33 describe the statistical droplet size distribution of LOx and LN<sub>2</sub> at the outlet plane of the computational domain, respectively. In total about 2000 parcels at the outlet plane are sampled for data analysis. From both pictures, it can be seen that at the outlet plane the droplets are relatively uniform. This feature is reasonable since the residence time of the droplets in the chamber is short (with a time scale of millisecond) and the droplets with large non-uniform initial size distributions could not have enough time to approach very uniform sizes at the exit of the chamber. As to the LOx spray, the standard deviation of the droplet distribution is around  $1.3 \times 10^{-6}$ . The arithmetic mean droplet size ( $D_{10}$ ) is estimated at  $7.98 \mu\text{m}$  and the Sauter Mean Diameter ( $D_{32}$ ) is determined to be  $8.40 \mu\text{m}$ . As to the LN<sub>2</sub> spray, the standard deviation of the droplet distribution is around  $2.7 \times 10^{-6}$ , and the  $D_{10}$  and  $D_{32}$  are estimated at about  $9.70 \mu\text{m}$  and  $11.07 \mu\text{m}$ .

## 5. Modeling of Cryogenic Flashing Spray

Part of the important simulation results of case #3 and case #4 are also listed for the numerical model validation, as shown in Fig. 5.34 ~ Fig. 5.37. The results display a good agreement between the simulation and experiments. The analyses are similar to the above cases, which, therefore, will not be shown here.

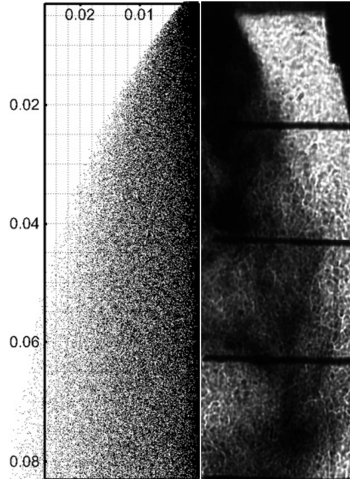


Fig. 5.34 LN<sub>2</sub> spray contour (case #3)

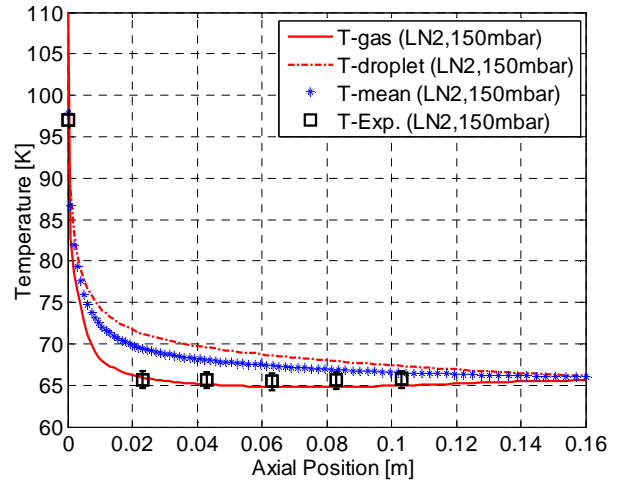


Fig. 5.35 LN<sub>2</sub> temperature distribution along the spray centerline (case #3)

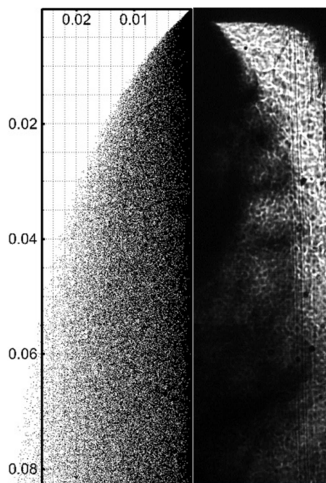


Fig. 5.36 LOx spray contour (case #4)

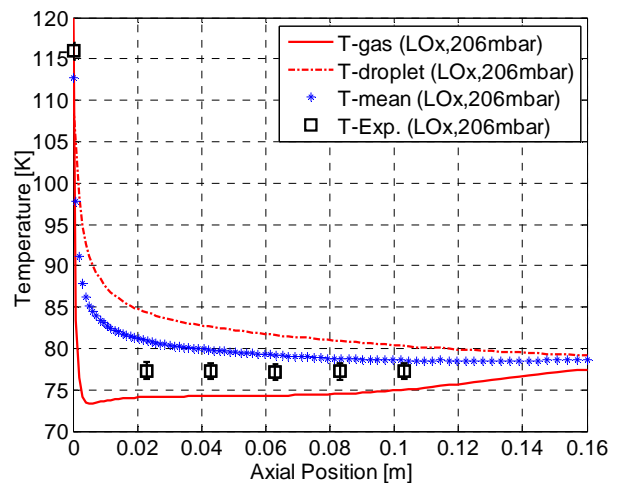


Fig. 5.37 LOx temperature distribution along the spray centerline (case #4)

## 5.5 New Correlation of Flashing Evaporation

From the above discussion, it can be seen that the average temperature of the liquid droplets with the neighboring vapor (assumed in a quasi-equilibrium state) is in good agreement with the test data. The simulated temperature of either droplets or vapor, however, deviates lots from the measured temperature. The deviation is attributed to the superheat evaporation model, i.e. the Adachi-correlation, as shown in Eq. (5.1). This equation is an empirical correlation derived for of pentane ( $C_5H_{12}$ ), which may not suit well the studied cryogenic fluids, considering the big property differences between the two substances. Tab. 5.3 lists the properties of the studied fluids and pentane. In this section, we are trying to figure out a flashing evaporation model by taking into account the fluid properties. Two approaches can be considered to perform this study. One way is to modify the existing Adachi-correlation with due consideration for the specific fluid properties. The other way is to return to the mechanism of flashing and to develop a new model.

Tab. 5.3 Properties of the simulated fluids and pentane (@ 1bar)

Fluids	$T_b$ (K)	$c_p$ (kJ/kg/K)	$L(T_b)$ (kJ/kg)	$\sigma$ (mN/m)	$\mu$ ( $\mu$ Pa-s)	$\rho$ (kg/m <sup>3</sup> )	$\lambda$ (mw/m/K)
LN <sub>2</sub>	77.2	2.0410	199.32	8.9049	161.37	806.59	144.99
LOx	90.1	1.6990	213.18	13.177	195.32	1141.8	150.96
Pentane	308.8	2.3657	357.89	14.282	199.24	610.10	107.41

The common boiling process can help us to understand the physical mechanism of heat transfer in the flash boiling phenomenon. In the normal boiling process, the convection coefficient  $\alpha$  is affected by many factors, such as the superheat  $\Delta T$ , the evaporation latent heat  $L(T_b)$ , the buoyancy force from the density difference,  $g(\rho_l - \rho_g)$ , the surface tension  $\sigma$ , a characteristic length  $L_c$ , and the some other properties of the fluids. This relationship can be expressed as [140]

$$\alpha = \alpha[\Delta T, L(T_b), c_p, \sigma, g(\rho_l - \rho_g), L_c, \lambda, \mu, \rho] \quad (5.33)$$

This multivariable function poses a great challenge to the modification of the Adachi-correlation, although some key factors can just be concerned in the simplification, such as the main driving potential  $\Delta T$ , the factor of indication for the strength of evaporation  $c_p/L(T_b)$  and the molecule surface tension  $\sigma$ . Moreover, Adachi et al. [38] gave the flashing evaporation correlation without any other information for the derivation, which also brings the difficulty to the modification. On this occasion, we resort to a new correlation for the flashing evaporation. Since the flashing evaporation is dominated by the bubble nucleation, the mass evaporation theory related to the nucleate boiling is employed here.

When the spray is at low superheat degree, the flashing evaporation is rather weak. In this regime, the superheat is mere sufficient to support bubble formation, and the heat transfer is principally determined by heat conduction and free convection due to the fluid motion. Therefore, the free convection boiling (e.g.  $\Delta T < 5K$ ) is employed in this regime, as shown [140]:

$$\alpha = 0.15\lambda_l \left[ \frac{g\beta\rho_l^2}{\mu_l^2} \text{Pr}_l \right]^{1/3} (\Delta T)^{1/3} \quad (5.34)$$

In this regime, the conductive heat transfer can be assumed to be in the same order of magnitude as the convective heat transfer. By a sensitivity study, the effective heat transfer coefficient in this regime is estimated about four times of Eq. (5.34).

As the superheat level increases (e.g.  $\Delta T > 5\text{K}$ ), the nucleate boiling becomes important and therefore, in this regime, the well-known Rohsenow-correlation [141] for the nucleation boiling is adopted, as shown:

$$\alpha = \mu_l L(T_b) \left[ \frac{g(\rho_l - \rho_g)}{\sigma} \right]^{1/2} \left( \frac{c_{p,l}}{C_{s,f} L(T_b) \text{Pr}_l^n} \right)^3 (\Delta T)^2 \quad (5.35)$$

To summarize, the correlation of the superheat flashing evaporation is described as below:

$$\alpha'_f = \begin{cases} 0.6\lambda_l \left[ \frac{g\beta\rho_l^2}{\mu_l^2} \text{Pr}_l \right]^{1/3} (\Delta T)^{1/3}, & (0\text{K} \leq \Delta T < 5\text{K}) \\ \mu_l L(T_b) \left[ \frac{g(\rho_l - \rho_g)}{\sigma} \right]^{1/2} \left( \frac{c_{p,l}}{C_{s,f} L(T_b) \text{Pr}_l^n} \right)^3 (\Delta T)^2, & (\Delta T \geq 5\text{K}) \end{cases} \quad (5.36)$$

where  $\beta$  is the thermal expansion coefficient of a liquid at saturation,  $\Delta T$  refers to the liquid superheat degree, and  $g$  represents the gravitational acceleration. All the properties are estimated in the saturation state of the liquid. The constant  $C_{s,f}$  is 0.01, and the exponent  $n$  of the Prandtl number is 1.7 [141].

In this section, Eq. (5.36) is supplemented, as a replacement of the Adachi-correlation, to the developed FSM model. The results will be briefly discussed as follows.

Fig. 5.38 ~ Fig. 5.41 illustrate temperature distribution of the LOx and LN<sub>2</sub> spray, simulated respectively with Adachi-correlation and the new correlation, respectively. It is evident that by the new correlation, the simulated temperature curves of the droplets are more approximate to the measured data than with the Adachi-correlation. As to the gas temperature, both methods give comparable results. To be specific, the droplet temperature decreases much faster at the injector orifice. Along the spray centerline, the droplets lose the latent heat and approximately reach the saturation temperature far downstream of the spray. For the gas phase, the new correlation predicts a steep decrease followed by a slight increase in the temperature. Further downstream of the spray, the gas temperature along the spray centerline is about 4 K higher than the saturation temperature. This gradual increase in the temperature along the centerline is ascribed to the enhancement of the heat convection and conduction from the ambient gas downstream of the spray.

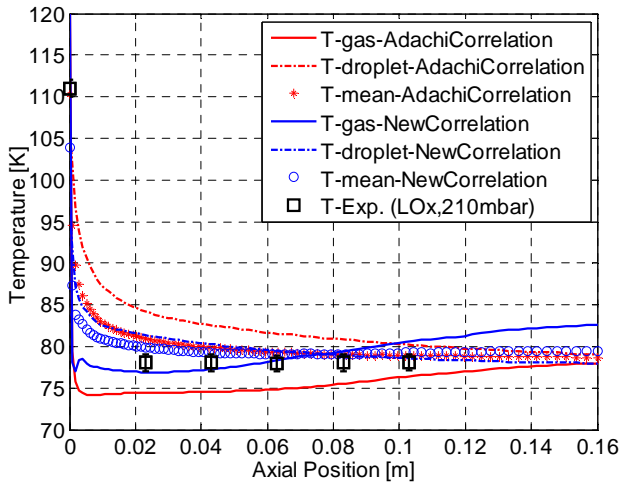


Fig. 5.38 LOx temperature distribution with new superheat evaporation correlation (Case#1)

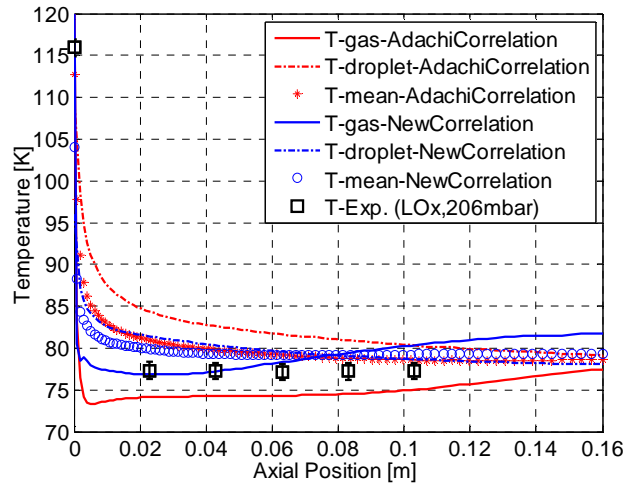


Fig. 5.39 LOx temperature distribution with new superheat evaporation correlation (Case#4)

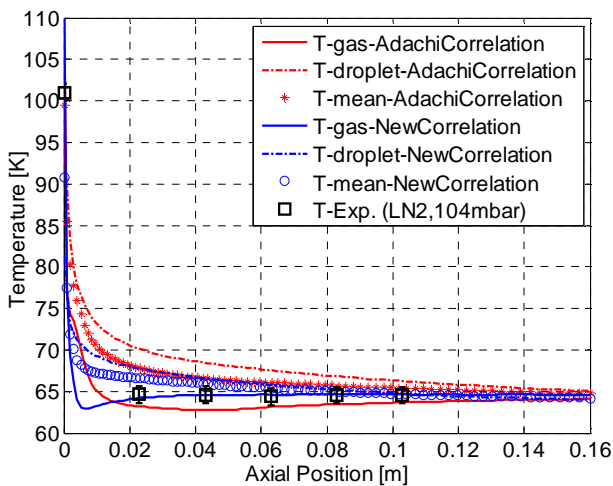


Fig. 5.40 LN<sub>2</sub> temperature distribution with new superheat evaporation correlation (Case#2)

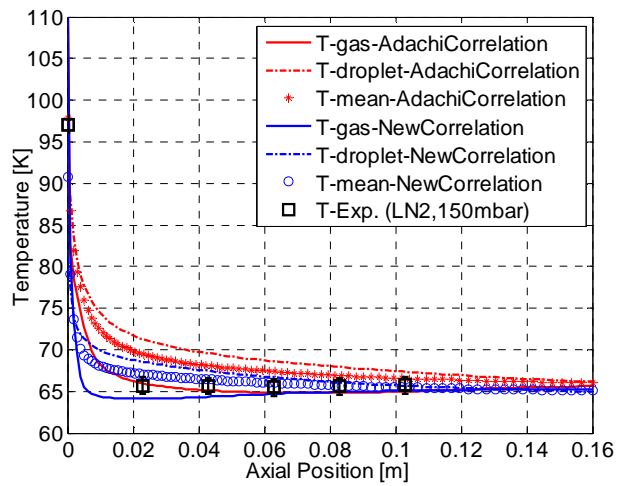


Fig. 5.41 LN<sub>2</sub> temperature distribution with new superheat evaporation correlation (Case#3)

To summarize, the new correlation of flashing evaporation based on the nucleate boiling theory is successfully implemented into the developed FSM model, and it shows better results than Adachi-correlation does.

### 5.6 Summary

In this chapter, a numerical simulation is conducted aiming at the development and verification of a proper numerical model, to further understand the flashing spray. The typical Euler-Lagrange approach is employed for this two-phase flow investigation. The continuous phase is simulated by solving the 3-D URANS equations, and the discrete phase is tracked under Newton's second law. A flashing model is developed and supplemented into the ANSYS solver by taking account of both the internal and external heat transfer to the superheated droplets, as well as the mass, heat and momentum exchange between the two phases. The simulation results agree well with the experimental data. Some conclusions are summarized as below.

- 1). A typical macroscopic morphology of the flashing spray of a bell-shaped profile with a large spray angle is reproduced, and it matches well with the test Schlieren images.
- 2). The simulated spray temperature (average temperature of the droplet ensemble and surrounding vapor) along the spray centerline is in good agreement with the experimental data. The liquid spray experiences a drastic temperature decrease, and loses most of its superheat in the near-injection region, and afterwards the spray approximately approaches the saturation temperature associated with the surrounding pressure.
- 3). After injection, both phases are strongly accelerated and later decelerate to a similar velocity, as a result of the interphase momentum exchange. The velocity distribution in the radial direction maintains self-similarity at different axial positions.
- 4). The pressure in the near-injector region shows much high frequency than that downstream of the injector. This is supposed to be caused by the more violent flash vaporization near the injector orifice.
- 5). The droplet size along the spray centerline shows an approximately power-law decay. In the beginning, the droplet experiences a dramatic size reduction due to the huge flashing evaporation. In the spray radial direction, the droplet size distribution shows a high number density of small droplets near the spray center and middle, whereas some large droplets move radially outwards because of the large inertial force.
- 6). Since the simulated temperatures of the droplets deviate much from the test data with Adachi-correlation, a new flashing evaporation model is developed and added to the Flashing Spray Model. The simulation results match the test data better than the Adachi-correlation.

The numerical work demonstrates that the developed FSM model works successful for the numerical prediction of the flashing spray. For the further study, it can be linked with other models (e.g. combustion model) to investigate the concerned issues of the engine.



# Chapter 6. Conclusions and Outlooks

## 6.1 Summary and Conclusions

This research work is performed under the project “Propulsion Technologies for Green in-Orbit Spacecraft”, which is aimed at the development of green propulsion techniques for addressing the issue of space safety that is threatened by increasing space debris. As a consequence, an understanding of the green propellants’ behavior under vacuum conditions for the upper stage engine or in-orbit thruster is the main motivation of the present work. This research is mainly divided into two parts: the experimental work and the modeling with CFD.

### 6.1.1 Experimental Work

In order to perform this research project, a flashing test facility has been designed and built in the Institute of Turbomachinery and Flight Propulsion of Technische Universität München (LTF-TUM). The study of  $\text{LN}_2$ ,  $\text{LOx}$  and  $\text{LCH}_4$  sprays was conducted with the help of the high-speed Schlieren and Shadowgraph techniques, and the Global Rainbow Refractive technique. Under low pressure conditions, the cryogenic sprays experience violent atomization and vaporization, termed as the flashing phenomenon. The characteristics of this phenomenon (i.e. the flashing evolution process, temperature distribution, solidification, and atomization regimes’ transition criteria) and the effect of injector geometry on this phenomenon have been discussed in detail.

The morphological study shows that the superheat (as a driving force) facilitates the flashing spray atomization. With the liquid superheat increasing (chamber pressure decreasing), the spray undergoes a complex evolution, from the mechanical atomization regime (with aerodynamics dominated) to the fully flashing regime (with thermodynamics dominated). In this work, following Lienhard and Lamanna’s work, from the nucleate boiling perspective, a non-dimensional energy barrier  $\zeta$  was proposed, which refers to the ratio of the bubble nucleation barrier to the excessive thermal energy that the cluster molecules had. This parameter was validated with the experimental data and can successfully indicate the flashing spray. As the spray undergoes the process from the mechanical atomization regime to the fully flashing regime, the parameter  $\zeta$  correspondingly varies from much larger than 1 to less than 1, and in the onset of the fully flashing regime,  $\zeta$  is around 1.

In order to study the effect of the injector geometry on the flashing spray, tests with different geometry parameters were conducted. The test results show that both a large injector diameter and a large injector aspect ratio enhance the flashing spray. This positive effect is mainly attributed to the heterogeneous

## 6. Conclusions and Outlooks

---

nucleation, since a injector with a large diameter or a large aspect ratio hosts more nucleation sites, which are favorable to the heterogeneous nucleation.

The thermal behavior of the spray was investigated with an intrusive measurement by positing thermocouples (Type T) in the spray centerline at equal distances. The thermal profiles show a temperature decrease followed by a sharp drop prior to the saturation temperature associated to the chamber pressure. The steep temperature drop in the beginning is due to the violent flashing evaporation in this time period. In addition, in the stable state, the temperature distribution remains approximately uniform downstream of the injector. During the test, the solidification phase transitions in the LN<sub>2</sub> spray and LCH<sub>4</sub> spray were observed. This is ascribed to the flashing atomization and vaporization triggered by the sudden depressurization. The massively evaporated vapor formed from the liquid droplet surface absorbs the latent heat of vaporization from the remaining droplet, resulting in a drastic temperature decrease that leads to a solidification phase change. It was found that the existence of the solid phase is pressure dependent. The solidification was going on when the chamber pressure was below the triple point pressure. Once the pressure exceeded the triple point pressure, the melting or sublimation phase transition occurred.

Following the morphological study, a quantitative optical diagnostic investigation was conducted. A literature survey shows that it still has a great challenge to the quantitative study of the cryogenic spray. In this work, the Global Rainbow Refractometry technique (GRR), for the first time, was applied to the cryogenic sprays. This technique can provide an accurate measurement of droplet refractive index and size distribution simultaneously. The GRR test setup was built and the inversion method was developed. The test successfully obtained the typical rainbow patterns of the cryogenic droplets. Both the refractive index and the droplet size probability distribution were derived from the recorded rainbow patterns with the methods (including Saengkaew's inversion method) based on the complex angular momentum (CAM) scattering theory. Results show that the derived temperatures from the rainbow signal agree well with the temperatures measured by thermocouples, with the relative error within 7.5%. The retrieved droplet size displays a bimodal or multimodal distribution feature. The GRR technique thus proves its capability in the cryogenic spray investigation.

### 6.1.2 Modeling Work

In order to further understand thermodynamics of the flashing spray, a numerical simulation of this two-phase flow was performed with the coupled Euler-Lagrange method. The continuous phase is simulated by solving the 3-D URANS equations, and the discrete phase is tracked under Newton's second law. A Flashing Spray Model (FSM) has been developed and successfully supplemented to the ANSYS CFD solver, by considering the flashing evaporation, and heat, mass and momentum exchange between the discrete phase and the continuous phase.

From the simulation, the flashing spray's macroscopic morphologies with bell-shaped profiles were reproduced, and the results match well with the experimental Schlieren images. The simulated spray temperature (averaged by the temperature of the droplet ensemble and surrounding vapor) along the spray centerline is in good agreement with the experimental data. The liquid spray experiences a drastic

cooling process, and loses most of its superheat in a short distance downstream of the injector orifice, and afterwards the spray approximately approaches to the saturation temperature associated with the surrounding pressure. After injection, both phases are strongly accelerated and then decelerated to a similar velocity due to the interphase momentum exchange. The velocity distribution in the radial direction maintains self-similarity at different axial positions. Because of the violent flash vaporization in the near-injection region, the pressure oscillations in this region show much high frequency than that downstream of the injector. The droplet size along the spray centerline shows an approximately a power-law decay. Initially, it experiences a dramatic size reduction due to a violent flashing evaporation. In the spray radial direction, the droplet size distribution shows a high number density of small droplets concentrated near the spray center, with some larger droplets swept radially outwards due to their large inertial force.

Though the average temperature of the spray simulated with the Adachi-correlation matches well with the experimental data, the simulated temperatures of the droplets deviate lots from the measured temperatures. Therefore, a new flashing evaporation model was developed using the nucleate boiling correlations. The new model shows an improved agreement between the measurements and simulations.

## 6.2 Outlooks

A comprehensive experimental and modeling investigation of the cryogenic flashing sprays has been explored at great length in this work. The main characteristics of the cryogenic flashing sprays have been obtained. However, still some details information of these sprays is lacked. By the pre-knowledge of such phenomenon of this work, the further experimental work can be emphasized on:

- (1). Quantitative measurements of the flashing spray for the spray droplet distribution, such as the PDPA technique. This can be used to validate the GRR technique, and also can provide a reliable inlet boundary condition of droplet size distributions for the CFD study.
- (2). Adapt the flashing spray test facility to LOx/LCH<sub>4</sub> fire test to investigate the transient injection process as well as the combustion process under vacuum conditions. The high-speed Schlieren and Global Rainbow Refractometry (GRR) techniques can be employed to characterize the transient injection process of the propellants.

As a prediction method, the flashing spray model can be linked with the combustion model to investigate the thermal process of the propellant injection and the combustion process inside the chamber. Departing from this point, the following topics can be introduced:

- (1). Although the validated Flashing Spray Model in this research has successfully predicted the flashing spray, as analyzed in the thesis, the detailed spray vortex structures have not been reproduced due to the inherent features of the RANS method we used. Therefore, the LES method can be further employed to predict more detail of the spray.

## 6. Conclusions and Outlooks

---

(2). The integration of the flashing process and combustion process will be of great significance to investigate the thermal load and combustion performance in the transient start-up of the in-orbit thruster.

## Bibliography

- [1] "ECHA SVHC Support Document EC Number 206-114-9," 2011.
- [2] T. Neill, D. Judd, E. Veith and D. Rousar, "Practical uses of liquid methane in rocket engine application," in *57th International Astronautical Congress (IAC)*, Valencia, 2006.
- [3] M. D. Klem, T. D. Smith, M. F. Wadel, M. L. Meyer, J. M. Free and H. A. Cikanek, "Liquid oxygen/liquid methane propulsion and cryogenic advanced development," in *62nd International Aeronautical Congress (IAC)*, Cape Town, 2011.
- [4] C. Bonhomme, M. Theron, E. Louaas, A. Beaurain and E. Seleznev, "French / Russian activities on LOX - LCH<sub>4</sub> area," in *57th International Astronautical Congress (IAC)*, Valencia, 2006.
- [5] V. Salvatore, F. Battista, P. D. Matteis and L. D. Rose, "Current Activities for the Development of a LOX/LCH<sub>4</sub> Regenerative Thrust Chamber at the Italian Aerospace Research Centre," in *Space Propulsion Conference*, Cologne, 2014.
- [6] O. J. Haidn, M. Oswald, W. Clauss, R. Arnold, J. Sender, A. Preuss, D. Preclik, C. Mäding, J. Görgen and S. Soller, "LOX / methane technology efforts for future liquid rocket engines," in *Conference: 5th International Spacecraft Propulsion Conference & 2nd International Symposium on Propulsion for Space Transportation*, Crete, 2008.
- [7] V. G. Baidakov and V. P. Skripov, "Experimental study of cryogenic liquids in the metastable superheated state," *Experimental Thermal and Fluid Science*, vol. 5, no. 5, pp. 664-678, 1992.
- [8] D. Becker and W. Döring, "The kinetic treatment of nuclear formation in supersaturated vapors," *Annalen der Physik*, vol. 24, no. 5, pp. 19-52, 1935.
- [9] V. I. Kalikmanov, *Nucleation Theory*, Netherland: Springer, 2013.
- [10] S. Whitaker, "Forced convection heat transfer correlations for flow in pipes, past flat plates, single cylinders, single spheres, and for flow in packed beds and tube bundles," *AIChE Journal*, vol. 18, no. 2, pp. 361-371, 1972.
- [11] S. D. Lubetkin, "Why is it much easier to nucleate gas bubbles than the theory predicts?," *Langmuir*, vol. 19, no. 7, pp. 2575-2587, 2003.

- 
- [12] V. P. Carey, *Liquid–vapor phase change phenomena*, Boca Raton: Taylor & Francis Inc, 2007.
- [13] A. Prosperetti and M. S. Plesset, "Vapour-bubble growth in a superheated liquid," *Journal of Fluid Mechanics*, vol. 85, pp. 349-368, 1978.
- [14] M. S. Plesset and S. A. Zwick, "The growth of vapor bubbles in superheated liquids," *Journal of Applied Physics*, vol. 25, pp. 493-500, 1954.
- [15] M. S. Plesset and A. Prosperetti, "Bubble dynamics and cavitation," *Annual Review of Fluid Mechanics*, vol. 9, pp. 145-185, 1977.
- [16] B. Mikic, W. M. Rohsenow and P. Griffith, "On bubble growth rates," *International Journal of Heat and Mass transfer*, vol. 13, pp. 657-666, 1970.
- [17] T. G. Theofanous, "Universal relations for bubble growth," *International Journal of Heat and Mass Transfer*, vol. 19, pp. 425-429, 1976.
- [18] O. Miyatake, I. Tanaka and N. Lior, "A simple universal equation for bubble growth in pure liquids and binary solutions with a nonvolatile solute," *International Journal of Heat and Mass Transfer*, vol. 40, no. 7, pp. 1577-1584, 1997.
- [19] E. Sher, T. Bar-Kohany and A. Rashkovan, "Flash-boiling atomization," *Progress in Energy and Combustion Science*, vol. 34, pp. 417-439, 2008.
- [20] R. Brown and L. York, "Sprays Formed by Flashing Liquid Jets," *AIChE Journal*, vol. 28, no. 2, pp. 149-153, 1962.
- [21] Y. Kitamura, H. Morimitsu and T. Takahashi, "Critical superheat for Flashing of superheated liquid jet," *Ind. Eng. Chem. Fundam*, vol. 25, no. 2, pp. 207-211, 1986.
- [22] N. Nagai, K. Sato and C. W. Lee, "Atomisation characteristics of superheated liquid jets," in *International Conference on Liquid Atomisation and Spray Systems*, London, 1985.
- [23] V. Cleary, P. Bowen and H. Witlox, "Flashing liquid jets and two-phase droplet dispersion. I. Experiments for derivation of droplet atomization correlation," *Journal of Hazardous Materials*, vol. 142, pp. 786-796, 2007.
- [24] D. W. Johnson and J. L. Woodward, *A model with data to predict aerosol rainout in accidental releases*, New York: Center of Chemical Process Safety (CCPS), 1999.
- [25] C. van den Bosch and N. Duijm, "Finite duration spray releases," in *Methods for the calculation of physical effects*, Hague, Committee for the Prevention of Disasters, 1997, pp. 2.107-2.114.
- [26] T. Gemci, K. Yakut, N. Chigier and T. C. Ho, "Experimental study of flash atomization of binary hydrocarbon liquids," *International Journal of Multiphase Flow*, vol. 30, no. 4, pp. 395-417, 2004.
- [27] M. Luo and O. J. Haidn, "Characterization of Flashing Phenomena with Cryogenic Fluid under

- Vacuum Conditions," *Journal of propulsion and power*, vol. 32, no. 5, pp. 1253-1263, 2016.
- [28] W. O. Mayer, A. H. Schlik, B. Vielle, C. Chauveau, I. Gökalp, D. G. Talley and R. D. Woodward, "Atomization and Breakup of Cryogenic propellants under high-pressure subcritical and supercritical conditions," *Journal of Propulsion and Power*, vol. 14, no. 5, pp. 835-842, 1998.
- [29] R. Karami, N. Ashgriz and H. N. Tran, "The effect of flashing on characteristics of sprays of splash-plate nozzle," in *22nd Annual Conference on Liquid Atomization and Spray Systems*, Cincinnati, 2010.
- [30] M. Vieira and J. Simoes-Moreira, "Low-pressure flashing mechanisms in iso-octane liquid jets," *Journal of Fluid Mechanics*, vol. 572, pp. 121-144, 2007.
- [31] G. Lamanna, H. Kamoun and B. Weigand, "Towards a unified treatment of fully flashing spray," *International Journal of Multiphase Flow*, vol. 58, pp. 168-184, 2013.
- [32] R. C. Reid, "Possible mechanism for pressurized- liquid tank explosions or BLEVE's," *Science*, vol. 203, pp. 1263-1265, 1979.
- [33] J. E. Shepherd and B. Sturtevant, "Rapid evaporation at the superheat limit," *Journal of Fluid Mechanics*, vol. 121, pp. 379-402, 1982.
- [34] H. Witlox, M. Harper, P. Bowen and V. Cleary, "Flashing liquid jets and two-phase droplet dispersion. II. Comparison and validation of droplet size and rainout formulations," *Journal of Hazardous Materials*, vol. 142, pp. 797-809, 2007.
- [35] R. D. Reitz, "A photographic study of flash-boiling atomization," *Aerosol Science and Technology*, vol. 12, no. 3, pp. 561-569, 1990.
- [36] E. M. Peter, A. Takimoto and Y. Hayashi, "Flashing and shattering phenomena of superheated liquid jets," *JSME International Journal Series B, Fluids and Thermal Engineering*, vol. 37, no. 2, pp. 313-321, 1994.
- [37] B. S. Park and S. Lee, "An experimental investigation of the Flash atomization mechanism," *Atomization and Sprays*, vol. 4, no. 2, pp. 159-179, 1994.
- [38] M. Adachi, V. McDonnell, D. Tanaka, J. Senda and H. Fujimoto, "Characterization of fuel vapor concentration inside a flash boiling spray," in *SAE Paper 970871*, Detroit, 1997.
- [39] J. R. Simoes-Moreira, M. M. Vieira and E. Angelo, "Highly Expanded Flashing Liquid Jets," *Journal of Thermophysics and heat transfer*, vol. 16, no. 3, pp. 415-424, 2002.
- [40] W. Zeng, M. Xu, G. Zhang, Y. Zhang and D. J. Cleary, "Atomization and vaporization for flash-boiling multi-hole sprays with alcohol fuels," *Fuel*, vol. 95, pp. 287-297, 2012.
- [41] E. Hervieu and T. Veneau, "Experimental determination of the droplet size and velocity distributions at the exit of the bottom discharge pipe of a liquefied propane storage tank during a

- sudden blowdown," *Journal of Loss Prevention in the Process Industries*, vol. 9, no. 6, pp. 413-425, 1996.
- [42] J. T. Allen, "Laser-based measurements in two-phase Flashing propane jets. Part one: velocity profiles," *Journal of Loss Prevention in the Process Industries*, vol. 11, no. 5, pp. 291-297, 1998.
- [43] J. T. Allen, "Laser-based measurements in two-phase Flashing propane jets. Part two: droplet size distribution," *Journal of Loss Prevention in the Process Industries*, vol. 11, no. 5, pp. 299-306, 1998.
- [44] D. Yildiz, "Experimental investigation of superheated liquid jet atomization due to flashing phenomena," *Ph.D Dissertation, Université Libre de Bruxelles ULB, Belgium*, 2005.
- [45] H. Vu, O. Garcia-Valladares and G. Aguilar, "Vapor/liquid phase interaction in flare flashing sprays used in dermatologic cooling," *International Journal of Heat and Mass Transfer*, vol. 51, pp. 5721-5731, 2008.
- [46] Z. Zhou, W. Wu, B. Chen, G. Wang and L. Guo, "An experimental study on the spray and thermal characteristics of R134a two-phase flashing spray," *International Journal of Heat and Mass Transfer*, vol. 55, pp. 4460-4468, 2012.
- [47] H. Kamoun, G. Lamanna, S. Ruberto, B. Weigand, A. Komenda and J. Steelant, "Experimental investigations of fully flashing jets," in *Space Propulsion Conference*, Cologne, 2014.
- [48] D. Weber and P. Leick, "Structure and velocity field of individual plumes of flashing gasoline direct injection sprays," in *26th Annual Conference on Liquid Atomization and Spray Systems (ILASS-Europe)*, Bremen, 2014.
- [49] G. Lamanna, P. Pack, Y. Khanfir and J. Steelant, "Droplet sizing and infrared temperature measurements in superheated sprays," in *8th European Symposium on Aerothermodynamics for Space Vehicles*, Lisbon, 2015.
- [50] M. R. Vetrano, J. P. A. J. van Beek and M. L. Riethmuller, "Global rainbow thermometry: improvements in the data inversion algorithm and validation technique in liquid-liquid suspension," *Applied Optics*, vol. 43, no. 18, pp. 3600-3607, 2004.
- [51] M. R. Vetrano, A. Simonini, J. Steelant and P. Rambaud, "Flashing jet characterization by non-intrusive laser based measurement technique," in *16th International Symposiums on Applications of Laser Techniques to Fluid Mechanics*, Lisbon, 2012.
- [52] D. Yildiz, J. P. A. J. van Beeck and M. L. Riethmuller, "Global rainbow thermometry applied to a flashing two-phase R134-A jet," in *10th International Symposium on Applications of Laser Techniques to Fluid Mechanics*, Lisbon, 2002.
- [53] H. Kamoun, G. Lamanna, B. Weigand and J. Steelant, "Thermal characterisation of an ethanol flashing jet using differential infrared thermography," in *4th European Conference for Aero-space Sciences*, Saint Petersburg, 2011.

- [54] G. Lamanna, H. Kamoun, B. Arnold, K. Schlottke, B. Weigand and J. Steelant, "Differential infrared thermography (DIT) in a flashing jet: a feasibility study," *Quantitative InfraRed Thermography Journal*, vol. 10, no. 1, pp. 112-131, 2013.
- [55] V. Gautam and A. K. Gupta, "Fate of cryogenic fluid flow and atomization from a sheer coaxial injector under pre-ignition conditions," in *44th AIAA/ASME/ASME/SAE/ASEE Joint Propulsion Conference & Exhibit*, Hartford, 2008.
- [56] V. Gautam and A. K. Gupta, "Cryogenic flow and atomization from a coaxial injector," *Journal of Propulsion and Power*, vol. 25, no. 1, pp. 33-39, 2009.
- [57] C. Manfretti, "Laser ignition of an experimental cryogenic reaction and control thruster: pre-ignition conditions," *Journal of Propulsion and Power*, vol. 30, no. 4, pp. 925-933, 2014.
- [58] G. Lamanna and H. Kamoun, "Flashing behavior of rocket engine propellants," *Atomization and Spray*, vol. 25, no. 10, pp. 837-856, 2015.
- [59] M. Luo and O. J. Haidn, "Injection of cryogenic propellants under low pressure conditions," in *52nd AIAA/SAE/ASEE Joint Propulsion Conference*, Salt Lake City, UT, 2016.
- [60] M. Luo, T. Ramcke, M. Pfitzner and O. Haidn, "Experimental and Numerical Investigation of Flash Atomization with Cryogenic Fluids," in *9th International Conference on Multiphase Flow*, Florence, 2016.
- [61] M. Luo, Y. Wu and O. J. Haidn, "Temperature and Size Measurement of Cryogenic Spray Droplets with Global Rainbow Refractometry," submitted to *Journal of Propulsion and Power*, May 2017.
- [62] S. D. Goldstein, "A computer simulation method for describing two-phase flashing flow in small diameter tubes," *AHSARE Transactions*, vol. 87, no. 2, pp. 51-60, 1981.
- [63] F. Inada and T. Ohkawa, "Thermo-hydraulic instability of natural circulation BWRs (explanation on instability mechanism at start-up by homogeneous and thermal-dynamic equilibrium model considering flashing effect)," in *International Conference on New Trends in Nuclear System Thermohydraulics*, Pisa, Italy, 1994.
- [64] J. C. Leung, "A generalized correlation for one-component homogeneous equilibrium flashing choked flow," *AIChE Journal*, vol. 32, pp. 1743-1746, 1986.
- [65] J. C. Leung, "The Omega method for discharge rate evaluation," in *International symposium on runaway reactions and pressure relief design*, Boston, 1995.
- [66] T. Lenzing, L. Friedel and M. Alhusein, "Critical mass flow rate in accordance with the omega-method of DIERS and the Homogeneous Equilibrium Model," *Journal of Loss Prevention in the Process Industries*, vol. 11, pp. 391-395, 1998.
- [67] Z. Bilicki and J. Kestin, "Physical aspects of the relaxation model in two-phase flow," *Proc. Roy.*

- 
- Soc. London: Ser. A: Math., Phys. Eng. Sci.*, vol. 428, pp. 379-397, 1990.
- [68] D. P. Schmidt, M. Corradini and C. Rutland, "A two dimensional, non-equilibrium model of flashing nozzle flow," in *3rd ASME/JSME Joint Fluids Engineering Conference*, San Francisco, 1999.
- [69] S. Gopalakrishnan and D. P. Schmidt, "A computational study of flashing flow in fuel injector nozzles," *SAE International Journal of Engines*, vol. 1, no. 1, pp. 160-170, 2009.
- [70] K. Neroorkar, S. Gopalakrishnan, J. O. Grover and D. P. Schmidt, "Simulation of flash boiling in pressure swirl injectors," *Atomization and Sprays*, vol. 21, no. 2, pp. 179-188, 2011.
- [71] I. Schmitz, W. Ipp and A. Leipertz, "Flash Boiling Effects on the Development of Gasoline Direct-Injection Engine Sprays," in *SAE Powertrain & Fluid Systems Conference & Exhibition*, San Diego, California, 2002.
- [72] K. Saha, S. Som, M. Battistoni, Y. Li, S. Quan and P. K. Senecal, "Modeling of internal and near-nozzle flow for gasoline direct injection fuel injector," *Journal of Energy Resources Technology*, vol. 138, pp. 052208-1-11, 2016.
- [73] J. R. Simoes-Moreira and C. W. Bullard, "Pressure drop and flashing mechanisms in refrigerant expansion devices," *International Journal of Refrigeration*, vol. 16, pp. 840-848, 2003.
- [74] E. Angelo and J. R. Simões-Moreira, "Numerical solution of highly expanded flashing liquid jets," *Journal of thermophysics and heat transfer*, vol. 21, no. 2, pp. 379-391, 2007.
- [75] B. Zuo, A. Gomes and C. Rutland, "Modelling superheated fuel sprays and vaporization," *International Journal of Engine Research*, vol. 1, no. 4, pp. 321-336, 2000.
- [76] M. S. Raju, "CFD modeling of superheated fuel sprays," in *47th Aerospace Sciences Meeting sponsored by the American Institute of Aeronautics and Astronautics*, Orlando, 2009.
- [77] R. Schmehl and J. Steelant, "Flashing-evaporation of oxidizer during start-up of an upper-stage rocket engine," in *39th AIAA/ASME SAE/ASEE Joint Propulsion Conference and Exhibit*, Huntsville, Alabama, 2003.
- [78] T. Ramcke and M. Pfitzner, "Numerical simulations of atomization and flash evaporation of cryogenic nitrogen injection," in *8th International Symposium On Turbulence, Heat and Mass Transfer*, Sarajevo, 2015.
- [79] T. Ramcke, A. Lampmann and M. P. Michael, "Simulations of Injection of Liquid Oxygen/Gaseous Methane Under Flashing Conditions," *Journal of Propulsion and Power*, vol. 34, no. 2, pp. 395-407, 2018.
- [80] M. Luo, U. Rana and O. Haidn, "Modeling Investigation of Liquid Oxygen Flashing Spray with CFD," submitted to *Journal of Thermophysics and Heat Transfer*, May 2018.

## Bibliography

---

- [81] G. S. Settles, *Schlieren and Shadowgraph Techniques: visualizing phenomena in transparent media*, New York: Springer-Verlag, 2001.
- [82] K. D. Timmerhaus and T. M. Flynn, *Cryogenic process engineering*, New York: Plenum Press, 1989.
- [83] W. V. Ohnesorge, "Die Bildung von Tropfen an Düsen und die Auflösung flüssiger Strahlen," *Zeitschrift für Angewandte Mathematik und Mechanik*, vol. 16, no. 6, pp. 355-358, 1936.
- [84] C. C. Miesse, "Correlation of experimental data on the disintegration of liquid jets," *Industrial and Engineering Chemistry*, vol. 47, no. 9, pp. 1690-1701, 1955.
- [85] R. D. Reitz and F. V. Bracco, "Mechanisms of Breakup of Round Liquid Jets," *The Encyclopedia of Fluid Mechanics*, vol. 3, pp. 233-243, 1986.
- [86] S. P. Lin and R. D. Reitz, "Drop and spray formation from a liquid jet," *Annual Review of Fluid Mechanics*, vol. 30, pp. 85-105, 1998.
- [87] M. Blander and J. I. Katz, "Bubble nucleation in liquids," *AIChE Journal*, vol. 21, no. 5, pp. 833-848, 1975.
- [88] K. Nishigaki and Y. Saji, "The superheat-limit of liquid oxygen and nitrogen at 1 atm," *Japanese Journal of Applied Physics*, vol. 20, no. 5, p. 849-853, 1981.
- [89] M. Das, B. K. Chatterjee, B. Roy and S. C. Roy, "How can the temperature of liquid be raised without boiling?," *Physical Review E*, vol. 62, no. 4, pp. 5843-5846, 2000.
- [90] G. Polanco, A. E. Holdo and G. Munday, "General review of flashing studies," *Journal of Hazardous Materials*, vol. 173, pp. 2-18, 2010.
- [91] L. Nghiem, H. Merte, E. Winter and H. Beer, "Prediction of transient inception of boiling in terms of a heterogeneous nucleation theory," *Journal of Heat Transfer*, vol. 103, no. 1, pp. 69-73, 1981.
- [92] B. S. Kim, H. T. Shin, Y. P. Lee and J. Jurng, "Study on ice slurry production by water spray," *International Journal of Refrigeration*, vol. 24, no. 2, p. 176-184, 2001.
- [93] J. H. Lienhard and A. Karimi, "Homogeneous nucleation and the spinodal line," *Journal of Heat Transfer*, vol. 103, pp. 61-64, 1981.
- [94] W. O. Mayer, "Coaxial atomization of a round liquid jet in a high speed gas stream: A phenomenological study," *Experiments in Fluids*, vol. 16, pp. 401-410, 1994.
- [95] N. Saiyed, J. Jurns and D. Chato, "LN<sub>2</sub> spray droplet size measurement via ensemble diffraction technique," in *26th Thermophysics conference*, Honolulu, Hawaii, 1991.
- [96] R. D. Ingebo, "Characteristics of vaporizing cryogenic sprays for rocket combustion modeling," in *ASME International Joint Power Generation Conference*, Phoenix, 1994.

- [97] O. J. Haidn and M. Habiballah, "Research on high pressure cryogenic combustion," *Aerospace Science and technology*, vol. 7, no. 6, pp. 473-491, 2003.
- [98] N. Roth, K. Anders and A. Frohn, "Simultaneous measurement of temperature and size of droplets in the micrometer range," *Journal of Laser Application*, vol. 2, no. 1, pp. 37-42, 1990.
- [99] J. P. A. J. van Beeck and M. L. Riethmuller, "Rainbow phenomena applied to the measurement of droplet size and velocity and to detection of nonsphericity," *Applied Optics*, vol. 35, no. 13, pp. 2259-2266, 1996.
- [100] J. Wilms and B. Weigand, "Composition measurements of binary mixture droplets by rainbow refractometry," *Applied Optics*, vol. 46, no. 11, pp. 2109-2118, 2007.
- [101] X. Wu, Y. Wu, S. Saengkaew, S. Meunier-Guttin-Cluzel, G. Gréhan, L. Chen and K. Cen, "Concentration and composition measurement of sprays with a global rainbow technique," *Measurement Science and Technology*, vol. 23, no. 12, p. 125302, 2012.
- [102] M. Ouboukhlik, S. Saengkaew, M.-C. Fournier-Salauin, L. Estel and G. Grehan, "Local measurement of mass transfer in a reactive spray for CO<sub>2</sub> capture," *The Canadian Journal of Chemical Engineering*, vol. 93, no. 2, pp. 419-426, 2014.
- [103] C. Letty, B. Renou, J. Reveillon, S. Saengkaew and G. Gréhan, "Experimental study of droplet temperature in a two-phase heptane/air V-flame," *Combustion and Flame*, vol. 160, no. 9, pp. 1803-1811, 2013.
- [104] S. Saengkaew, T. Charinpanitkul, H. Vanisri, W. Tanthapanichakoon, Y. Biscos, N. Garcia, G. Lavergne, L. Mees, G. Gouesbet and G. Grehan, "Rainbow refractometry on particles with radial refractive index gradients," *Experiments in Fluids*, vol. 43, pp. 595-601, 2007.
- [105] C. D. Rosebrocka, S. Shirinzadehb, M. Soekenb, N. Rieflera, T. Wriedta, R. Drechslerb and L. Mädler, "Time-resolved detection of diffusion limited temperature gradients inside single isolated burning droplets using Rainbow Refractometry," *Combustion and Flame*, vol. 168, pp. 255-269, 2016.
- [106] J. A. Adam, "The mathematical physics of rainbows and glories," *Physics Reports*, vol. 365, pp. 229-365, 2002.
- [107] C. Bohren and D. Huffman, *Absorption and Scattering of Light by Small Particles*, New York: Wiley, 1983.
- [108] H. Johns and J. Wilhelm, "The refractive index of liquid oxygen, nitrogen and hydrogen," *Canadian Journal of Research*, vol. 15, no. 7, pp. 101-108, 1937.
- [109] A. Yoshihara, A. Anderson, R. Aziz and C. Lim, "Brillouin scattering and refractive index measurements on low temperature liquids. I. Methane, CH<sub>4</sub> and CD<sub>4</sub>," *Chemical Physics*, vol. 48, no. 2, pp. 183-191, 1980.

- [110] J. P. A. J. van Beeck, L. Zimmer and M. L. Riethmuller, "Global rainbow thermometry for mean temperature and size measurement of spray droplets," *Part. Part. Syst. Charact.*, vol. 18, pp. 196-204, 2001.
- [111] S. Saengkaew, T. Charinpanikul, C. Laurent, Y. Biscos, G. Lavergne, G. Gouesbet and G. Gréhan, "Processing of individual rainbow signals," *Experiments in Fluids*, vol. 48, no. 1, pp. 111-119, 2010.
- [112] H. Nussenzveig, "High Frequency Scattering by a Transparent Sphere. II. Theory of the Rainbow," *Journal of Mathematical Physics*, vol. 10, no. 1, pp. 125-176, 1969.
- [113] V. Khare and H. Nussenzveig, "Theory of the rainbow," *Physical Review Letters*, vol. 33, no. 16, pp. 976-980, 1974.
- [114] H. C. van de Hulst, *Light scattering by small particles*, New York: John Wiley & Sons, 1957.
- [115] J. A. Lock, "Supernumerary spacing of rainbows produced by an elliptical-cross-section cylinder. I. Theory," *Applied Optics*, vol. 39, no. 27, pp. 5040-5051, 2000.
- [116] G. Swirniak, G. Glomb and J. Mroczka, "Inverse analysis of the rainbow for the case of low-coherent incident light to determine the diameter of a glass fiber," *Applied Optics*, vol. 53, no. 19, pp. 4239-4247, 2014.
- [117] Y. Wu, J. Promvonggsa, X. Wu, K. Cen, G. Grehan and S. Saengkaew, "One-dimensional rainbow technique using Fourier domain filtering," *Optics Express*, vol. 23, no. 23, pp. 30545-30556, 2015.
- [118] V. Bodoc, J. Wilms, Y. Biscos, G. Lavergne and O. Rouzaud, "Experimental and numerical investigation of a monocomponent polydisperse spray," in *22nd European Conference on Liquid Atomization and Spray Systems*, Como Lake, 2008.
- [119] F. Lemoine and G. Castanet, "Temperature and chemical composition of droplets by optical measurement techniques: a state-of-art review," *Experiments in Fluids*, vol. 54, pp. 1-34, 2013.
- [120] J. V. Martonchik and G. S. Orton, "Optical constants of liquid and solid methane," *Applied Optics*, vol. 33, no. 36, pp. 8306-8317, 1994.
- [121] H. W. Coleman and W. Steele, *Experimentation, validation, and uncertainty analysis for engineers*, Third Edition ed., New Jersey: John Wiley & Sons, Inc., 2009.
- [122] E. S. Starkman, K. F. N. V. E. Schrock and D. J. Maneely, "Expansion of a very low quality two-phase fluid through a convergent-divergent nozzle," *ASME Journal of Basic Engineering*, vol. 86, no. 2, pp. 247-255, 1964.
- [123] S. Negro and G. M. Bianchi, "Superheated fuel injection modeling: An engineering approach," *International Journal of Thermal Sciences*, vol. 50, pp. 1460-1471, 2011.
- [124] J.-M. Lacome, C. Lemofack, J. Reveillon and F. X. Demoulin, "Numerical modelling of flashing

- liquid jets due to leakage of liquefied gas storage," in *43. ESReDA Seminar on Land Use Planning*, Rouen, France, 2012.
- [125] S. Gopalakrishnan and D. P. Schmidt, "Multidimensional simulation of flash-boiling fuels in injector nozzles," in *29th Annual Conference on Liquid Atomization and Spray Systems (ILASS Americas)*, Orlando, Florida, 2008.
- [126] M. Adachi, V. McDonnel, D. Tanaka, J. Senda and H. Fujimoto, "Characteristics of fuel vapor concentration inside a flash boiling spray," in *SAE Paper 970871*, 1997.
- [127] B. Abramzon and W. Sirignano, "Droplet vaporization model for spray combustion calculations," *International Journal of Heat and Mass Transfer*, vol. 32, no. 9, pp. 1605-1618, 1989.
- [128] E. M. G. J. L. Sparrow, "The variable fluid property problem in free convection," *Transactions of the ASME*, vol. 80, pp. 879-886, 1958.
- [129] S. A. Morsi and A. J. Alexander, "An investigation of particle trajectories in two-phase flow systems," *Journal of Fluid Mechanics*, vol. 55, no. 2, pp. 193-208, 1972.
- [130] P. Eisenklam, S. Arunachalam and J. Weston, "Evaporation rates and drag resistance of burning drops," *Symposium (International) on Combustion*, vol. 11, no. 1, pp. 715-728, 1967.
- [131] P. J. Linstrom and W. G. Mallard, NIST Chemistry WebBook, NIST Standard Reference Database Number 69, National Institute of Standard and Technology, 2011.
- [132] A. Munnannur and R. D. Reitz, "Droplet collision modeling in multi-dimensional spray computations," in *International Multidimensional Engine Modeling User's Group Meeting at the SAE Congress*, Detroit, 2007.
- [133] J. Abraham, "What is Adequate Resolution in the Numerical Computations of Transient Jets?," in *International Congress & Exposition*, Detroit, Michigan, 1997.
- [134] Y. Wang, H. Ge and R. D. Reitz, "Validation of Mesh- and Timestep- Independent Spray Models for Multi-Dimensional Engine CFD Simulation," *SAE International Journal of Fuels and Lubricants*, vol. 3, no. 1, pp. 277-302, 2010.
- [135] J. K. Dukowicz, "A particle-fluid numerical model for liquid sprays," *Journal of Computational Physics*, vol. 35, pp. 229-253, 1980.
- [136] A. Sadiki, A. Maltsev, B. Wegner, F. Flemming, A. Kempf and J. Janicka, "Unsteady methods (URANS and LES) for simulation of combustion systems," *International Journal of Thermal Sciences*, vol. 45, pp. 760-773, 2006.
- [137] G. Aguilera, B. Majaron, W. Verkrusse, Y. Zhou, J. S. Nelson and E. J. Lavenia, "Theoretical and experimental analysis of droplet diameter, temperature, and evaporation rate evolution in cryogenic sprays," *International Journal of Heat and Mass Transfer*, vol. 44, no. 17, pp. 3201-3211, 2001.

## Bibliography

---

- [138] D. L. Frost, "Dynamic of explosive boiling of a droplet," *Physics of Fluids*, vol. 31, pp. 2554-2561, 1988.
- [139] J. C. Lasheras, E. Villermaux and E. J. Hopfinger, "Break-up and atomization of a round water jet by a high-speed annular air jet," *Journal of Fluid Mechanics*, vol. 357, pp. 351-379, 1998.
- [140] F. P. Incropera, D. P. DeWitt, T. L. Bergman and A. S. Lavine, *Principles of Heat and Mass Transfer*, New Jersey: John Wiley & Sons, Inc., 2011.
- [141] W. M. Rohsenow, "A method of correlating heat transfer data for surface boiling of liquids," *Trans. ASME*, vol. 74, pp. 969-975, 1952.



# Appendix

## I. Test Hard Ware



Fig. I.1. Flashing test facility



Fig. I.2. DAQ system

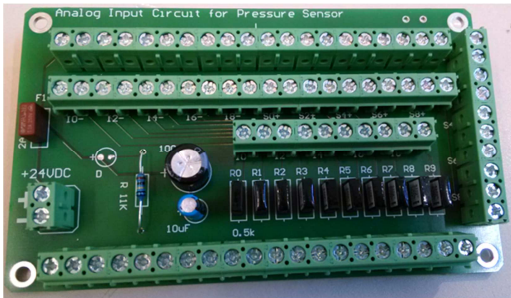


Fig. I.3. Current board for the analog signal input (for pressure sensors)

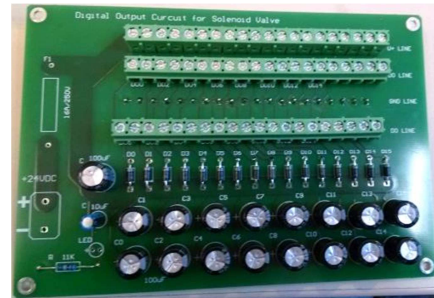


Fig. I.4. Current board for the digital signal output (for solenoid valves)



Fig. I.5. Venturi flow meter



Fig. I.6. Injectors

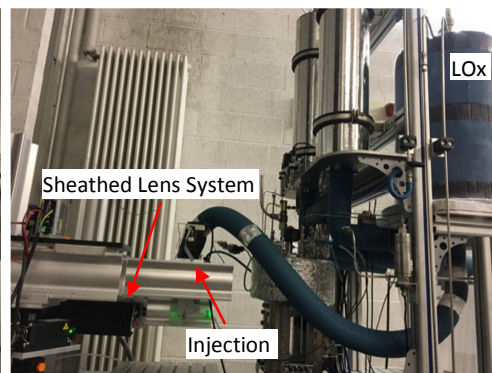
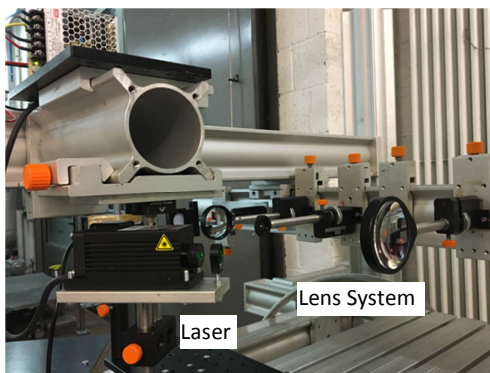


Fig. I.7. Global Rainow Refractometry setup

## II. Lorenz-Mie Theory

The Lorenz-Mie scatter and CAM theory are used in our study for the calculation of the global rainbow signal. In this section, the calculation of droplet scattering intensity by the Lorenz-Mie theory is shown. The detailed information of this theory can be found in the references: “C. Bohren and D. Huffman, Absorption and Scattering of Light by Small Particles, New York: Wiley, 1983.” and “H. C. van de Hulst, Light scattering by small particles, New York: John Wiley & Sons, 1957”.

### A. Mie Coefficients

The rainbow technique in this work concerns the external scatter field. Therefore the key parameters for Mie calculations are the Mie coefficients  $a_n$  and  $b_n$ , which are used to compute the amplitudes of the scattered field.

$$a_n = \frac{m^2 j_n(mx) [xj_n(x)]' - j_n(x) [mxj_n(mx)]'}{m^2 j_n(mx) [xh_n(x)]' - h_n(x) [mxj_n(mx)]'} \quad (\text{II.1})$$

$$b_n = \frac{j_n(mx) [xj_n(x)]' - j_n(x) [mxj_n(mx)]'}{j_n(mx) [xh_n(x)]' - h_n(x) [mxj_n(mx)]'} \quad (\text{II.2})$$

$$n_{\max} = x + 4x^{1/3} + 2 \quad (\text{II.3})$$

where  $x$  is the size parameter and  $x = \pi D / \lambda$ ,  $\lambda$  is the wavelength in the ambient medium,  $m$  is the refractive index relative to the ambient medium,  $D$  is the droplet size and the functions  $j_n(z)$  and  $h_n$  are spherical Bessel function of order  $n$  of the arguments.

### B. Scattered Far-field Intensity

In this work, the scattered far-field intensity in the perpendicular scattering plane (source-particle-observer) is described as  $I_{sca}^\perp(\theta)$ , as shown:

$$I_{sca}^\perp(\theta) = \frac{1}{k^2 r^2} \left| \sum_{n=1}^{n_{\max}} \frac{2n+1}{n(n+1)} (a_n \pi_n + b_n \tau_n) \right|^2 I_{inc}^\perp(\theta) \quad (\text{II.4})$$

Where the wave number  $k = 2\pi/\lambda$ ,  $r$  is the wave propagation distance, and  $I_{inc}^\perp(\theta)$  is the perpendicularly polarized incident intensity.

The functions  $\pi_n$  and  $\tau_n$  describe the angular scattering patterns of the spherical harmonics used to describe the intensity, and they are determined from the recurrence relations

$$\pi_n = \frac{2n-1}{n-1} \cos \theta \cdot \pi_{n-1} - \frac{n}{n-1} \pi_{n-2} \quad (\text{II.5})$$

$$\tau_n = n \cos \theta \cdot \pi_n - (n+1) \pi_{n-1} \quad (\text{II.6})$$

The initial conditions are

$$\begin{cases} \pi_0 = 0; \pi_1 = 1; \pi_2 = 3 \cos \theta \\ \tau_0 = 0; \tau_1 = \cos \theta; \tau_2 = 3 \cos(2\theta) \end{cases} \quad (\text{II.7})$$

Based on the Lorenz-Mie theory, the scattering intensity of a water droplet ( $m=1.335+1e-8i$ ,  $x=591$ ), taken as an example, is obtained, as shown in Fig. II.1. It shows that most of the incident light energy is reflected in front of a droplet (reference of light direction). In the pericircular direction of the light, the light intensity is rather weak (see the intensity at about  $80^\circ\sim 110^\circ$ ). When the scattering angle is larger than about  $120^\circ$ , two distinguished regions characterized with a local intensity peak and some supernumerary arcs are present, as called the rainbow regions. The one close to  $125^\circ$  is the secondary rainbow, and the other close to  $140^\circ$  is the primary rainbow. Between the two rainbows exists a region with a very weak scattering intensity ( $130^\circ\sim 135^\circ$ ), which is the Alexander's dark band.

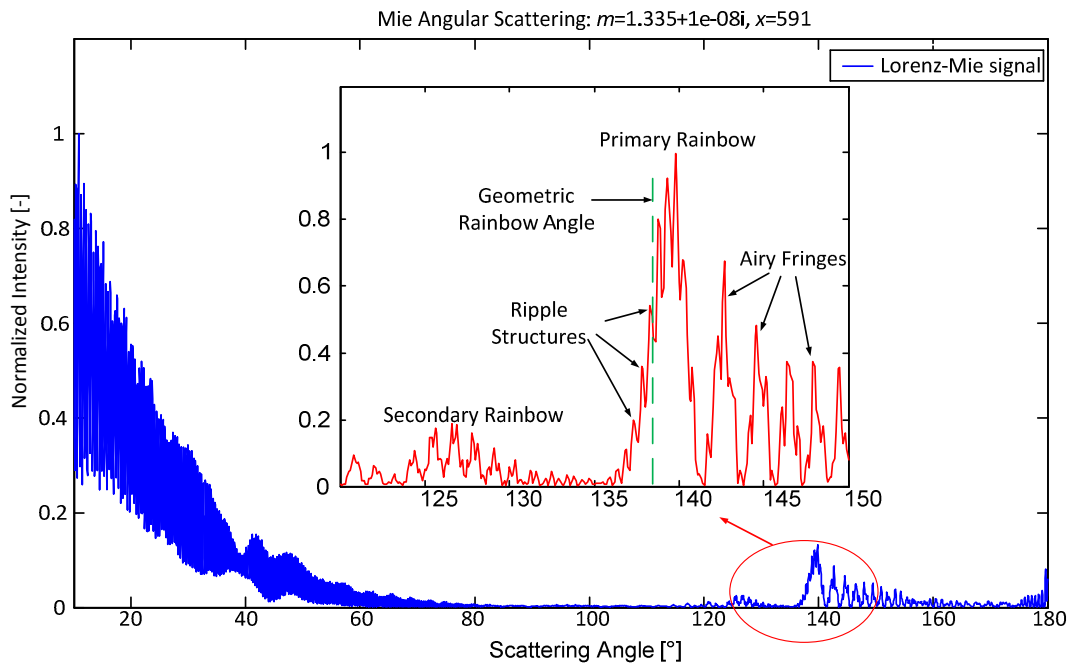


Fig. II.1. Mie-scattering intensity of a single droplet